

Chulalongkorn University

## Chula Digital Collections

---

Chulalongkorn University Theses and Dissertations (Chula ETD)

---

2022

### Nanoporous CU-based catalytic electrodes for electrochemical conversion of carbon dioxide

Jidsucha Darayen  
*Graduate School*

Follow this and additional works at: <https://digital.car.chula.ac.th/chulaetd>

---

#### Recommended Citation

Darayen, Jidsucha, "Nanoporous CU-based catalytic electrodes for electrochemical conversion of carbon dioxide" (2022). *Chulalongkorn University Theses and Dissertations (Chula ETD)*. 5971.  
<https://digital.car.chula.ac.th/chulaetd/5971>

This Thesis is brought to you for free and open access by Chula Digital Collections. It has been accepted for inclusion in Chulalongkorn University Theses and Dissertations (Chula ETD) by an authorized administrator of Chula Digital Collections. For more information, please contact [ChulaDC@car.chula.ac.th](mailto:ChulaDC@car.chula.ac.th).

# Nanoporous Cu-based catalytic electrodes for electrochemical conversion of carbon dioxide



Miss Jidsucha Darayen

A Dissertation Submitted in Partial Fulfillment of the Requirements  
for the Degree of Doctor of Philosophy in Nanoscience and Technology  
Inter-Department of Nanoscience and Technology  
GRADUATE SCHOOL  
Chulalongkorn University  
Academic Year 2022  
Copyright of Chulalongkorn University

ข้าวไฟฟ้าทองแดงพูนระดับนาโนเชิงตัวเร่งปฏิกิริยาสำหรับการเปลี่ยนแก๊สคาร์บอนไดออกไซด์  
ด้วยกระบวนการทางเคมีไฟฟ้า



น.ส.จิตสุชา ดาราเย็น

วิทยานิพนธ์นี้เป็นส่วนหนึ่งของการศึกษาตามหลักสูตรปริญญาวิทยาศาสตรดุษฎีบัณฑิต  
สาขาวิชาวิทยาศาสตร์นาโนและเทคโนโลยี สหสาขาวิชาวิทยาศาสตร์นาโนและเทคโนโลยี

บัณฑิตวิทยาลัย จุฬาลงกรณ์มหาวิทยาลัย

ปีการศึกษา 2565

ลิขสิทธิ์ของจุฬาลงกรณ์มหาวิทยาลัย

Thesis Title	Nanoporous Cu-based catalytic electrodes for electrochemical conversion of carbon dioxide
By	Miss Jidsucha Darayen
Field of Study	Nanoscience and Technology
Thesis Advisor	Professor Dr. YUTTANANT BOONYONGMANEERAT
Thesis Co Advisor	Professor Dr. ORAWON CHAILAPAKUL

---

Accepted by the GRADUATE SCHOOL, Chulalongkorn University in  
Partial Fulfillment of the Requirement for the Doctor of Philosophy

..... Dean of the GRADUATE  
SCHOOL  
(Associate Professor Dr. YOOTTHANA  
CHUPPUNNARAT)

DISSERTATION COMMITTEE

..... Chairman  
(Professor Dr. VUDHICHAIR PARASUK)  
..... Thesis Advisor  
(Professor Dr. YUTTANANT  
BOONYONGMANEERAT)  
..... Thesis Co-Advisor  
(Professor Dr. ORAWON CHAILAPAKUL)  
..... Examiner  
(Assistant Professor Dr. DUANGAMOL  
TUNGASMITA)  
..... Examiner  
(Assistant Professor Dr. RATTHAPOL RANGKUPAN)  
..... External Examiner  
(Dr. Pongkarn Chakthranont)



จิตสุชา คาราฮิน : ขั้วไฟฟ้าทองแดงพรุนระดับนาโนเชิงตัวเร่งปฏิกิริยาสำหรับการเปลี่ยนแก๊สคาร์บอนไดออกไซด์ด้วยกระบวนการทางเคมีไฟฟ้า. ( Nanoporous Cu-based catalytic electrodes for electrochemical conversion of carbon dioxide) อ.ที่ปรึกษาหลัก : ศ. ดร.ยุพรัตน์ บุญยงฉัตรรัตน์, อ.ที่ปรึกษาร่วม : ศ. ดร.อรรณพ ชัยลาภกุล

งานวิจัยนี้ศึกษาแนวทางการเพิ่มประสิทธิภาพของกระบวนการรีดักชันของคาร์บอนไดออกไซด์เพื่อผลิตสารเคมีที่มีค่า เช่น เมทานอล อะซิโตนไดไฮโดรลิก ด้วยการปรับแต่งลักษณะทางกายภาพของทองแดงพรุน ในส่วนของโครงสร้างพรุน และสารประกอบทางเคมี เช่น ทองแดงออกไซด์ มีการทดสอบประสิทธิภาพของกระบวนการรีดักชันของคาร์บอนไดออกไซด์ นอกจากนี้ ความสัมพันธ์ระหว่างพารามิเตอร์การชุบ (ความหนาแน่นกระแสไฟฟ้า, เวลาการชุบ, สารที่ใช้ชุบ), รูพรุน, สารประกอบทางเคมี และผลของกระบวนการรีดักชันของคาร์บอนไดออกไซด์ การศึกษานี้แสดงให้เห็นว่าอัตราส่วนของ คอปเปอร์ซัลเฟตและกรดซัลฟิวริกของสารละลาย, ความหนาแน่นกระแสไฟฟ้า, เวลาการชุบ ส่งผลต่อโครงสร้างรูพรุนที่ได้รับ ซึ่งได้รับการยืนยันด้วยโครงสร้างจุลภาคและการประเมินทางกายภาพ (รูพรุนที่สามารถเห็นได้, รูพรุนจริง, ลักษณะพื้นผิวแบบสองมิติ, ความหนาผิว, พื้นที่ผิวและการกระจายของรูพรุน)

เมื่อควบคุมความเข้มข้นของกรดซัลฟิวริก ทำให้พบว่า ความเข้มข้นที่มากขึ้นของคอปเปอร์ซัลเฟตเพิ่มปริมาณการชุบของทองแดงเป็นการสร้างชิ้นงานทองแดงพรุนที่มีปริมาณรูพรุนที่สูงขึ้นโดยที่ขนาดรูพรุนยังเท่าเดิม ในขณะที่ความหนาแน่นกระแสไฟฟ้าของทองแดงพรุน ทำให้เกิดเป็นทองแดงพรุนที่มีทั้งขนาดรูพรุน และ ปริมาตรรูพรุนสูงที่สุด ทองแดงพรุนทั้งหมดที่ผลิตด้วยกระแสไฟฟ้าคงที่ เป็นวัสดุเมโซพอร์ัส (ขนาดรูพรุนมีค่าอยู่ระหว่าง 2-50 นาโนเมตร เนื่องจากการจัดเรียงตัวของอนุภาคทองแดงที่คล้ายเม็ดคอลลอยด์เรียงกันบนโครงข่ายของโครงสร้างรูพรุนที่ผลิตขึ้นโดย โมดูลอิลิรของคอปเปอร์ซัลเฟตที่ปราศจากกรดไฮโดรคลอริกมีพื้นที่ผิวสูงสุดถึง 19.56 ตารางเมตรต่อกรัม ซึ่งมีค่ามากกว่าทองแดงพรุนอื่น 5-6 เท่า รูพรุนที่สามารถเห็นได้, ประสิทธิภาพการชุบ, และการคำนวณหาปริมาณจริง สามารถยืนยันได้ว่า ทองแดงพรุนที่ชุบด้วยคอปเปอร์ซัลเฟตที่มีความเข้มข้นมากขึ้นมีความหนาแน่นมากที่สุด สารประกอบทางเคมีของเนื้อในและที่ผิวของทองแดงพรุนมีความแตกต่างจากทองแดงแผ่นเล็กน้อย  $\text{Cu}^+$  และ  $\text{Cu}^{2+}$  ถูกตรวจจับบนผิวของทองแดงแผ่นและทองแดงพรุนแต่  $\text{Cu}^0$  ถูกตรวจจับบนผิวของทองแดงทั้งในสารละลายที่มีกรดไฮโดรคลอริกเท่านั้น ยิ่งไปกว่านั้น การผลิตชิ้นงานทองแดงพรุนด้วยการชุบบางครั้ง เป็นอีกวิธีหนึ่ง ที่สามารถสร้างชิ้นงานที่มีความหนาแน่นมากขึ้นโดยมีความหนาผิวที่น้อยกว่าถึง 10-12 เท่า นอกจากนี้ การเพิ่มขึ้นของพื้นที่ผิวของตัวเร่ง เป็นการเพิ่มพื้นที่แอคทีฟไซต์ ส่งผลให้ อัตราการเกิดปฏิกิริยาเพิ่มขึ้นโดยจะสังเกตได้จากประมาณค่าความหนาแน่นกระแสไฟฟ้าที่เพิ่มขึ้น 7 เท่า และการเพิ่มขึ้นของการกระจายตัวของผลิตภัณฑ์ที่เกี่ยวกับทองแดงแผ่น ทองแดงพรุนที่ชุบด้วยคอปเปอร์ซัลเฟตที่มีความเข้มข้นมากขึ้น ให้การกระจายตัวของผลิตภัณฑ์มากที่สุด มากไปกว่านั้น แก๊สไฮโดรเจนเพิ่มขึ้น เมื่อให้แรงดันไฟฟ้าที่มากขึ้นแสดงด้วยผลการทดลองที่นาโนเทค หลังผ่านกระบวนการรีดักชันของคาร์บอนไดออกไซด์ อนุภาคของทองแดงมีการรวมกลุ่มกันมากขึ้นและมีการเปลี่ยนแปลงของลักษณะของรูพรุน และสารประกอบทางเคมี เมทานอลเป็นผลิตภัณฑ์หลักของปฏิกิริยาที่มีทองแดงพรุนเป็นตัวเร่ง ขณะเดียวกันยังพบ อัลดีไฮด์ แอลกอฮอล์ และเมทานอลอีกด้วย

ในกรณีของตัวเร่งทองแดงออกไซด์ที่ผลิตด้วยการอบให้ความร้อน เมื่อเวลาการอบคงที่ ผลของอุณหภูมิการอบส่งผลให้มีสารประกอบที่ผิวแตกต่างกัน  $\text{Cu}^+$  และ  $\text{Cu}^{2+}$  ถูกตรวจจับบนผิวของชิ้นงานทองแดงออกไซด์ที่อบที่อุณหภูมิ 300 และ 500 องศาเซลเซียส เช่นเดียวกับทองแดงแผ่น ในขณะที่  $\text{Cu}^0$  ถูกตรวจจับบนผิวของชิ้นงานทองแดงออกไซด์ที่อบที่อุณหภูมิ 800 และ 1,000 องศาเซลเซียสเท่านั้น มีอนุภาคของทองแดงบนผิวของชิ้นงาน โดยเฉพาบนผิวของชิ้นงานทองแดงออกไซด์ที่อบที่อุณหภูมิ 300 และ 500 องศาเซลเซียส ชิ้นงาน ทองแดงออกไซด์ที่อบที่อุณหภูมิ 300 องศาเซลเซียส เป็นชิ้นงานเดียวที่ไม่แตก ผลอัตราการเกิดปฏิกิริยาของตัวเร่งทองแดงออกไซด์สูงกว่าของทองแดงแผ่น อีกทั้งยังพบอัลดีไฮด์เป็นหนึ่งในผลิตภัณฑ์อีกด้วย ยิ่งไปกว่านั้น ชิ้นงานทองแดงพรุนที่ผ่านการอบให้ความร้อนซึ่งเกิดจากการรวมกันของทองแดงพรุนและทองแดงออกไซด์ สามารถเพิ่มอัตราการเกิดปฏิกิริยาได้มากถึง 9 เท่าเมื่อเทียบกับทองแดงแผ่น และ 4 เท่าของทองแดงพรุน สารเคมีมีค่าหลายชนิดถูกผลิตขึ้น โดยพบว่าเมทานอลเป็นผลิตภัณฑ์หลัก อีกทั้งยังมีสารเคมีที่มีค่าอื่นๆ เช่น เอ็น-โพรพานอล, โกลคอลลีไฮด์, โพรพิโอนาลดีไฮด์ อีกด้วย  $\text{Cu}^+$  และ  $\text{Cu}^{2+}$  ถูกตรวจจับบนผิวของทองแดงพรุนที่ผ่านการอบให้ความร้อนทั้งก่อนและหลังผ่านกระบวนการรีดักชันของคาร์บอนไดออกไซด์ แสดงให้เห็นว่าตัวเร่งนี้มีความเสถียรมากกว่าทองแดงพรุน สามารถสรุปได้ว่า การพัฒนาโครงสร้าง และทางเคมี สามารถเพิ่มประสิทธิภาพของตัวเร่งในกระบวนการรีดักชันของคาร์บอนไดออกไซด์ได้

สาขาวิชา วิทยาศาสตร์นาโนและเทคโนโลยี  
ปีการศึกษา 2565

ลายมือชื่อนิติ .....  
ลายมือชื่อ อ.ที่ปรึกษาหลัก .....  
ลายมือชื่อ อ.ที่ปรึกษาร่วม .....

# # 6087841520 : MAJOR NANOSCIENCE AND TECHNOLOGY

KEYWORD: Electrochemical, Carbon dioxide reduction reaction (CO<sub>2</sub>RR), Copper oxide, Nanoporous, Catalyst

Jidsucha Darayen : Nanoporous Cu-based catalytic electrodes for electrochemical conversion of carbon dioxide.

Advisor: Prof. Dr. YUTTANANT BOONYONGMANEERAT Co-advisor: Prof. Dr. ORAWON CHAILAPAKUL

This research investigates the strategies to enhance copper electrodes for carbon dioxides reduction reactions (CO<sub>2</sub>RR) for generation of valuable chemical products, including methanol and acetaldehyde. Through modifications of physical characteristics of electroplated copper electrodes, particularly introduction of porosity, and chemical composition, namely formation of copper oxides, the key performance parameters for CO<sub>2</sub>RR including selectivity, Faradaic efficiency, and energy efficiency are examined. Furthermore, the relationships between copper electrodes' plating variables (current density, deposition time, and bath solution), porosity and compositions, and corresponding CO<sub>2</sub>RR performances are constructed. The study has demonstrated that the ratio of CuSO<sub>4</sub> and H<sub>2</sub>SO<sub>4</sub> of bath solution, current density, and deposition time influence the obtained porous structure as confirmed by microstructural and physical evaluations (apparent and true porosity, 2D-morphology, surface roughness, BET surface area and BJH pore distribution).

With controlling concentration of H<sub>2</sub>SO<sub>4</sub>, it was found that more concentration of CuSO<sub>4</sub> increase the amount of copper deposit on the substrate creating a porous copper with higher apparent porosity but identical pore size. HCl minimize the size of porous branch causing the highest apparent pore size and porosity. All constant-current porous coppers were mesoporous materials (2-50 nm pore size). The arrangement of copper particle as grape seed on the dendrite structure of porous copper which fabricated in 0.2 M CuSO<sub>4</sub> without HCl providing the highest true surface area as 19.56 m<sup>2</sup>/g. This value is higher than of other porous coppers approximately 5-6 times. The apparent density, electrodeposition efficiency, and true porosity calculation was also confirmed that porous copper with higher concentration of CuSO<sub>4</sub> was the densest porous structure. Both bulk and surface chemical composition of porous coppers were slightly different from copper foil. Cu<sup>+</sup> and Cu<sup>2+</sup> were detected on the surface of copper foil and porous coppers but Cu<sup>0</sup> was detected only on the surface of porous copper which fabricated with HCl. Moreover, pulse electrodeposition was another method which can used to fabricate the denser porous structure manifested by the 10-12 times lower value of surface roughness. Furthermore, increase in surface area of catalytic electrode cause increase in active site as a result of increasing rate of reaction as shown by the approximately 7 times higher of current density with product distribution enhancement of porous coppers compared with copper foil. Porous copper with higher concentration of CuSO<sub>4</sub> provide the highest product distribution, moreover, H<sub>2</sub> increase with higher applied voltage as presented in the result which performed at Nanotec. After passing through CO<sub>2</sub>RR, particles of copper had more agglomeration with change in apparent pore characteristic and chemical composition. Ethanol is a main product of porous copper electrocatalyst while aldehyde, ethylene and methanol were also detected.

In case of thermally-induced copper oxides catalytic electrode, with controlling oxidation time, oxidation temperature cause the different surface composition. Cu<sup>+</sup> and Cu<sup>2+</sup> were detected on the surface of oxidized copper at 300 and 500 as copper foil whereas Cu<sup>0</sup> was detected only on oxidized copper at 800 and 1,000. There were some copper particles on the surface, obviously the oxidized copper at 300 and 500. Only the oxidized copper at 300 was not broken after passing through the oxidation. Copper oxide catalyst provide higher rate of reaction of CO<sub>2</sub>RR than of copper foil. Acetaldehyde was detected by the oxidized copper catalyst. Furthermore, thermally-induced porous copper oxides which fabricated by combining the porous copper and copper oxide can deliver 9 and 4 times higher rate of reaction than copper foil and porous coppers, respectively. Ethanol is a main product whereas some rare valuable chemicals (i.e., n-propanol, glycolaldehyde, and propionaldehyde). Cu<sup>+</sup> and Cu<sup>2+</sup> were detected on the surface of thermally-induced porous copper oxides both before and after passing through the CO<sub>2</sub>RR process indicating that this electrocatalyst have more stability than porous coppers. It summarized that development in structure and chemistry can enhance the performance of electrocatalyst in CO<sub>2</sub>RR process.

Field of Study: Nanoscience and Technology

Academic Year: 2022

Student's Signature .....

Advisor's Signature .....

Co-advisor's Signature .....

## ACKNOWLEDGEMENTS

Jidsucha Darayen



# TABLE OF CONTENTS

	Page
ABSTRACT (THAI) .....	iii
ABSTRACT (ENGLISH).....	iv
ACKNOWLEDGEMENTS.....	v
TABLE OF CONTENTS.....	vi
1. Introduction .....	1
1.1) Definition.....	2
1.2) CO <sub>2</sub> conversion.....	2
1.3) Electrochemical CO <sub>2</sub> RR.....	3
1.4) Motivation, Problems, and Solution approach .....	5
2. Literature reviews .....	6
2.1) Electrode, Product, and Mechanism pathway .....	6
2.2) Copper electrode: possible products.....	8
2.3) Electrochemical reduction CO <sub>2</sub> to valuable chemicals (i.e., methanol) .....	11
2.4) Catalytic electrode development .....	12
2.5) Chemical composition development (kind of catalytic electrode) .....	13
2.6) Structural development.....	17
2.6.1) Crystallographic Texture.....	18
2.6.2) Nanoparticles (nano) .....	20
2.6.3) Porous Structure .....	22
2.6.4) Pulse electrodeposition of porous fabrication .....	25
3. Scope of experiments .....	27
3.1) Sample fabrication.....	27
Section1: Electrodeposited porous copper electrocatalysts.....	27
1.1) Constant-current electrodeposition.....	27
1.2) Pulse electrodeposition .....	28

Section 2: Thermally-oxidized copper electrocatalysts.....	28
Section 3: Copper oxide electrocatalysts thermally-induced from electrodeposited porous copper .....	29
3.2) Sample Characterization and Analysis.....	29
3.3) CO <sub>2</sub> RR Testing and Chemical Product Detection.....	30
4. Objectives .....	32
5. Experimental.....	32
5.1) Sample Preparation procedure.....	32
Section 1: Electrodeposited porous copper electrocatalysts.....	32
1.1) Constant-current electrodeposition .....	32
1.2) Pulse Electrodeposition.....	34
Section 2: Thermally-oxidized copper electrocatalysts.....	36
Section 3: Copper oxide electrocatalysts thermally-induced from electrodeposited porous copper .....	36
5.2) CO <sub>2</sub> reduction reaction .....	37
6. Result and discussion .....	40
Section 1: Electrodeposited porous copper electrocatalysts .....	40
1.1) Porous copper fabrication.....	40
1.1.1) Constant-current electrodeposition.....	40
1.1.2) Pulse Electrodeposition .....	41
1.2 Sample characterization .....	42
1.2.1) Surface morphology and pore characteristics of constant-current porous copper .....	42
1.2.1.1) Surface morphology and pore characteristics .....	42
1.2.1.2) 3D-Surface roughness .....	47
1.2.1.3) True surface area and pore distribution.....	49
1.2.1.4) Apparent density, Electrodeposition efficiency, and True porosity calculation .....	51
1.2.2) Surface morphology and pore characteristics of pulse electrodeposited porous copper .....	52
1.2.3) Chemical composition.....	56

1.3 CO <sub>2</sub> electrochemical conversion tests (with Cu foil as baseline) .....	59
1.3.1) CO <sub>2</sub> RR result of porous coppers compared with copper foil (tested at Chemical engineering, Chulalongkorn University) .....	59
1.3.2) CO <sub>2</sub> RR result of porous B-3-40 compared with copper foil (tested at National Nanotechnology Center (NANOTEC), NSTDA) .....	65
1.3.2.1) CO <sub>2</sub> electrochemical conversion result .....	65
1.4 Analysis .....	74
Section 2: Thermally-induced copper oxides and CO <sub>2</sub> conversion performance ....	75
2.1) Copper oxide fabrication .....	75
2.2) Sample characterization .....	75
2.3 CO <sub>2</sub> electrochemical conversion tests (with Cu foil as baseline) .....	78
2.4 Analysis .....	81
Section 3: Thermally-induced copper oxides from porous copper .....	81
3.1 Fabrication method .....	81
3.2 Sample characterization .....	81
3.3 CO <sub>2</sub> electrochemical conversion tests .....	85
3.4 Analysis .....	86
7. Conclusion .....	87
8. Reference .....	89
Appendix: Copper foil .....	95
REFERENCES .....	99
VITA .....	101

## LIST OF FIGURES

Figure 1 Sources of CO <sub>2</sub> emission [1].	1
Figure 2 Development of global CO <sub>2</sub> emissions from fuel combustion and CO <sub>2</sub> concentration in the atmosphere [2].	1
Figure 3 The electrochemical CO <sub>2</sub> RR [19].	4
Figure 4 Periodic table for CO <sub>2</sub> reduction products at -2.2V vs. SCE in low-temperature 0.05 mol dm <sup>-3</sup> KHCO <sub>3</sub> solution [25].	7
Figure 5 CO <sub>2</sub> reduction metal classification by their binding energy of CO [29].	7
Figure 6 simple mechanism pathway of CO <sub>2</sub> RR [23].	8
Figure 7 Products of CO <sub>2</sub> reduction along with the number of electron requirement of CO <sub>2</sub> RR product formation [16].	10
Figure 8 (a) the faradaic efficiency and (b) Tafel plot of the partial current going to each product produced by Cu catalyst [16].	11
Figure 9 mechanism pathway of methanol in CO <sub>2</sub> RR [47].	12
Figure 10 Methanol production rate of electrodeposited, oxidized, and anodized Cu catalysts. [44]	14
Figure 11 Oxide formation on Cu surface by (a) thermal oxidation (heating) and (b) electrochemical oxidation (anodization).	17
Figure 12 Two approaches for electrochemical characterization of defect effects on CO <sub>2</sub> reduction. (A) Bulk electrolysis of a well-defined polycrystalline Au electrode within a glass, two-compartment H cell. (B) SECCM using a ~300-nm nanopipette electrochemical cell [68].	19
Figure 13 A schematic diagram of a nanostructure characteristic [70].	20
Figure 14 Faradaic efficiency for the products of electroreduction of CO <sub>2</sub> on three surfaces in CO <sub>2</sub> -saturated 0.1 M KClO <sub>4</sub> upon -1.1 V vs. RHE, including Sample A (electropolished surface), Sample B (copper nanoparticle-covered surface) and Sample C (sputtered surface) [69].	21
Figure 15 SEM image of the Cu oxide nanomaterials. (a) belonged to Cu oxide NWs (b) belonged to Cu oxide NNs [17].	22
Figure 16 Comparison of the CO <sub>2</sub> reduction activities on Cu NWs and NNs in the solution of 0.1 molL <sup>-1</sup> KHCO <sub>3</sub> at 10°C. (a) FEs for CH <sub>4</sub> and C <sub>2</sub> H <sub>4</sub> , (b) FEs for H <sub>2</sub> and HCOOH [17].	22

Figure 17 The effect of electrodeposition factors; (a) current density (b) deposition temperature on the average grain size [76].	23
Figure 18 (a) Scheme for preparing of Cu mesoporous electrodes synthesis and SEM images of Cu electrodes mesopores with (b) 30 nm width/40 nm depth (30 nm/40 nm), (c) 30 nm width/70 nm depth (30 nm/70 nm), and (d) 300 nm width/40 nm depth (300 nm/40 nm) [31].	23
Figure 19 Electrodeposited copper form with varied deposition time for (a) 5s; (b) 10s; (c) 15s; (d) 30s; and (e) 60s, moreover, (f) nanostructure of the electrodeposited foams [32].	24
Figure 20 Current density of smooth copper (red line) and copper foam (black and blue lines) plotted as a function of electrolyte concentration, where the electrolyte was $\text{KHCO}_3$ saturated with $\text{CO}_2$ and the step potential was $-1.8 \text{ V}$ [32].	25
Figure 21 Structure of pulse electrodeposited porous copper: (a) Honeycomb-like structure, (b) Non coalescence hole, (c) Coalescence hole, and (d) Cauliflower-like agglomerates [87].	26
Figure 22 Schematic of $\text{CO}_2\text{RR}$ test.	31
Figure 23 the overview of operation consisting of (a) $\text{CO}_2\text{RR}$ and (b) product detection.	31
Figure 24 Constant-current electrodeposition.	32
Figure 25 A stack up of different size of hydrogen bubbles which fabricated by Dynamic hydrogen bubble template (DHBT).	33
Figure 26 The pulse electrodeposition set up: (a) with electrolyte (b) copper foil cathode and platinum mesh anode.	35
Figure 27 The thermal oxidation set up	36
Figure 28 thermally-induced copper oxides from porous copper fabrication by combination of the best conditions of section 1 and section 2.	37
Figure 29 Schematic of $\text{CO}_2\text{RR}$ setup at Chemical Engineering, Chulalongkorn University.	39
Figure 30 Schematic of $\text{CO}_2\text{RR}$ setup at Nanotec, NSTDA.	40
Figure 31 Surface appearance of the constant-current porous copper in groups (a) A, (b) B, and (c) C varying by bath solution composition.	41
Figure 32 Surface appearance of the pulse electrodeposited porous copper P1-10, P4-10, P10-10 and P20-10, respectively which varying pulse on time: 1, 4, 10, and 20 ms, respectively with fixed pulse off time at 10 ms and current density $0.44 \text{ A/cm}^2$ ...	42



Figure 33 2D-Surface morphology of the constant-current porous copper in groups (a) A, (b) B, and (c) C varying by current density and deposition time. ....	43
Figure 34 Apparent pore size and apparent porosity of the constant-current porous copper in groups (a) A, (b) B, and (c) C varying by current density and deposition time. ....	44
Figure 35 OM image and Image J analysis of A-3-40, B-3-40, and C-3-40. ....	45
Figure 36 Apparent pore size and apparent porosity of A-3-40, B-3-40, and C-3-40 varying current density with deposition time 40 second. ....	45
Figure 37 The cross-sectioned microstructure of A-3-40, B-3-40 and C-3-40 with magnification 1000X: PX (in porous structure) and PX-IF (interface between porous structure and substrate).....	46
Figure 38 The cross-sectioned microstructure of A-3-40, B-3-40 and C-3-40 with magnification 4000X: PX (in porous structure) and PX-IF (interface between porous structure and substrate). ....	46
Figure 39 Microstructure of Cu foil (a–d), and porous Cu deposits from groups A (e–h), B (i–l), and C (m–p), electrodeposited with 3 A/cm <sup>2</sup> for 40 s, presented at different magnifications. ....	47
Figure 40 The 3D-morphology captured by 3D optical profiler and surface roughness value of constant-current porous coppers. ....	48
Figure 41 The correlation between surface roughness of the representative constant-current porous copper (A-3-40, B-3-40, and C-3-40). ....	48
Figure 42 Pore size of IUPAC classification system. ....	50
Figure 43 Isotherm plot of BET analysis and BJH pore distribution analysis results of A-3-40, B-3-40, and C-3-40.....	50
Figure 44 The process of cross-sectioned microstructure analysis of the porous coppers (a) the fabricated porous sample cut from the edge into almost of the middle of sample, (b) the cut sample dipped into the liquid nitrogen, (c) after separating the sample into 2 sides of sample, and (d) sample prepared to be analyzed by SEM .....	51
Figure 45 The 3D-morphology captured by 3D optical profiler and surface roughness value of pulse electrodeposited porous coppers with 40 s deposition time. ....	53
Figure 46 Surface roughness of constant-current porous coppers and pulse electrodeposition for 40 s deposition time. ....	54
Figure 47 The 3D-morphology captured by 3D optical profiler and surface roughness value of pulse electrodeposited porous coppers with 80 s deposition time. ....	54

Figure 48 Surface roughness of pulse electrodeposited porous coppers. ....	55
Figure 49 Microstructure of pulse electrodeposited porous copper which deposited for 40 and 80 seconds .....	55
Figure 50 Comparison of surface roughness and microstructure of the constant-current and pulse electrodeposited porous copper by controlling the applied current density at $0.44 \text{ A/cm}^2$ and deposition time for 40 seconds .....	56
Figure 51 EDX result of Cu foil and constant-current porous copper. ....	57
Figure 52 The XPS spectra of (a) copper foil (EP) and constant-current porous copper (b) PA (A-3-40), (c) PB (B-3-40), and (d) PC (C-3-40). ....	58
Figure 53 The ratio of oxidation state of copper foil (EP) and constant-current porous copper. ....	58
Figure 54 Representative NMR spectra obtained from the $\text{CO}_2\text{RR}$ experiments, using porous copper samples from groups (a) A, (b) B, and (c) C, electrodeposited with $3 \text{ A/cm}^2$ for 40 s, and (d) the copper foil as electrodes. ....	60
Figure 55 Rate of production of the chemical products of $\text{CO}_2\text{RR}$ obtained from Cu foil and porous A-3-40, B-3-40, and C-3-40, electrodeposited with $3 \text{ A/cm}^2$ for 40 seconds. ....	61
Figure 56 Selectivity of the chemical products of $\text{CO}_2\text{RR}$ obtained from Cu foil and porous A-3-40, B-3-40, and C-3-40, electrodeposited with $3 \text{ A/cm}^2$ for 40 seconds. ....	61
Figure 57 Faradaic efficiency of the chemical products of $\text{CO}_2\text{RR}$ obtained from Cu foil and porous A-3-40, B-3-40, and C-3-40, electrodeposited with $3 \text{ A/cm}^2$ for 40 seconds. ....	62
Figure 58 Microstructure of PX, PX1301, and PX1601 represents the porous coppers before passing through the $\text{CO}_2\text{RR}$ , after passing through the $\text{CO}_2\text{RR}$ at $-1.3 \text{ V}$ (Ag/AgCl), and at $-1.6 \text{ V}$ (Ag/AgCl), respectively. ....	62
Figure 59 (a) Apparent pore size and (b) apparent porosity of constant-current porous coppers. ....	63
Figure 60 EDX result of copper foil and constant-current porous coppers before and after passing through $\text{CO}_2\text{RR}$ . ....	64
Figure 61 The XPS spectra of the constant-current porous copper before passing through $\text{CO}_2\text{RR}$ (a) PA (A-3-40), (b) PB (B-3-40), (c) PC (C-3-40), and after passing through $\text{CO}_2\text{RR}$ at $-1.3 \text{ V}$ (Ag/AgCl) in $0.1 \text{ M KHCO}_3$ (d) PA1301, (e) PB1301, and (f) PC1301. ....	64

Figure 62 The ratio of oxidation state of copper foil (EP) and the constant-current porous copper before and after passing through at -1.3 V (Ag/AgCl) in 0.1M KHCO <sub>3</sub> . .....	65
Figure 63 The correlation between current (A) and time (s) of Cu1301, PB1301, PB1801, and PB2301 during CO <sub>2</sub> RR. ....	66
Figure 64 Representative NMR spectra obtained from the CO <sub>2</sub> RR experiments, using Cu foil in (a) catholytic and (b) anolytic parts, using B-3-40 running CO <sub>2</sub> RR at -1.3V (Ag/AgCl) in (c) catholytic and (d) anolytic parts, running CO <sub>2</sub> RR at -1.8V (Ag/AgCl) in (e) catholytic part, and running CO <sub>2</sub> RR at -2.3V (Ag/AgCl) in (e) catholytic part.....	67
Figure 65 CO <sub>2</sub> RR result of copper foil and constant-current porous coppers. ....	68
Figure 66 CO <sub>2</sub> RR result of Palmore's work. ....	69
Figure 67 SEM images of porous B-3-40 before and after passing through CO <sub>2</sub> RR with magnification 2000X, 5000X, and 15,000X.....	71
Figure 68 EDX result of Cu foil and porous B-3-40 before and after passing through at -1.3 V (Ag/AgCl) in 0.1M KHCO <sub>3</sub> .tested at Nanotec, NSTDA.....	71
Figure 69 The XPS spectra of the copper foil and the constant-current porous copper before passing through CO <sub>2</sub> RR (a) Cu (EP), (c) PB (B-3-40) and after passing through CO <sub>2</sub> RR: (b) Cu (1301), (d) PB1301 at -1.3 V (Ag/AgCl) and (e) PB2301 at -2.3 (Ag/AgCl) in 0.1M KHCO <sub>3</sub> , respectively.....	72
Figure 70 The ratio of the copper foil and the constant-current porous copper before passing through CO <sub>2</sub> RR (a) Cu (EP), (c) PB (B-3-40) and after passing through CO <sub>2</sub> RR: (b) Cu (1301), (d) PB1301 at -1.3 V (Ag/AgCl) and (e) PB2301 at -2.3 (Ag/AgCl) in 0.1M KHCO <sub>3</sub> , respectively.....	73
Figure 71 The capacitance of porous B-3-40.....	74
Figure 72 Appearance and 3D-morphology of A300, A500, A800, and A1000 fabricated by thermal oxidation in the furnace. ....	75
Figure 73 Morphology of oxidized coppers (A300, A500, A800, and A1000) captured at 2000X, 5000X, and 15000X. ....	76
Figure 74 EDX result of oxidized copper. ....	76
Figure 75 The XPS spectra of the thermally-induced copper oxides (a) A300, (b) A500, (c) A800, and (d) A1000. ....	77
Figure 76 The oxidation state of copper foil and the thermally-induced copper oxides A300, A500, A800, and A1000. ....	78

Figure 77 Faradaic efficiency of the chemical products of CO <sub>2</sub> RR obtained from Cu foil and the thermally-induced copper oxides (A300) at -1.3 V (Ag/AgCl) in 0.5 M KHCO <sub>3</sub> .	79
Figure 78 EDX result of copper foil and A300 before and after passing through CO <sub>2</sub> RR at -1.3 V (Ag/AgCl) in 0.5M KHCO <sub>3</sub> .	80
Figure 79 The XPS spectra of the copper foil and thermally-induced copper oxides before (a) Cu (EP), (b) A300 and after passing through CO <sub>2</sub> RR at -1.3 (Ag/AgCl) in 0.5M KHCO <sub>3</sub> (c) Cu_1305, and (d) A300_1305.	80
Figure 80 The ratio of oxidation state of the copper foil and thermally-induced copper oxides before (a) Cu (EP), (b) A300 and after passing through CO <sub>2</sub> RR at -1.3 (Ag/AgCl) in 0.5M KHCO <sub>3</sub> (c) Cu_1305, and (d) A300_1305.	81
Figure 81 (a) Apparent pore size and (b) apparent porosity of constant-current porous coppers, thermally-induced porous copper oxides, and thermally-induced porous copper oxides after passing through CO <sub>2</sub> RR at -1.3V (Ag/AgCl) in 0.1M KHCO <sub>3</sub> .	82
Figure 82 Morphology of thermally-induced porous copper oxides captured at 2000X, 5000X, and 15000X.	83
Figure 83 Morphology of thermally-induced porous copper oxides after passing through the CO <sub>2</sub> RR at -1.3 V (Ag/AgCl) in 0.1M KHCO <sub>3</sub> captured at 2000X, 5000X, and 15000X.	83
Figure 84 EDX result of thermally-induced porous copper oxides, and thermally-induced porous copper oxides after passing through CO <sub>2</sub> RR at -1.3V (Ag/AgCl) in 0.1M KHCO <sub>3</sub> .	84
Figure 85 The XPS spectra of the constant-current porous copper before passing through CO <sub>2</sub> RR (a) PAA300, (b) PBA300, (c) PCA300 and after passing through CO <sub>2</sub> RR at -1.3 V (Ag/AgCl) in 0.1M KHCO <sub>3</sub> (d) PAA300_1301, (e) PBA300_1301, and (f) PCA300_1301.	84
Figure 86 The ratio of the oxidation state of the constant-current porous copper before passing through CO <sub>2</sub> RR (a) PAA300, (b) PBA300, (c) PCA300 and after passing through CO <sub>2</sub> RR at -1.3 V (Ag/AgCl) in 0.1M KHCO <sub>3</sub> (d) PAA300_1301, (e) PBA300_1301, and (f) PCA300_1301.	85
Figure 87 CO <sub>2</sub> RR result of copper foil and of thermally-induced porous copper oxides at -1.3V (Ag/AgCl) in 0.1M KHCO <sub>3</sub> .	86
Figure A1 the detailed chemical composition of copper foil.	95
Figure 2 EDX result of copper foil.	96
Figure A3 XPS profile and oxidation state of copper foil.	96

Figure A4 Capacitance experiment of copper foil. ....	97
Figure A5 CO <sub>2</sub> RR electrolyzer (1) the conventional H-cell and (b) the flat cell. ....	98
Figure A6 CO <sub>2</sub> RR result of copper foil which tested by H-cell and flat cell electrolyzer.....	98

## LIST OF TABLES

Table 1 Pros and cons of each method of CO <sub>2</sub> RR. ....	3
Table 2 Reaction equations during electrochemical CO <sub>2</sub> RR. ....	4
Table 3 Faradaic Efficiencies of CO <sub>2</sub> Reduction Products on Metal Electrodes in CO <sub>2</sub> -Saturated 0.1 M KHCO <sub>3</sub> (pH = 6.8) [20]. ....	6
Table 4 Electrochemical potentials of possible CO <sub>2</sub> reduction reactions in aqueous solutions for the production of different hydrocarbon fuels [19]. ....	9
Table 5 Cu-based electrode for methanol formation in CO <sub>2</sub> RR. ....	14
Table 6 Cu-oxide reduction reactions and their standard electrode potential (E <sup>0</sup> ) [59]. ....	15
Table 7 Other kinds of developed electrode for methanol formation in CO <sub>2</sub> RR.....	16
Table 8 Products from the electrochemical reduction of CO <sub>2</sub> at Cu single crystal electrodes [64].....	18
Table 9 Product distribution in the electrochemical reduction of CO <sub>2</sub> at a series of copper single crystal electrodes Cu(S)- [n (111) x (111)] and Cu(S)- [n (110) x (100)] [65].....	18
Table 10 Onset Potentials (V vs RHE) and corresponding partial current densities for various CO <sub>2</sub> RR Products on Cu <sub>2</sub> O-derived Cu was compared to the Cu single-crystal electrodes consisting of Cu (100), Cu (111), and Cu (110) in CO <sub>2</sub> in the saturated 0.1 M KHCO <sub>3</sub> electrolyte [24]. ....	20
Table 11 Sample analysis.....	30
Table 12 Parameters of constant-current porous copper fabrication. ....	34
Table 13 Parameters of pulse electrodeposited porous copper fabrication.....	35
Table 14 Parameters of thermally-induced copper oxides fabrication. ....	36
Table 15 Parameters of thermally-induced porous copper oxides fabrication. ....	37
Table 16 CO <sub>2</sub> RR setup at Chemical Engineering, Chulalongkorn University. ....	38

Table 17 CO <sub>2</sub> RR setup at Nanotec, NSTDA. ....	39
Table 18 Pore characteristics of Porous A-3-40, Porous B-3-40, and Porous C-3-40 copper. ....	49
Table 19 Calculation for pore characteristics. ....	52
Table 20 Comparison of the CO <sub>2</sub> RR result between this work and the Palmore's work. .....	70
Table 21 the XRD result of Hugo's work. ....	77



# 1. Introduction

The amount of carbon dioxide (CO<sub>2</sub>), a greenhouse gas (GHG), has increased exponentially. **Error! Not a valid bookmark self-reference.** shows that all of the varied sources of CO<sub>2</sub> emission fossil fuel combustion is the main source which consists of electricity and heat generation, transportation, industry, residential and others for 41, 22, 20, 6 and 10 percent, respectively .

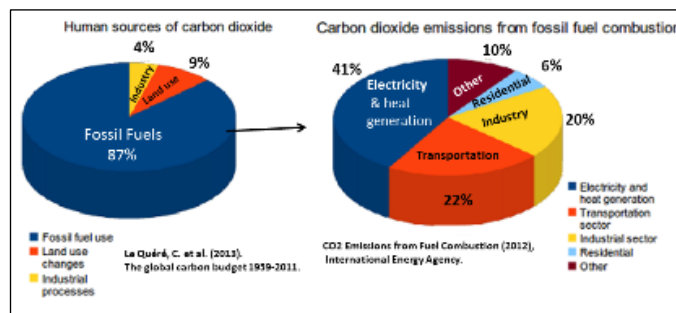


Figure 1 Sources of CO<sub>2</sub>emission [1].

According to Figure 2 [2], CO<sub>2</sub> emissions develops from fuel combustion and global atmospheric carbon dioxide. At the present, a main source of CO<sub>2</sub> emission is fuel combustion, approximately 33,000 Mega tons (Mt), and CO<sub>2</sub> concentration in the atmosphere is around 400 ppm. According to American Society of Heating and Air-Conditioning Engineers (ASHRAE), CO<sub>2</sub> concentration in the atmosphere should not reach to 1,000 ppm [3]. Therefore, excess CO<sub>2</sub> is a global problem causing the climate change and other environmental damages.

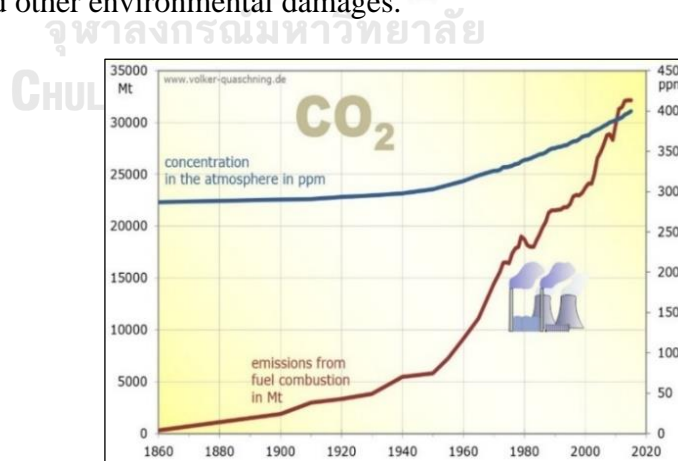


Figure 2 Development of global CO<sub>2</sub> emissions from fuel combustion and CO<sub>2</sub> concentration in the atmosphere [2].

Since CO<sub>2</sub>RR (CO<sub>2</sub> reduction reaction) is a rather specific field consisting of many terminologies (i.e., catalytic activity, current density, energy efficiency, selectivity), they are defined their meanings as following to avoid the misunderstanding or confusing.

### 1.1) Definition

1.1.1) Catalytic activity: the increase in rate of a chemical reaction caused by the presence of a catalyst.

1.1.2) Current density (i): the amount of charge per unit time that flows through a unit area of a chosen cross section.

1.1.3) Energy efficiency (EE): the goal to reduce the amount of energy required to provide products and services. For CO<sub>2</sub>RR, it can be calculated by equation (1).

$$\epsilon_{(\text{energetic})} = \sum_k \frac{E_k^0 \epsilon_{k, \text{Faradaic}}}{E_k^0 + \eta} \quad (1)$$

1.1.4) Faradaic efficiency (FE): the efficiency with which charge (electrons) is transferred in a system facilitating an electrochemical reaction. For CO<sub>2</sub>RR, it can be calculated by equation (2).

$$\epsilon_{(\text{Faradaic})} = \frac{z \cdot n \cdot F}{Q} \quad (2)$$

1.1.5) Reaction rate: the speed at which reactants are converted into products.

1.1.6) Overpotential ( $\eta$ ): the potential difference (voltage) between a half-reaction's thermodynamically determined reduction potential and the potential at which the redox event is experimentally observed.

Moreover, the criteria of desirable catalyst consist of high catalytic activity (high reaction rate), low energy consumption (low overpotential), high selectivity (high faradaic efficiency: FE), and high stability (repeatability).

### 1.2) CO<sub>2</sub> conversion

In General, there are two main approaches of CO<sub>2</sub> management. The first method is CO<sub>2</sub> capture and storage (CCS) [4, 5]. CO<sub>2</sub> has been stored in the land, sea, and stone. Therefore, CO<sub>2</sub> storage requires a lot of areas. For a long term, CO<sub>2</sub> capture is not a practical way because of risks of getting explosion, high-cost process, and



storage capacity limitations. On the other hand, the second method is CO<sub>2</sub> reduction (CCR). CO<sub>2</sub> can be converted or reduced to other higher value-added chemicals such as hydrocarbons and oxygenates [6]. Therefore, CO<sub>2</sub> in the atmosphere will be reduced while other chemicals can be produced. CO<sub>2</sub> conversion is a reduction reaction called CO<sub>2</sub> reduction reaction process or CO<sub>2</sub>RR. This method receives a lot of attention because it is more practical and sustainable method than CCS. There are many ways of CCR (i.e., thermochemical, photochemical, electrochemical means as well as hydrogenation) [7-15]. Each method has different pros and cons as presented in Table 1.

Four main techniques of CO<sub>2</sub>RR are compared. Thermochemical is a simple process but high temperature/energy are required. Hydrogenation is used in the wide range for methanol synthesis of syngas, but it is not only a highly flammable and explosive but also easily diffusing process. Moreover, hydrogenation process is an expensive method because high energy is required. Photochemical and electrical methods are clean and environmentally friendly processes. However, photochemical has been studied in the wide range. Some researchers discovered that faradaic efficiency is declined with the reaction going on by using some material as a catalyst. Moreover, light which is used as a source of energy is another limitation.

Therefore, in this research, electrochemical reduction method is selected to study because this method is also a clean process. It is an inexpensive method. It can be operated at room temperature and provide higher production rate and conversion at mild condition [16-18]. Nevertheless, there are some limitations of selectivity and current density when producing more than 2 electrons transfer products such as methanol, ethylene etc. (except CO and formate; 2 electrons transfer product).

Table 1 Pros and cons of each method of CO<sub>2</sub>RR.

CO <sub>2</sub> RR	Pros	Cons
Thermochemical	- Simple process	- High temperature process - High energy requirement
Hydrogenation	- Generally used in the wide range to produce methanol	- Highly flammable - Explosive - Diffuse easily - Expensive - High energy consumption
Photochemical	- Clean process - Environmental friendly - High efficiency processing	- Some material show that the faraday efficiency decline with the reaction going on
Electrochemical	- Can be operated at room temperature - Clean Process - Inexpensive - Provide higher production rate & conversion at mild condition	- Low selectivity - Low current density (approx. 100 times compared to 2 e <sup>-</sup> products i.e. CO, formate)

### 1.3) Electrochemical CO<sub>2</sub>RR

The electrochemical reduction of CO<sub>2</sub>RR is operated by consuming the electricity from other renewable energy sources such as wind or hydro energy. In case

of CO<sub>2</sub>RR, the electrochemical system consists of three electrodes, one proton exchange membrane (PEM) and electrolyte as illustrated in Figure 3 [19]. Electrodes contain working electrode (WE), counter electrode (CE), and reference electrode (RE). WE is a cathode while CE is an anode. Generally, noble metal is used as CE for making a stable electrode providing electron of electrochemical reaction. RE acts as a potential reference of the system.

The PEM is used for separating the system into two parts: catholytic and anolytic parts. Products which formed at catholytic part at cathode will not go through to the anolytic part. Therefore, products of both parts are not combined which simplify a product detection. Electrolyte is an intermediate which is used to facilitate the charge transferring between electrodes (i.e., KHCO<sub>3</sub>, NaHCO<sub>3</sub>, NaSO<sub>4</sub>)

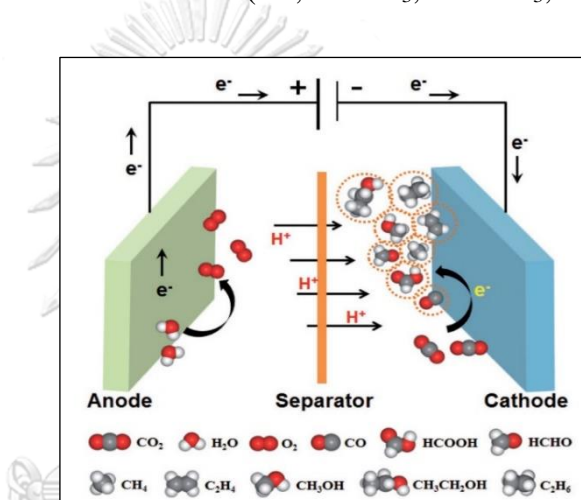


Figure 3 The electrochemical CO<sub>2</sub>RR [19].

Table 2 Reaction equations during electrochemical CO<sub>2</sub>RR.

Electrode	Reaction name	Reaction equation
Cathode	CO <sub>2</sub> reduction reaction, CO <sub>2</sub> RR	$\text{CO}_2 + 6\text{H}^+ + 6\text{e}^- \rightarrow \text{CH}_3\text{OH} + \text{H}_2\text{O}$
	Hydrogen Evolution Reaction, HER	$2\text{H}^+ + 2\text{e}^- \rightarrow \text{H}_2$
Anode	Oxygen Evolution Reaction, OER	$2\text{H}_2\text{O} \rightarrow \text{O}_2 + 4\text{H}^+ + 4\text{e}^-$

During CO<sub>2</sub>RR, electrons are transferred from anode to cathode. At cathode, both CO<sub>2</sub>RR and Hydrogen evolution reaction (HER), the competitive reaction of CO<sub>2</sub>RR, occur at cathode by reduction reaction providing CO<sub>2</sub>RR products and H<sub>2</sub>, respectively. CO<sub>2</sub>RR product consists of carbon monoxide (CO), formate (HCOOH), methane (CH<sub>4</sub>), ethylene (C<sub>2</sub>H<sub>4</sub>), methanol (CH<sub>3</sub>OH), ethanol (C<sub>2</sub>H<sub>5</sub>OH) and other hydrocarbons and oxygenates. According to the FE, CO and formate can be produced as major products by CO<sub>2</sub>RR whereas other products are minor products. On the other hand, O<sub>2</sub> is produced at anode by oxidation reaction named Oxygen

evolution reaction (OER). Reaction equations at cathode and anode are shown in Table 2. HER should be suppressed to obtain higher selectivity of CO<sub>2</sub>RR products. Moreover, the morphology of cathode can also affect to the of rate product formation. Therefore, cathode acts as a catalytic electrode of CO<sub>2</sub>RR that affects both selectivity and activity. The different cathodes or catalytic electrodes have different catalytic performance. Catalytic electrode has been developed to obtain a suitable catalyst which is capable of achieving a stable and cost-effective process with high efficiency and selectivity at low over-potentials are the key technological challenges for the electrochemical reduction of CO<sub>2</sub>.

#### 1.4) Motivation, Problems, and Solution approach

According to CO<sub>2</sub>RR products which produced by copper catalytic electrode as mentioned previously, valuable chemicals (i.e., ethylene, methanol, ethanol, and acetaldehyde) were detected as a minor product of CO<sub>2</sub>RR. Although their selectivity and activity are low, they have a lot of benefits for the industrial field. For example, ethylene is used as a feedstock in the manufacture of plastics, fibers, and other organic chemicals. Methanol is a convenient and safe mean of storing energy without high pressures needed to store at room temperature, excellent fuel for combustion engines. Ethanol is used in the manufacture of drugs, plastics, and cosmetics. Acetaldehyde is used as a prior substance for chemicals production (i.e., acetic acid). At the present, some product formation by CO<sub>2</sub>RR has not been concentrated enough in the wide range. Their production can be enhanced by using a suitable catalytic electrode. Copper based catalytic electrode acts as an important candidate to overcome this limitation. Moreover, porous catalyst can enhance rate of reaction while copper-based electrode with proper composition can improve product selectivity. The study on the development of copper electrodes and study of processing parameters for copper electrodes for CO<sub>2</sub> conversion to valuable chemicals is very limited. Therefore, it is a reason why the purpose of this study is to maximize product yield as a desirable product to increase both selectivity and activity with minimal energy input by copper-based catalytic electrode development. This work will study the relationship of processing parameter of catalytic electrode fabrication and product formation in CO<sub>2</sub>RR.

## 2. Literature reviews

### 2.1) Electrode, Product, and Mechanism pathway

Since product formation depend on kind of material of catalytic electrode. Metal (i.e., Au, Ag, Zn, Sn, In, Pb, and Cu etc.) is generally used as a catalytic electrode for CO<sub>2</sub>RR [20-23]. According to Hori's work, he studied the effect of various metal electrode on product distribution. Table 3 shows the faradaic efficiencies of CO<sub>2</sub> reduction products on metal electrodes in CO<sub>2</sub>-Saturated 0.1 M KHCO<sub>3</sub> (pH = 6.8) [20].

Table 3 Faradaic Efficiencies of CO<sub>2</sub> Reduction Products on Metal Electrodes in CO<sub>2</sub>-Saturated 0.1 M KHCO<sub>3</sub> (pH = 6.8) [20].

Electrode	Potential vs. SHE V	Current density mA cm <sup>-2</sup>	Faradaic efficiency, %							
			CH <sub>4</sub>	C <sub>2</sub> H <sub>4</sub>	EtOH <sup>a</sup>	PrOH <sup>b</sup>	CO	HCOO <sup>-</sup>	H <sub>2</sub>	Total
Pb	-1.63	5.0	0.0	0.0	0.0	0.0	0.0	97.4	5.0	102.4
Hg	-1.51	0.5	0.0	0.0	0.0	0.0	0.0	99.5	0.0	99.5
Tl	-1.60	5.0	0.0	0.0	0.0	0.0	0.0	95.1	6.2	101.3
In	-1.55	5.0	0.0	0.0	0.0	0.0	2.1	94.9	3.3	100.3
Sn	-1.48	5.0	0.0	0.0	0.0	0.0	7.1	88.4	4.6	100.1
Cd	-1.63	5.0	1.3	0.0	0.0	0.0	13.9	78.4	9.4	103.0
Bi <sup>c</sup>	-1.56	1.2	-	-	-	-	-	77	-	-
Au	-1.14	5.0	0.0	0.0	0.0	0.0	87.1	0.7	10.2	98.0
Ag	-1.37	5.0	0.0	0.0	0.0	0.0	81.5	0.8	12.4	94.6
Zn	-1.54	5.0	0.0	0.0	0.0	0.0	79.4	6.1	9.9	95.4
Pd	-1.20	5.0	2.9	0.0	0.0	0.0	28.3	2.8	26.2	60.2
Ga	-1.24	5.0	0.0	0.0	0.0	0.0	23.2	0.0	79.0	102.0
Cu	-1.44	5.0	33.3	25.5	5.7	3.0	1.3	9.4	20.5	103.5 <sup>d</sup>
Ni	-1.48	5.0	1.8	0.1	0.0	0.0	0.0	1.4	88.9	92.4 <sup>e</sup>
Fe	-0.91	5.0	0.0	0.0	0.0	0.0	0.0	0.0	94.8	94.8
Pt	-1.07	5.0	0.0	0.0	0.0	0.0	0.0	0.1	95.7	95.8
Ti	-1.60	5.0	0.0	0.0	0.0	0.0	tr.	0.0	99.7	99.7

<sup>a</sup>ethanol; <sup>b</sup>n-propanol; <sup>c</sup>the data are taken from Hori et al.<sup>23</sup> except Bi which is read from an illustration in a paper by Kunugi et al.<sup>117</sup>; <sup>d</sup>the total value contains C<sub>3</sub>H<sub>5</sub>OH(1.4%), CH<sub>3</sub>CHO(1.1%), C<sub>2</sub>H<sub>5</sub>CHO(2.3%) in addition to the tabulated substances; <sup>e</sup>the total value contains C<sub>2</sub>H<sub>4</sub>(0.2%)

Metal electrode can be separated into four main groups. Sn, Hg, Pb are the examples of the first metal group which provide formate with high selectivity. The second metal group consists of Au, Ag, and Zn. They provide CO as a major product. Cu is an only metal electrode which can provide the most product distribution. CO, formate, hydrocabons (i.e., methane, ethylene), and some oxygenates (i.e., ethanol) can be produced in CO<sub>2</sub>RR by using Cu catalytic electrode [5, 12, 20, 21, 24]. The last metal group contains Pt, Fe, Ti, and Ni. They provide H<sub>2</sub> as the main products. In case of CO<sub>2</sub>RR, H<sub>2</sub> plays as a competitive product of other products. Therefore, the H<sub>2</sub> group can be ignored and H<sub>2</sub> is not considered as a product in the CO<sub>2</sub>RR mechanism pathway.

In addition to Table 3, Hori and his coworker [20] also classified these metals in the periodic table by kinds of product distribution with different symbols (CO, HCOOH, hydrocarbons, and H<sub>2</sub>) as shown in Figure 4 [25]. Moreover, the CO<sub>2</sub> reduction metal which is also classified by their binding energy of CO as presented in

Figure 5. Copper is a metal which has intermediate binding energy with CO causing various products can be produced by copper electrocatalyst.

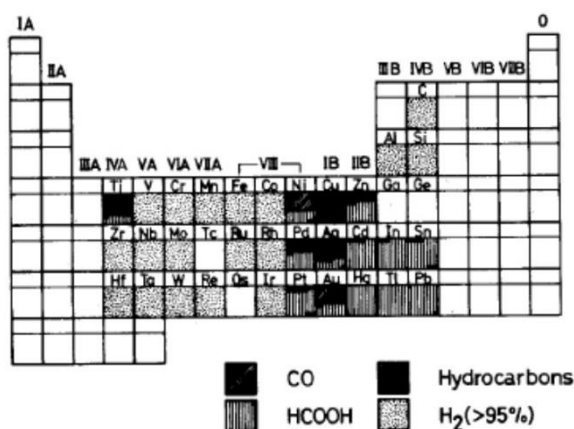


Figure 4 Periodic table for CO<sub>2</sub> reduction products at -2.2V vs. SCE in low-temperature 0.05 mol dm<sup>-3</sup> KHCO<sub>3</sub> solution [25].

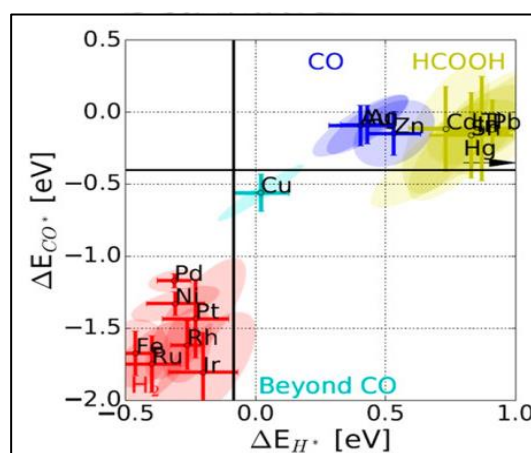


Figure 5 CO<sub>2</sub> reduction metal classification by their binding energy of CO [29].

The result of the electrode effect can be related to the mechanism pathway of CO<sub>2</sub>RR. This mechanism pathway shows the pathway of electron and proton transfer beginning from CO<sub>2</sub> until turning to another product during reduction reaction of CO<sub>2</sub>. It can explain which intermediates are formed during each product formation.

Some prior studies have been conducted to achieve the understanding of the mechanism of CO<sub>2</sub>RR which depends on the setup and parameters employed in the process. Among the CO<sub>2</sub>RR products, CO and formate formation require only two electrons in CO<sub>2</sub>RR. This is a reason why a formation requires relatively low overpotential. On the other hand, hydrocarbons, alcohols and other oxygenates are found only at higher applied voltage. Electron transfer and intermediate specie formation are important factors. Therefore, it is necessary to consider understanding CO<sub>2</sub>RR mechanism. When CO<sub>2</sub> gains the first electron, it can be served as

intermediate specie ( $\text{C O}_2^*$ ). Moreover, during electron and proton transfer, other intermediates which adsorb on the surface are changing along the pathway. If  $\text{C O}_2^*$  gains only one more pair of proton and electron, formate will be formed as a product. In addition to another important intermediate is  $\text{CO}^*$ . It can desorb from the catalytic electrode surface providing CO as the product. On the other hand, it can still be on the catalytic electrode surface for being further reduced to other products which requires two more electrons. For this way,  $\text{CO}^*$  can gain more electron to form new chemicals and then desorb as the obtained products. This phenomenon is very influenced and controlled by material types of the working electrodes (catalytic electrode).

In case of CO formation, Au, Ag, and Zn can bind with  $\text{CO}_2^*$  intermediate but not reduce CO further. It can imply that their binding energy with CO of these metals are weak. Therefore, CO is got rid of as a product easily [26]. For formate formation, Sn, Pb, and In can bind with weakly with  $\text{CO}_2^*$  intermediate so, formate is formed [27, 28]. In additions, hydrocarbons and oxygenates (i.e., alcohols) can be produced by Cu because Cu can bind with  $\text{CO}_2^*$  intermediate and can also reduce CO further. A simple mechanism pathway of  $\text{CO}_2\text{RR}$  are illustrated in Figure 6 [23].

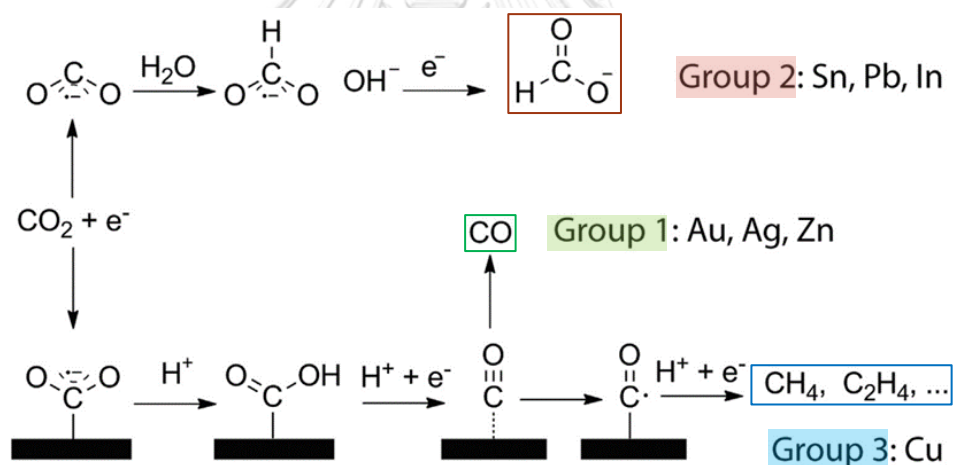


Figure 6 simple mechanism pathway of  $\text{CO}_2\text{RR}$  [23].

Figure 5 illustrates the value of binding energy with CO of each metal [29]. These metals can also be separated into three groups similar as in the groups of metal that shown in the mechanism pathway (Figure 6). Considering the CO binding energy and mechanism pathway, these can conclude that copper is a unique metal because it has the intermediate binding energy with CO compared to other metals such as Au, Ag, Cd, Hg, and Fe. This is a reason why it can provide various products [11, 16, 20, 21, 23, 30-34].

## 2.2) Copper electrode: possible products

Based on Cu catalytic electrode, Kendra and her coworkers discovered the state-of-art research in 2012. They presented that as much as 16 products can be



produced by using copper (Cu) catalytic electrode. Each product formation requires different number of electrons. Moreover, each product requires different magnitude of potential to form. Examples of CO<sub>2</sub>RR reaction are contained in Table 4 [19]. CO and formate require only two electrons while other products require more than two electrons up to 18 electrons for 1-propanal formation as presented in Figure 7 [16].

Table 4 Electrochemical potentials of possible CO<sub>2</sub> reduction reactions in aqueous solutions for the production of different hydrocarbon fuels [19].

Possible half-reactions of electrochemical CO <sub>2</sub> reduction	Electrode potentials (V vs SHE) at pH 7
$\text{CO}_2 (\text{g}) + \text{e}^- \rightarrow \text{*COO}^-$	-1.90
$\text{CO}_2 (\text{g}) + 2\text{H}^+ + 2\text{e}^- \rightarrow \text{HCOOH} (\text{l})$	-0.61
$\text{CO}_2 (\text{g}) + \text{H}_2\text{O} (\text{l}) + 2\text{e}^- \rightarrow \text{HCOO}^- (\text{aq}) + \text{OH}^-$	-0.43
$\text{CO}_2 (\text{g}) + 2\text{H}^+ + 2\text{e}^- \rightarrow \text{CO} (\text{g}) + \text{H}_2\text{O} (\text{l})$	-0.53
$\text{CO}_2 (\text{g}) + \text{H}_2\text{O} (\text{l}) + 2\text{e}^- \rightarrow \text{CO} (\text{g}) + 2\text{OH}^-$	-0.52
$\text{CO}_2 (\text{g}) + 4\text{H}^+ + 2\text{e}^- \rightarrow \text{HCHO} (\text{l}) + \text{H}_2\text{O} (\text{l})$	-0.48
$\text{CO}_2 (\text{g}) + 3\text{H}_2\text{O} (\text{l}) + 4\text{e}^- \rightarrow \text{HCHO} (\text{l}) + 4\text{OH}^-$	-0.89
$\text{CO}_2 (\text{g}) + 6\text{H}^+ + 6\text{e}^- \rightarrow \text{CH}_3\text{OH} (\text{l}) + \text{H}_2\text{O} (\text{l})$	-0.38
$\text{CO}_2 (\text{g}) + 5\text{H}_2\text{O} (\text{l}) + 6\text{e}^- \rightarrow \text{CH}_3\text{OH} (\text{l}) + 6\text{OH}^-$	-0.81
$\text{CO}_2 (\text{g}) + 8\text{H}^+ + 8\text{e}^- \rightarrow \text{CH}_4 (\text{g}) + 2\text{H}_2\text{O} (\text{l})$	-0.24
$\text{CO}_2 (\text{g}) + 6\text{H}_2\text{O} (\text{l}) + 8\text{e}^- \rightarrow \text{CH}_4 (\text{g}) + 8\text{OH}^-$	-0.25
$2\text{CO}_2 (\text{g}) + 12\text{H}^+ + 12\text{e}^- \rightarrow \text{C}_2\text{H}_4 (\text{g}) + 4\text{H}_2\text{O} (\text{l})$	0.06
$2\text{CO}_2 (\text{g}) + 8\text{H}_2\text{O} (\text{l}) + 12\text{e}^- \rightarrow \text{C}_2\text{H}_4 (\text{g}) + 12\text{OH}^-$	-0.34
$2\text{CO}_2 (\text{g}) + 12\text{H}^+ + 12\text{e}^- \rightarrow \text{CH}_3\text{CH}_2\text{OH} (\text{l}) + 3\text{H}_2\text{O} (\text{l})$	0.08
$2\text{CO}_2 (\text{g}) + 9\text{H}_2\text{O} (\text{l}) + 12\text{e}^- \rightarrow \text{CH}_3\text{CH}_2\text{OH} (\text{l}) + 12\text{OH}^- (\text{l})$	-0.33

Currently, according to CO<sub>2</sub>RR products, CO and formate have been studied a lot. Their selectivity can reach to approximately 100 percent by gold (Au) and tin (Sn), respectively [30, 35]. Methane and ethylene are the main hydrocarbons which can be produced with the acceptable selectivity. Moreover, ethanol and other oxygenates can also be produced. Many researchers have developed the catalytic performance of catalytic electrode to improve selectivity and activity of desirable products. However, methanol (an alcohol consisting of only one atom of carbon) should be produced easily. It is difficulty produced due to the complicated CO<sub>2</sub>RR mechanism pathway of methanol formation. Therefore, electrode can affect to CO<sub>2</sub>RR products and their mechanism pathway.

Product	# e <sup>-</sup>	E	Product	# e <sup>-</sup>	E
<b>Formate</b> 	2	-0.02	<b>Acetaldehyde</b> 	10	0.05
<b>Carbon monoxide</b> 	2	-0.10	<b>Ethanol</b> 	12	0.09
<b>Methanol</b> 	6	0.03	<b>Ethylene</b> 	12	0.08
<b>Glyoxal</b> 	6	-0.16	<b>Hydroxyacetone</b> 	14	0.46
<b>Methane</b> 	8	0.17	<b>Acetone</b> 	16	-0.14
<b>Acetate</b> 	8	-0.26	<b>Allyl alcohol</b> 	16	0.11
<b>Glycolaldehyde</b> 	8	-0.03	<b>Propionaldehyde</b> 	16	0.14
<b>Ethylene glycol</b> 	10	0.20	<b>1-Propanol</b> 	18	0.21

Figure 7 Products of CO<sub>2</sub> reduction along with the number of electron requirement of CO<sub>2</sub>RR product formation [16].

For instance, there is a report of faradaic efficiency and current density of 16 products which were formed by using copper foil as a catalytic electrode in CO<sub>2</sub>RR as illustrated in Figure 8 [16]. Products are divided into three groups: (1) major products (H<sub>2</sub>, CO, formate, methane, and ethylene) (2) intermediate products (ethanol, n-propanol, allyl alcohol) and (3) minor products (methanol, acetate, acetone, aldehydes etc.). FE of major products was approximately up to 80 percent while FE of intermediate products was less than or equal 10 percent. In case of minor products, FE is very low with the 1 decimal point percent. However, it can imply that if using more suitable material as a catalytic electrode, the FE of these minor products may be higher. Therefore, the development of catalytic electrode is needed to enhance their FE.



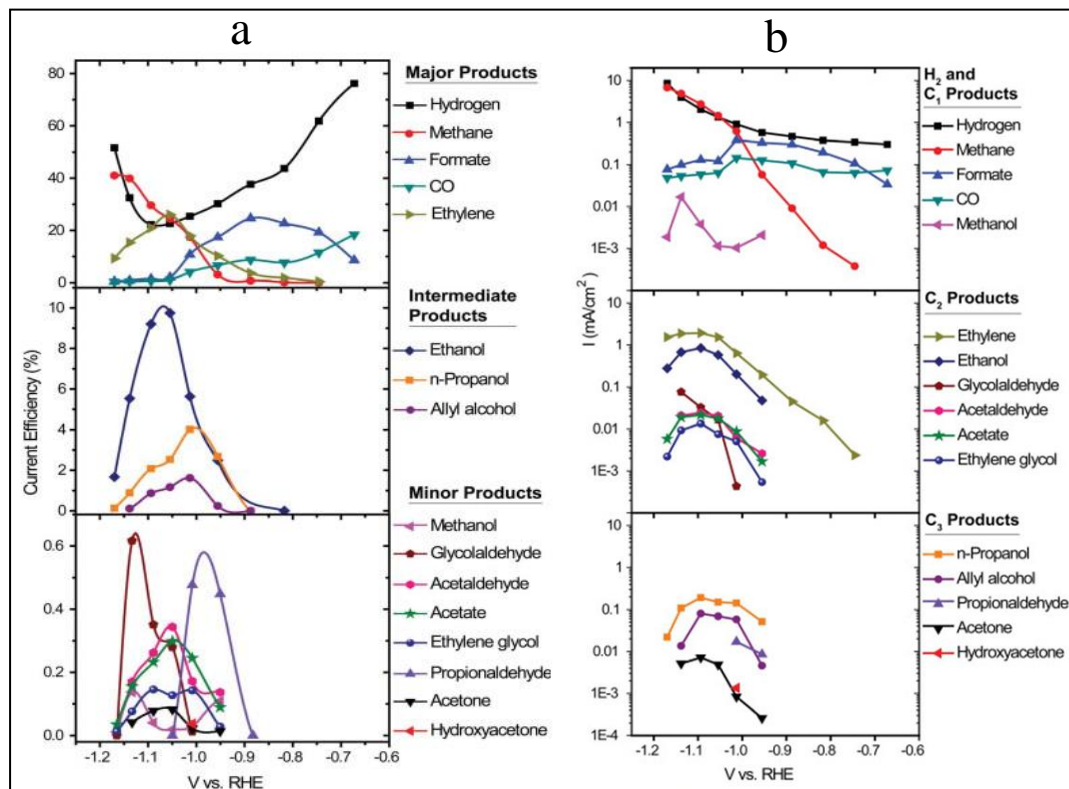
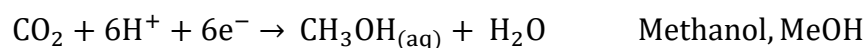


Figure 8 (a) the faradaic efficiency and (b) Tafel plot of the partial current going to each product produced by Cu catalyst [16].

### 2.3) Electrochemical reduction CO<sub>2</sub> to valuable chemicals (i.e., methanol)

To understand the production of some complex products of CO<sub>2</sub>RR process. Methanol was selected as a desirably valuable chemical product due to its wide range of applications, including direct use as a fuel for a fuel cell [36, 37]. Generally, methanol can be produced by many ways such as methanol formation from natural gas or synthesis by CO<sub>2</sub> and H<sub>2</sub>. In the present, Cu/ZnO/Al<sub>2</sub>O<sub>3</sub> is used as the catalytic electrode to produce methanol in the commercial level [38]. According to CO<sub>2</sub> reduction reaction (CO<sub>2</sub>RR), electrochemical process is an interesting method that can also be used to produce methanol [39-46]. However, there are some challenges of methanol production by this method. Methanol production require 6 electron transfer which is higher than of H<sub>2</sub>, CO, and formate production [16]. The equilibrium equation of methanol formation in CO<sub>2</sub>RR presents as follow,



Due to more electron transfer, it is a result of more complicated mechanism pathway of methanol production, including many intermediates. An example of methanol pathway of Yang and his coworkers is shown in Figure 9 [47].

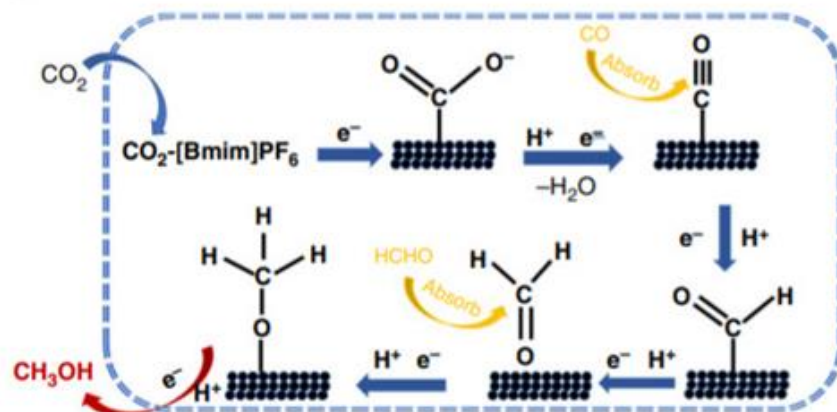


Figure 9 mechanism pathway of methanol in CO<sub>2</sub>RR [47].

A lot of studies have reported low current densities and/or low Faradaic efficiency [30, 40]. There are many factors that can affect both mentioned criteria. Electrode, electrolyte and other electrochemical factors such as temperature, pressure, and pH value can affect to methanol yield and rate of formation. Material which is used to be electrode is important to consider because different material electrodes provide different products. Copper is outstanding to look forward to studying for methanol production. Moreover, the development of copper electrode can improve both selectivity and activity of methanol yield. Methanol has been reported as a product of electrochemical reduction on a Cu<sub>2</sub>O surface [48-50]. However, for other materials, Ru and Mo were also used as an electrode producing methanol in 1900's [51, 52]. Other novel materials such as Pt@Adenine-rGO [39], Boron-doped diamond [43], Pulse-deposited Zn catalytic electrode on Ag foams (PD-Zn/Ag foam)[40] and MoS<sub>2</sub>-rods/TiO<sub>2</sub> nanotubes heterojunction electrodes were studied in previous works.

#### 2.4) Catalytic electrode development

However, studying the developing method of selectivity and activity enhancement of other products is necessary to obtain the direction of methanol formation development. CO and formate are two products that can provide selectivity as high as nearly 100 percent with acceptable reaction rate. Moreover, methane, ethylene, and ethanol yields have also been developed. These higher yields were caused by using more suitable catalytic electrode. Therefore, studying the catalytic property of these electrodes and relating to their product yield enhancement may pursue the understanding of product formation mechanism and effect of electrode development. According to the previous studies, there were Cu-based alloys studied by Hirunsit [53]. She used DFT method to estimate CO<sub>2</sub> reduction to CH<sub>4</sub> with Cu<sub>3</sub>Ag, Cu<sub>3</sub>Au (211) compared to Cu (211) in 2013. CuSn catalytic electrode is a non-noble metal which is not only low-cost material but also having selectivity of CO in the wide overvoltage ranges [35]. CO selectivity increase in as a function of

overvoltages. Moreover, oxide-derived copper or OD-Cu sample in this research provide CO, H<sub>2</sub> selectivity as a volcano trend while HCOOH is increasing in monotonic trend with increasing overvoltages. In additions, methanol is also found, but very small amount. There are some previous studies consider the catalytic selectivity of CuIn [54, 55]. This kind of catalytic electrode also produces CO; however, its stability is less than CuSn system. In case of CuPd [56], it is an effective catalytic electrode for CO formation from CO<sub>2</sub> with effective cost than Au catalytic electrode. CuPd also keeps geometric and electronic effect influenced by bimetallic synergistic effect.

Besides, there are other bimetallic catalytic electrodes studied in previous research. For example, in 2015, Pd-Pt system was also studied by Koper [57]. He reviewed the synthesis of Pd<sub>x</sub>Pt<sub>(100-x)</sub>/C nanoparticles producing formate as a major product. Although, CO may poison to the catalytic electrode, formic acid was generated with optimize ratio composition. To develop the catalytic electrode, this research varied the compositions to achieve formate formation at low overvoltage with high faradaic efficiency and stability. Pd<sub>70</sub>Pt<sub>30</sub>/C nanoparticles can provide reaching the maximum 90% FE of formate at overvoltage -0.4 V vs RHE in 1 hour. He also claimed that this catalytic electrode has enough high potential activity as the best formic formation from CO<sub>2</sub> catalytic electrode in the time.

## 2.5) Chemical composition development (kind of catalytic electrode)

Based on previous literatures, many researchers have provided a lot of effort to enhance selectivity and activity of methanol. Varied kinds of catalytic electrode have been developed. Some studies presented that Cu-based catalytic electrodes were practical for methanol formation depending on catalytic electrode preparation method, especially Cu-oxide catalytic electrode. Table 5 lists the previous studies using Cu-based electrode. This table shows the overpotential, faradaic efficiency, rate of reaction and lifetime of each electrode.

Copper oxide electrode is an interesting candidate. It can be fabricated by the simple method. Thermal oxidation and electrodeposition are two main methods which generally used to fabricate the copper oxide electrode. The chemical composition of copper oxide electrode is changed, so its catalytic performance will be differentiated from the metallic copper such as copper foil. Some previous studies showed that Cu-based electrode can be developed to the optimal catalytic electrode for methanol formation. Similarly, this also relate to the unique catalytic property of copper as mentioned previously in this section.

Table 5 Cu-based electrode for methanol formation in CO<sub>2</sub>RR.

Electrode	E (V vs. SCE)	FE (%)	Rate (E-6 mol.m <sup>-2</sup> .s <sup>-1</sup> )	Stability (hr)	Ref.
<b>Cu-based electrodes</b>					
Pre-oxidized Cu-TiO <sub>x</sub> (45 min., 500 °C)	-0.45	~30	33.3	-	Frese 1991
Cu <sub>2</sub> O carbon paper	-1.3 (Ag/AgCl)	45.7	60.8		Albo 2015
Cu <sub>2</sub> O/ZnO carbon paper	-1.3 (Ag/AgCl)	17.7	31.7	5	
Cu <sub>88</sub> Sn <sub>6</sub> Pb <sub>6</sub> alloy foil	-0.7	36.3	17.6 (44.47 μmol.h <sup>-1</sup> )	2	Schizodimou 2012
30% Cu <sub>2</sub> O-MWCNTs	-0.8 (Ag/AgCl)	38			Malik 2016
Electroplated Cu <sub>2</sub> O	-1.05 (Ag/AgCl)	38	119		Ren 2011
Anodized Cu foil	-1.35 (Ag/AgCl)	20	5.6		
Air-furnace oxidized Cu	-1.45 (Ag/AgCl)	2	0.3		
Cu on CNTs	-1.5	3.9			Rahman 2014
copper selenide nanocatalysts	285 mV	77.6			Han 2019

Methanol has been produced as a product of electrochemical reduction on a Cu-oxide surface. For a good example studied by Ren and his coworkers in 2011 [44], copper electrode were developed as electrodeposited, anodized and oxidized copper catalytic electrodes for using in their research. Methanol production rate of them is shown in Figure 10. The electrodeposited copper catalytic electrode provides the highest rate of methanol formation followed by anodized and oxidized copper, respectively. Moreover, FE of methanol which produced by the electrodeposited, anodized and oxidized copper catalytic electrodes were 38, 20, and 2 percent, respectively.

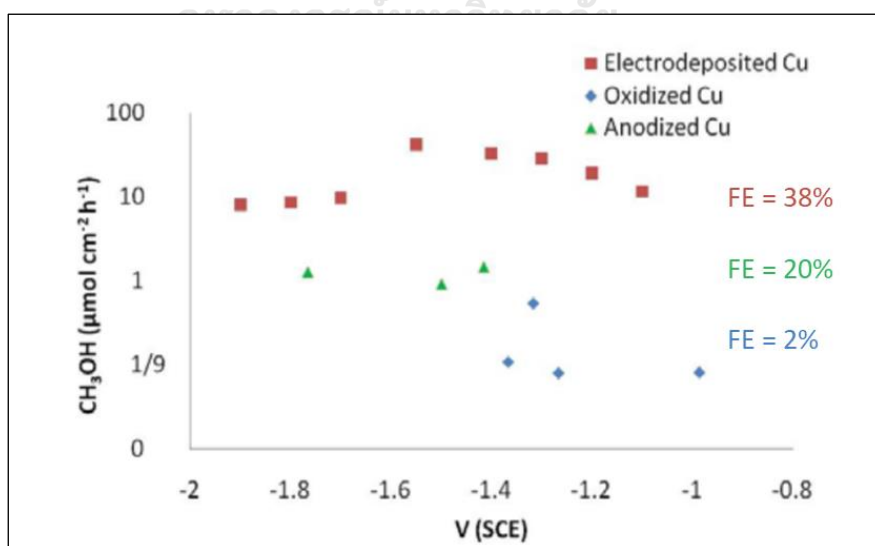


Figure 10 Methanol production rate of electrodeposited, oxidized, and anodized Cu catalysts.

Moreover, a work of Minh and his coworker showed that form of copper (i.e.  $\text{Cu}^0$ ,  $\text{Cu}^+$ ,  $\text{Cu}^{2+}$ ) also gave an impact on methanol formation. Cu-oxide surface provides much higher activity for hydrocarbons. Generally, copper is easily contaminated with organic compound due to its high affinity for absorbed  $\text{O}_2$ . Oxygen on Cu-oxide can increase number of defect electron and  $\text{CO}_2$  can be absorbed on the catalytic electrode surface. Cu-oxide reduction reactions and their standard electrode potential ( $E^0$ ) are presented in Table 6 [58].

Table 6 Cu-oxide reduction reactions and their standard electrode potential ( $E^0$ ) [59].

Equation no.	Cu-oxide reduction reaction	Standard electrode potential, $E^0$
1	$\text{Cu}_2\text{O} + 2\text{H}^+ + 2\text{e}^- \rightleftharpoons 2\text{Cu} + \text{H}_2\text{O}$	$E_o = 0.471 \text{ V vs. SHE}$
2	$\text{CuO} + 2\text{H}^+ + 2\text{e}^- \rightleftharpoons \text{Cu} + \text{H}_2\text{O}$	$E_o = 0.570 \text{ V vs. SHE}$
3	$2\text{CuO} + 2\text{H}^+ + 2\text{e}^- \rightleftharpoons \text{Cu}_2\text{O} + \text{H}_2\text{O}$	$E_o = 0.669 \text{ V vs. SHE}$

According  $E^0$  value of Cu-oxide in Table 6, the  $E^0$  value of Cu(II)oxide or CuO reduction to metallic Cu ( $\text{Cu}^0$ ) in equation 2 is more positive than of Cu(I)oxide or  $\text{Cu}_2\text{O}$  reduction to metallic Cu ( $\text{Cu}^0$ ) in equation 1. This means that Cu(II)oxide is more reactive to form  $\text{Cu}^0$  than Cu(I)oxide. Moreover, Cu(II)oxide can also be reduced to Cu(I)oxide at higher  $E^0$  value than both equation 1 and 2. It can imply that Cu(I) is a Cu form that has more stability than of Cu(II) of Cu-oxide. Therefore, it should be selected to develop further in methanol formation. Moreover, heat absorption of CO on  $\text{Cu}_2\text{O}$  is more than CO on metallic Cu,  $\text{Cu}_2\text{O}$  site is more favorable to the adsorption of CO than Cu-site. Therefore, the controlling Cu(I) is very important to selectivity of methanol. As a result, surface development actually affects catalytic performance.

On the other hands, other kinds of materials such as Mo-based,  $\text{TiO}_2$  and GaAs electrode also provided good range of selectivity and activity but these developed electrodes were not practical to be used as catalytic electrode due to their complicated preparation method (i.e. indigo, organically doped metal) as presented in Table 7. For example, Molybdenum (Mo) was studied in some research. It found that Mo can produce methanol, but it can also be corroded during  $\text{CO}_2\text{RR}$ . Some materials can provide methanol, but their sample fabrication was complicated.

Table 7 Other kinds of developed electrode for methanol formation in CO<sub>2</sub>RR.

Electrode	E (V vs. SCE)	FE (%)	Rate (E-6 mol.m <sup>-2</sup> .s <sup>-1</sup> )	Stability (hr)	Ref.
<b>Ru/Mo-based electrodes</b>					
Mo foil-Cu (KOH/HF pre-treated)	-0.80	84	-	-	Summers 1986
RuO <sub>2</sub> +TiO <sub>2</sub> (35/65)-Ti	-1.48	76	-	-	Bandi 1990
Mo foil on Cu wire	-0.80	55	-	-	Summers 1986
Mo	-0.68	46	-	-	Frese 1986
<b>Other transition metal: Fe, Ti and Hg</b>					
Everitt's salt (ES, K <sub>2</sub> Fe"[Fe"(CN) <sub>6</sub> ]) coated-Pt	-0.90	15.5	-	5	Ogura 1986
Indigo (C <sub>16</sub> H <sub>10</sub> N <sub>2</sub> O <sub>2</sub> )/ graphite-Pt	-0.70	70.2-37.2	0.69-0.42	2-9	Ogura 1987
Indigo/ graphite-Fe	-0.70	42.8	1.08	5	Ogura 1987
<b>Post-transition Ga- based electrodes</b>					
n-GaAs-crystal-(111)As	-1.20 to -1.40	100	-	-	Canfield 1983
<b>Pt metal group metal- based electrodes</b>					
Pt-Ru/C powder deposited-carbon paper	-0.45	75	~186	1	Shironita 2013
Pd-O-Sn interfaces in Pd/SnO <sub>2</sub> NSs	-	34	-	8	Zheng 2018
<b>Novel materials</b>					
Pt@Adenine-rGO	-0.3 (Ag/AgCl)	85	-	-	Alinajafi 2018
Pyrite-nickel sulfide nanocomposite	-0.6 (RHE)	64	-	-	Zhao 2017
Organically doped Pd	-0.6 (SCE)	35	-	-	Yang 2015
Boron-doped diamond	-1.3 (Ag/AgCl)	24.3	-	-	Jiwanti 2016
<b>Metal deposited on metal foam</b>					
Pulse-deposited Zn catalyst on Ag foams (PD-Zn/Ag foam)	-	10.5	-	-	Yeo 2018
Pulse-deposited Zn catalyst on Ag foams (PD-Zn/Ag foam)	-1.38 (RHE)	7.5 - 8.1	13.3 umole / hr. cm <sup>2</sup>	8	Yeo 2018
<b>TiO<sub>2</sub> electrodes</b>					
TiO <sub>2</sub> Nanotube	-0.56 (RHE)	85.8	-	2	Ping 2017
MoS <sub>2</sub> -rods/TiO <sub>2</sub> nanotubes heterojunction electrodes	-	42	-	6	Li 2014

In addition to kind of catalytic electrode or chemical composition development of metal-based catalytic electrode (i.e., copper oxide), structure of electrode can also affect catalytic performance. Therefore, structural study is necessary to enhance the methanol yield. Due to the limitation of catalytic electrode improvement for enhancing methanol yield, studying the catalytic electrode development method from other major products such as CO, formate, and other hydrocarbons can facilitate to be as a guideline for catalytic electrode development for methanol formation.

According to copper oxide fabrication by electrochemical oxidation [59], Copper is used as an anode part of the electrical circuit in the electrochemical process. After anodization process, the uniform anodic Cu-oxide will be formed on the metal surface as shown in Figure 11(b). Similarly, there are two oxides forms namely cuprous oxide (Cu<sub>2</sub>O) and cupric oxide (CuO) as well as their mixtures in various phases such as copper-rich oxide (Cu<sub>4</sub>O<sub>3</sub>) [60]. In this study, there are three Cu-oxide



electrodes are fabricated for both comparing with previous study and developing new Cu-oxide catalytic electrodes. The first electrode is fabricated following the selected paper to be as reference [44]. The second electrode is a Cu-oxide with the acceptable performance. And the last electrode is the second Cu-oxide with optimize electrochemical parameters (such as potential and concentration of electrolyte etc.) for being a developed Cu-oxide that can provide higher performance. Moreover, the most proper condition will be studied more by varying with time to obtain the direction of the effect of time to catalytic electrode development.

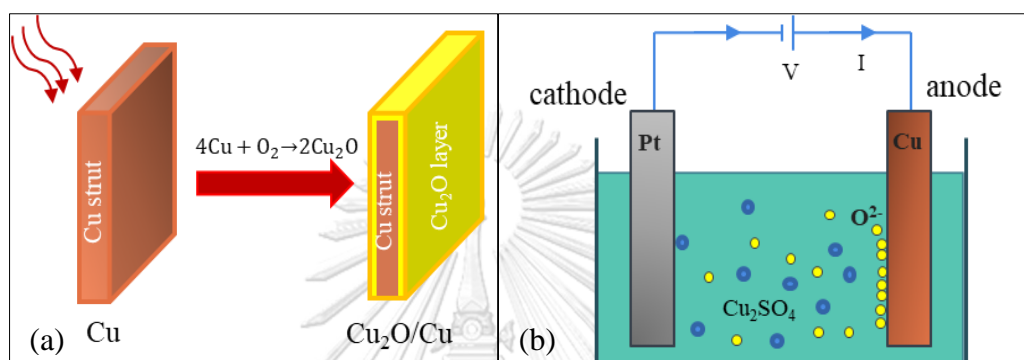


Figure 11 Oxide formation on Cu surface by (a) thermal oxidation (heating) and (b) electrochemical oxidation (anodization).

According to previous studies, copper oxide is generally formed by thermal oxidation of Cu [61-63]. The range of temperature which is used in thermal oxidation is 200-900°C. Castrejón and his coworkers presented that temperature below 400°C can caused a thin layer of Cu oxide [61]. For 400-700°C, the Cu oxide layer will be fragile but thermal oxidation at 800-900°C can improve the crystallization of  $\text{Cu}_2\text{O}$  and CuO. Moreover, CuO growth rate is less than of  $\text{Cu}_2\text{O}$  layer. Moreover, some research suggested that there are three Cu-oxide layer structures;  $\text{Cu}_2\text{O}$ , CuO and oxygen-rich Cu layer [64]. As mentioned, the occurrence of Cu oxide layer is depended on the processing parameter such as temperature and time of thermal oxidation.

## 2.6) Structural development

High efficiency, selectivity and cost-effective are required for being a suitable catalytic electrode. Plenty of previous studies making research and development with structure as an initial priority. Crystallographic orientation of metal used as catalytic electrode, more surface areas, and porosities of catalytic electrodes can provide more activity and selectivity of product formation form  $\text{CO}_2$  reduction. Furthermore, product selectivity is dependent on sizes, expose facets, compositions, and morphologies. Suitable structure can increase product selectivity because of the increasing active site on the catalytic electrode surface. Kim and Liu presented that Ag catalytic electrode structure improvement effect on CO selectivity [65]. Reske

showed on his report that hydrocarbon selectivity decrease with increasing size of Cu nanoparticles [66]. Structurally designed metal can be divided in 3 main characteristics: (1) Crystallographic texture (2) Nanoparticles and (3) Porous structure of metal which used as catalytic electrode. Both of Nano and Porous structure can increase over 3 order of magnitude higher activity than the of the bulk structure because of increasing in step site density [67]. Therefore, this study will focus on nano and porous structure as structural development.

### 2.6.1) Crystallographic Texture

Surface morphology is considered as an important factor impacting both activity and product selectivity of CO<sub>2</sub> reduction because they are strongly depended on surface structure [68]. In 1995, Hori initiated to study the effect of electrode texture to the product selectivity as presented in many papers. Products from the electrochemical reduction of CO<sub>2</sub> at Cu single crystal electrodes. He discovered that C<sub>2</sub>H<sub>4</sub> was preferably formed on the Cu (100) electrode more than CH<sub>4</sub>, and CH<sub>4</sub> is the main product on the Cu (111) surface as illustrated in Table 8 [69].

Table 8 Products from the electrochemical reduction of CO<sub>2</sub> at Cu single crystal electrodes [64].

Electrode	Potential (V) versus NHE	Current efficiency (%)						
		CH <sub>4</sub>	C <sub>2</sub> H <sub>4</sub>	CO	HCOO <sup>-</sup>	MeCHO	EtOH	H <sub>2</sub>
Polycrystal	-1.44	33.3	25.5	1.3	9.4	1.1	5.7	20.5
(100)	-1.42	25.0	31.7	0.0	5.1	1.9	9.8	23.3
(110)	-1.55	49.5	15.1	0.0	6.6	3.1	7.4	18.8
(111)	-1.56	38.9	4.7	0.0	4.8	0.0	0.9	56.5
								103.5
								96.9
								100.4
								105.7

Electrolyte solution: 0.1M KHCO<sub>3</sub>. Current density: 5.0 mA cm<sup>-2</sup>. Temperature: 18° C.

Table 9 Product distribution in the electrochemical reduction of CO<sub>2</sub> at a series of copper single crystal electrodes Cu(S)- [n (111) x (111)] and Cu(S)- [n (110) x (100)] [65].

Crystal orientation	<i>n</i>	Potential/V vs. SHE	Current efficiency/%														C <sub>2</sub> H <sub>4</sub> /CH <sub>4</sub>	
			CH <sub>4</sub>	C <sub>2</sub> H <sub>4</sub>	CO	H <sub>2</sub>	MeD	EtOH	PrD	AlOH	PrOH	HCOOH	CH <sub>3</sub> COOH	C <sub>2</sub> +	Gas total	Total		
<i>n</i> (111)-(111)																		
(111)	∞	−1.55	46.3	8.3	6.4	16.3	2.1	2.6	0.6	0.7	0.0	11.5	1.5	15.8	61.0	96.3	0.2	
(554)	10	−1.50	51.4	10.7	6.3	10.4	2.9	4.6	0.5	0.4	0.2	10.3	1.9	21.2	68.4	99.6	0.2	
(332)	6	−1.51	39.6	9.9	6.1	10.3	5.1	7.1	0.2	0.3	0.2	9.4	3.4	26.2	55.6	91.6	0.3	
(221)	4	−1.54	17.5	16.1	9.6	7.3	6.4	13.1	1.0	0.0	0.1	10.8	6.3	43.0	43.2	88.2	0.9	
(331)	3	−1.55	13.8	16.6	7.7	5.7	7.1	15.6	0.5	0.0	0.4	9.1	7.5	47.7	38.1	84.0	1.2	
(110)	2	−1.58	6.9	13.5	13.9	3.1	19.9	10.5	1.3	tr	0.04	10.1	20.8	66.0	34.3	99.9	2.0	
(110)	2	−1.58	8.4	15.1	11.7	3.4	25.3	10.8	0.9	0.0	0.0	10.5	17.8	69.9	35.2	103.9	1.8	
<i>n</i> (110)-(100)																		
(650)	6	−1.59	10.5	16.2	14.5	2.5	16.2	10.9	0.8	tr	0.06	6.1	20.6	64.8	41.2	98.4	1.5	
(540)	5	−1.60	16.1	15.2	12.9	3.3	9.2	8.8	1.4	0.0	0.1	6.9	13.5	48.2	44.2	87.4	0.9	
(430)	4	−1.56	25.2	15.0	12.9	3.5	7.4	8.1	1.5	0.3	0.4	9.7	8.6	41.3	53.1	92.6	0.6	
(320)	3	−1.52	52.4	13.7	5.4	5.3	3.2	6.5	0.6	0.3	0.4	5.8	4.8	29.5	71.5	98.4	0.3	
(210)	2	−1.52	64.0	13.4	2.2	7.0	0.9	6.6	0.6	0.2	0.5	5.5	0.7	22.9	79.6	101.6	0.2	

Electrolyte solution: 0.1 M KHCO<sub>3</sub>. Current density: 5 mA cm<sup>-2</sup>. MeD: Acetaldehyde, EtOH: Ethanol, PrD: Propionaldehyde, AlOH: Allyl alcohol, PrOH: Propanol. C<sub>2</sub>+ contains all the substances, which have more than two carbon atoms. The gas total contains all the gaseous products other than H<sub>2</sub>. tr: less than 0.05%.

Moreover, Table 9 shows the effect of crystal orientation (due to different number of dangling bonds in each texture) on product distribution in the electrochemical reduction of CO<sub>2</sub> at a series of copper single crystal electrodes Cu(S)-[n (111) x (111)] and Cu(S)-[n (110) x (100)] [70].



There are many methods to develop the surface structure such as PVD which is used in the research group of Jaramillo's laboratories. PVD can be used to form the large-format electrodes with analogous electrocatalytic properties to single crystals [68]. Relationships between structure and activity are proved that it can enhance the activity and selectivity of electrocatalytic electrode. In 2016, Broekmann studied CO<sub>2</sub> reduction on single-crystalline Cu catalytic electrodes [71]. C<sub>2</sub> products (C<sub>2</sub>H<sub>4</sub>, C<sub>2</sub>H<sub>6</sub>) can be predominantly formed on Cu (100) surface texture while C<sub>1</sub> product (CO and CH<sub>4</sub>) preferred to be generated as a hydrocarbon reaction product on Cu (111) surface inside of mesoporous with his superior selectivity foam catalytic electrode. These results were consistent with the previously mentioned Hori's work in 1995 [69]. Moreover, the formation of abundant of grain boundary with a lot of active sites including the preferable facets such as (100) and (111) caused the higher activity and increasing the product selectivity [72]. This can lead to reconstruct of surface facets. Additional experiment is a work of Kanan that shown in Figure 12 [73], which consisted of (A) bulk electrolysis with two-compartment H-cell and (B) scanning electrochemical cell microscopy (SECCM) used to test the local electrocatalytic activity across GBs. The result confirmed that catalytic activity was depended on the facets, but there was no correlation with the evolution activity of hydrogen.

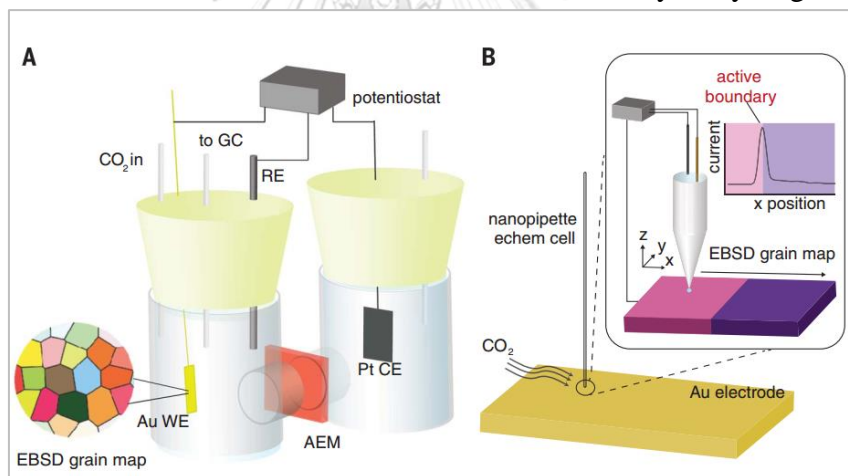


Figure 12 Two approaches for electrochemical characterization of defect effects on CO<sub>2</sub> reduction. (A) Bulk electrolysis of a well-defined polycrystalline Au electrode within a glass, two-compartment H cell. (B) SECCM using a ~300-nm nanopipette electrochemical cell [68]

According to Pussana's work in 2017, Table 10 [24] shows the onset potentials (V vs RHE) and corresponding partial current densities for various CO<sub>2</sub>RR products on Cu<sub>2</sub>O-derived Cu was compared to the Cu single-crystal electrodes consisting of Cu (100), Cu (111), and Cu (110) in CO<sub>2</sub> saturated 0.1 M KHCO<sub>3</sub> electrolyte. This research reported two general trends on Cu<sub>2</sub>O-derived Cu and Cu single-crystal surfaces. The first trend is the onset potential for C<sub>2</sub>H<sub>4</sub> formation always starts at 300-400 mV more negative than the onset potential for CO evolution. The second trend is C<sub>2</sub>H<sub>4</sub> was formed only after a significant amount of CO gas was

produced. It can be concluded that a high surface coverage of CO\* is essential for the selective formation of C<sub>2</sub>H<sub>4</sub> of Cu-based systems. Moreover, Noskov's work in 2012 [74] also showed that facets affected to the product selectivity including the complicated reaction mechanism.

Table 10 Onset Potentials (V vs RHE) and corresponding partial current densities for various CO<sub>2</sub>RR Products on Cu<sub>2</sub>O-derived Cu was compared to the Cu single-crystal electrodes consisting of Cu (100), Cu (111), and Cu (110) in CO<sub>2</sub> in the saturated 0.1 M KHCO<sub>3</sub> electrolyte [24].

catalyst	CO	C <sub>2</sub> H <sub>4</sub>	HCOO <sup>-</sup>	CH <sub>4</sub>
Cu <sub>2</sub> O-derived Cu	-0.28 V -1.3 $\mu\text{A}/\text{cm}^2$	-0.63 V -13 $\mu\text{A}/\text{cm}^2$	-0.48 V -27 $\mu\text{A}/\text{cm}^2$	-0.88 V -26 $\mu\text{A}/\text{cm}^2$
Cu(100)	-0.30 V -0.8 $\mu\text{A}/\text{cm}^2$	-0.70 V -13 $\mu\text{A}/\text{cm}^2$	-0.70 V -34 $\mu\text{A}/\text{cm}^2$	-0.85 V -19 $\mu\text{A}/\text{cm}^2$
Cu(111)	-0.60 V -0.9 $\mu\text{A}/\text{cm}^2$	-0.90 V -6 $\mu\text{A}/\text{cm}^2$	-0.65 V -26 $\mu\text{A}/\text{cm}^2$	-0.90 V -3 $\mu\text{A}/\text{cm}^2$
Cu(110)	-0.50 V -1.4 $\mu\text{A}/\text{cm}^2$	-0.80 V -4 $\mu\text{A}/\text{cm}^2$	-0.60 V -39 $\mu\text{A}/\text{cm}^2$	-0.90 V -13 $\mu\text{A}/\text{cm}^2$

### 2.6.2) Nanoparticles (nano)

Nanoparticle method strongly increases the large electrochemical surface area of material compared with polycrystalline catalytic electrode. It can lead to provide the higher activity catalytic electrode because of the greater stabilization of intermediates. As a result, CO<sub>2</sub> conversion will require less overpotential to overcome the thermodynamic barrier. An example of schematic diagram of a nanostructure characteristic as presented in Figure 13 [75]. There are varied types of nanostructures (i.e., nanotubes, nanoparticles, nanowires, and nanoneedles etc.) which used to develop the catalytic electrode of CO<sub>2</sub> reduction.

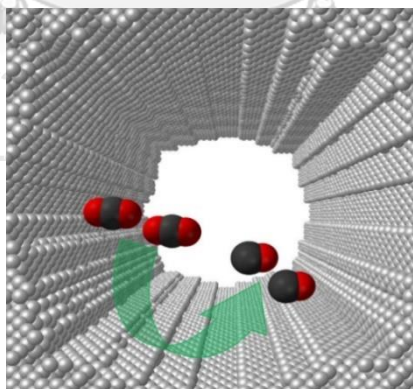


Figure 13 A schematic diagram of a nanostructure characteristic [70].

There are a lot of researches studied about the effect of nanomaterial based on Cu metal [76]. For example, Noskov presented the effect of nanostructure by comparing the product selectivity among electropolished surface, nanoparticle-covered surface, and sputtered surface with Cu electrode in 2002. The nanoparticle-covered surface catalytic electrode is predominant in C<sub>2</sub>H<sub>4</sub> and CO as shown in Figure

14 [74]. CO<sub>2</sub> conversion rate per unit area is approximately 10 times higher on Ag nanoparticles than the single crystal catalytic electrode in Amin and his coworkers' study [77]. Rosen also studied the effect of nanostructure Ag catalytic electrode which both of experiment and computation methods [67]. This pointed that nanostructure Ag catalytic electrode provided CO selectivity as high as 92%FE. Au nanoparticle also effect to the productivity of CO [33].

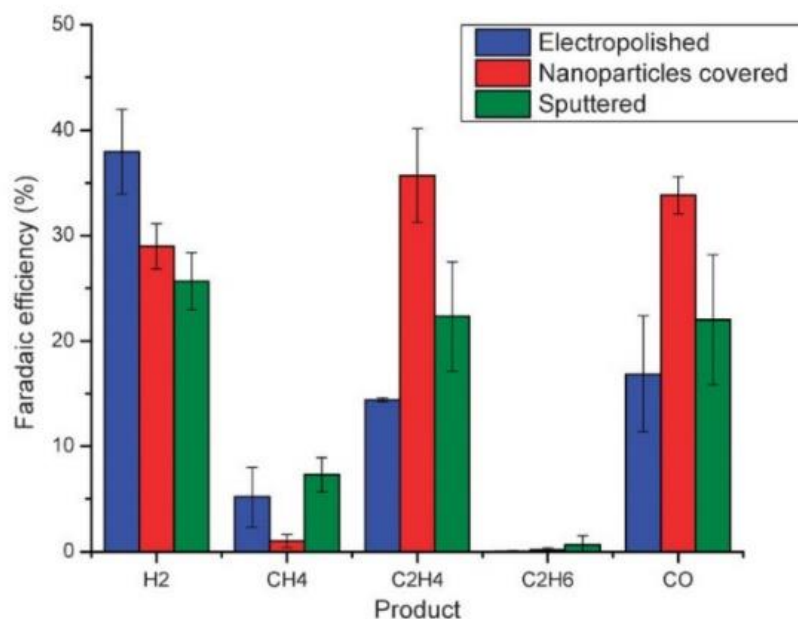


Figure 14 Faradaic efficiency for the products of electroreduction of CO<sub>2</sub> on three surfaces in CO<sub>2</sub>-saturated 0.1 M KClO<sub>4</sub> upon -1.1 V vs. RHE, including Sample A (electropolished surface), Sample B (copper nanoparticle-covered surface) and Sample C (sputtered surface) [69].

However, product selectivity is also depended on the different kinds of nanomaterials. For example, Nanowires and nanoneedles structure may give the different main product. This was supported by Xie's work in 2015, he discovered that C<sub>2</sub>H<sub>4</sub> was a favorable product of nanowires structure while CH<sub>4</sub> was produced more than C<sub>2</sub>H<sub>4</sub> of nanoneedles structure of Cu electrode as shown in Figure 16 [17]. The highest %FE of C<sub>2</sub>H<sub>4</sub> which caused by NWs is at -1.3 V, on the other hand, the highest %FE of CH<sub>4</sub> which generated by NNs is at -1.2 V. At these overpotentials, %FE of hydrogen keeps in the low range because of the product competition. SEM images of nanowires and nanoneedles Cu-oxide electrodes are presented in Figure 15.

According to many reviews, not only monolithic but also bimetallic catalytic electrode have been improved into nanoscale technique such as nanoparticle as well as nanotube approximately 2012-present. Some research focused on the electron efficiency, rate of product generation and product distribution of bimetallic catalytic electrode. Steven and his coworkers claimed that their AuCu nanotube catalytic electrode is as a state-of-the-art material in that time (2016) [78].

Researchers supported that the nanoparticle (NPs) can overcome the drawbacks of single-component materials [79]. Moreover, different kinds of catalytic electrode support of Au nanoparticle effect to the selectivity of CO selectivity [80].

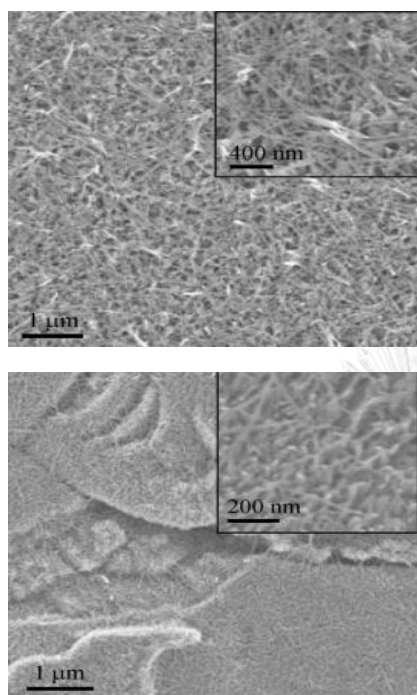


Figure 15 SEM image of the Cu oxide nanomaterials. (a) belonged to Cu oxide NWs (b) belonged to Cu oxide NNs [17].

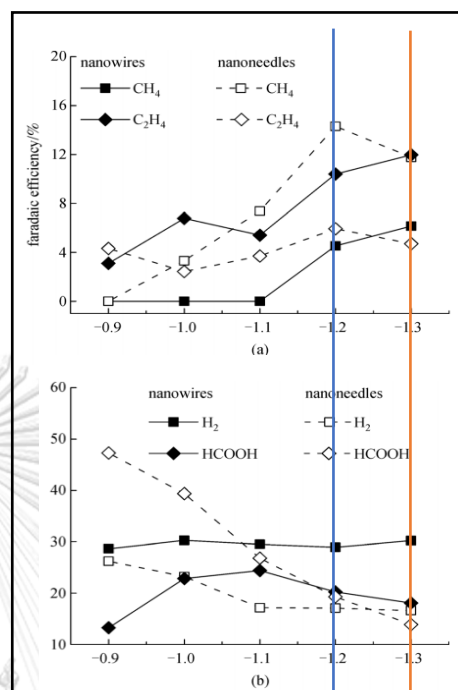


Figure 16 Comparison of the CO<sub>2</sub> reduction activities on Cu NWs and NNs in the solution of 0.1 molL<sup>-1</sup> KHCO<sub>3</sub> at 10°C. (a) FEs for CH<sub>4</sub> and C<sub>2</sub>H<sub>4</sub>, (b) FEs for H<sub>2</sub> and HCOOH [17].

### 2.6.3) Porous Structure

Mesoporous structure or 3D open-porous catalytic electrode structure has widely been studied for improving the catalytic activity and selectivity because of high gas permeability, good mechanical strength, and low density. In additions, CO<sub>2</sub>RR can provide higher current density at low overpotential by using improved 3D structure catalytic electrode as an electrode compared to smooth electrode [72]. Porous foam or honeycomb-like structure can be formed by fast electrodeposition with hydrogen bubbles including control the deposition parameters such as deposition temperature, pH value, and current density. High current density provide the smaller average grain size and lattice constant but high deposition temperature promotes to get the higher grain size than the lower one as shown in Figure 17 [81]. These mentioned electrodeposition factors can affect to the morphology and microstructures (dendrite branch size and grain size) of catalytic electrode. That can also affect to the physical property of catalytic electrode.

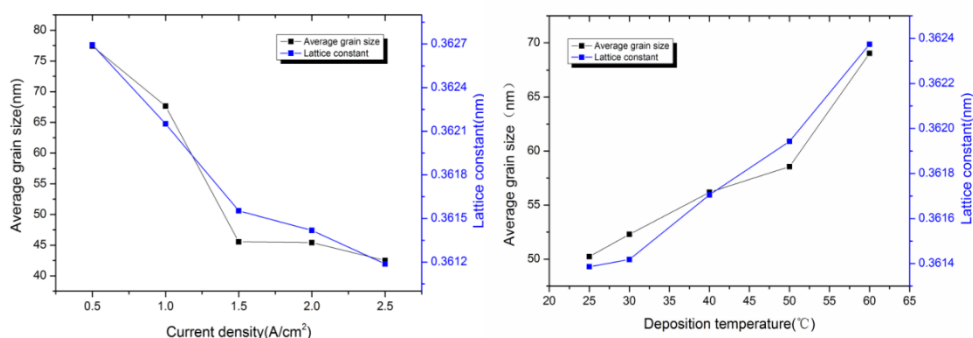


Figure 17 The effect of electrodeposition factors; (a) current density (b) deposition temperature on the average grain size [76].

Porous structure can increase gas dynamics diffusion as a result of increasing  $\text{CO}_2$  concentration at the catalytic electrode because of more active sites. A lot of research has shown that high porosity, large surface area per unit volume structure can enhance the electrocatalytic activity and product selectivity [56, 71, 82, 83]. Monolithic foam (one type of metal i.e., Cu) and bimetallic foam (two types of metal i.e., Cu/Pd) are attractively used as catalytic electrode due to their high porosity and low-cost material. Uniform porous is not suitable for  $\text{CO}_2$  conversion because the small porous near the top may limit the transport of the elective ions. Pore size and wall structure of catalytic electrode can be controlled by deposition conditions. In 2017, there were two interesting papers explained about the 3D-porous metal foam electrode. Nam studied the role of morphology based on the three different size (width/depth) of Cu porous foams, 300 nm/40 nm, 30 nm/40 nm and 30 nm/70 nm electrodes as illustrated in Figure 18 [31]. The result showed that  $\text{C}_2\text{H}_4$  preferred to be generated by 30 nm/40 nm electrode while  $\text{C}_2\text{H}_6$  was generated with the increasing pore depth as the 30 nm/70 nm electrode. 300 nm/40 nm electrode provided more %FE of hydrogen than the two electrodes.

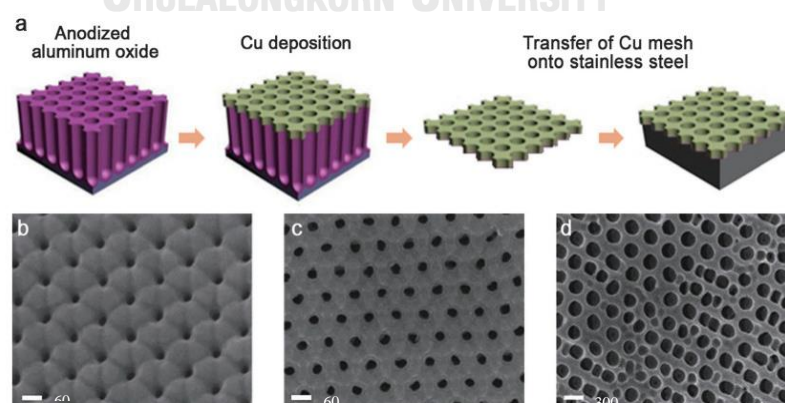


Figure 18 (a) Scheme for preparing of Cu mesoporous electrodes synthesis and SEM images of Cu electrodes mesopores with (b) 30 nm width/40 nm depth (30 nm/40 nm), (c) 30 nm width/70 nm depth (30 nm/70 nm), and (d) 300 nm width/40 nm depth (300 nm/40 nm) [31].



Rose compared the %FE of CO of Ag foam by varying the deposition durations for 30, 60 and 90 seconds to the Ag foil [84]. In this case, 60 seconds was the best deposition duration reflected by the increase %FE of CO and current density. Less deposition time caused the pore on the surface of electrode is small compared to Ag foam at 60 s. on the other hand, the vigorous hydrogen bubble comprising induced non-homogeneous due to too much deposition time.

Moreover, there is another interesting work of Brown university, Sen and his coworker developed the Cu electrode by nanoparticle and porous structure method as a hierarchical structure catalytic electrode in order to enhance the FE of hydrocarbons (i.e., methane, ethylene, propene). This research selected electrodeposition method for fabricating the electrodeposited copper with varying deposition time for (a) 5s; (b) 10s; (c) 15s; (d) 30s; and (e) 60s, moreover, (f) nanostructure of the electrodeposited foams as presented in Figure 19 [32].

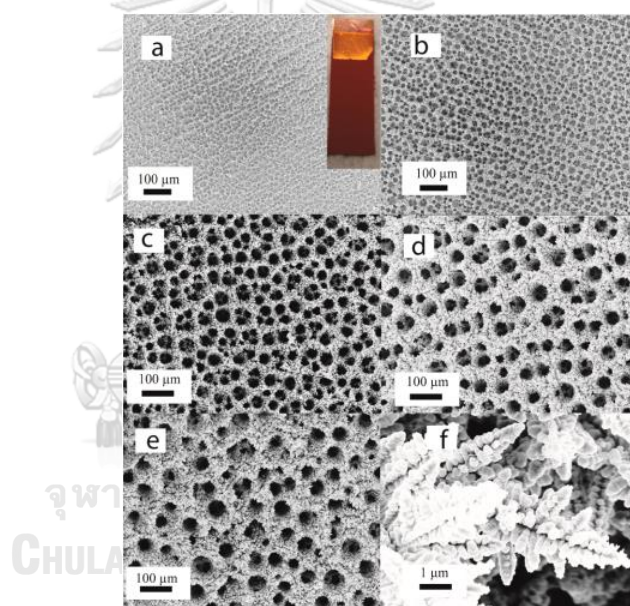


Figure 19 Electrodeposited copper form with varied deposition time for (a) 5s; (b) 10s; (c) 15s; (d) 30s; and (e) 60s, moreover, (f) nanostructure of the electrodeposited foams [32].

Figure 20 [32] illustrates the current density of smooth Cu and Cu foam electrode at different electrolyte concentration range. This result reported that copper foam provided higher current density than smooth copper. Especially, trend of current density at higher electrolyte concentration is clearer than at lower concentration. This could imply that their catalytic activity is increasing due to porous structure. Moreover, FE result also showed that selectivity of CO, formate, and hydrocarbons could be improved because of higher mass and charge transportation. This kind of catalytic electrode is promising for scaling CO<sub>2</sub> reduction up with the reasonable cost.

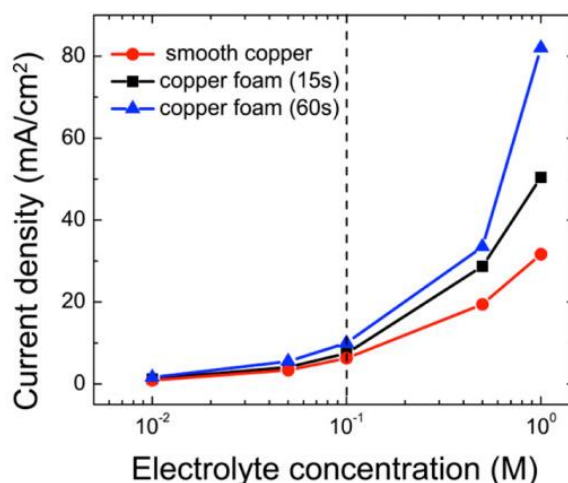


Figure 20 Current density of smooth copper (red line) and copper foam (black and blue lines) plotted as a function of electrolyte concentration, where the electrolyte was  $\text{KHCO}_3$  saturated with  $\text{CO}_2$  and the step potential was  $-1.8\text{ V}$  [32].

In addition to experimental results, it has also theoretically confirmed by DFT calculations that active sites play the important role in  $\text{CO}_2$  reduction process of Pd-Cu [56], Cu, Cu-Ag, and Cu-Au [53]. Both of Nano and Porous structure can increase over 3 order of magnitude higher activity than the of the bulk structure because of increasing in step site density [67]. Therefore, this study will focus on nano and porous structure as structural development.

Some researchers supported that surface area and fluid permeability are two key properties of porous metals [85]. Fabricated hierarchical porous copper consists of micro-pores (200-450  $\mu\text{m}$ ) and nano-pores (200-600 nm). Shin suggested that lowering hydrophobic force of hydrogen generation can reduce the pore size as well as increase of porosity [83]. If hydrophobic force is more than hydrodynamic force, hydrogen bubbles will coalesce together getting a larger hole. Additives such as acetic acid ( $< 0.1\text{M}$ ) can be used as bubble-stabilizer because it is no metallic ion. Polyethylene glycol: PEG ( $< 0.36\text{ g/L}$ ) can also be used to reduce pore size [86]. Moreover, branch size in the foam can be reduced by addition of chloride ion. For instance, 1-50 mM HCl can reduce branch size from 300 nm to 50 nm [83]. Increase in copper salt can enhance the copper deposition rate but not significant for pore size and wall density of foam structure. Chloride ion can eliminate the stress and reduce the particles of the process. Deposition reaction can be accelerated by adding chloride ion causing more copper film with highly open porous nanostructured wall due to ramification and catalytic effect of chloride ion.

#### 2.6.4) Pulse electrodeposition of porous fabrication

Pulse electrodeposition is another method to produce the denser porous copper compared to direct current deposition. Three main factors are (1) pulse current, (2) pulse on time, and (3) pulse off time. Different pore size, porosity, including hardness of porous structure depend on pulse frequency, duty cycle, applied current

density or overpotential [86, 87]. For example, increase of hydrogen evolution due to higher current density cause getting higher surface area of electrode but lower adhesion and compactness. This issue can be treated by addition of additives. Effect of pulse on time can be considered by the pause to pulse ratio. Increasing pause to pulse ratio cause decrease of hydrogen evolution, increasing copper deposition providing a dish-like holes structure. On the other hand, longer deposition pulse providing more saturated solution cause the larger formation of hydrogen bubbles. Longer pulse off time causes the lower hardness due to grain growth or recrystallization. Moreover, increase of electrolysis time cause coalescence of hydrogen bubbles providing larger pore size. Pulse electrodeposition can save energy, increase specific surface area, and improve the deposit structural stability. Nikolic [87] suggested the relationship of pulse ratio and structure of porous copper that the honeycomb-like structure was formed by electrodeposited at the constant current density. There is non-coalescence hole (individual hole formed by attached hydrogen bubbles), coalescence hole (coalescence of closely formed hydrogen bubble), and cauliflower-like agglomerates (very disperse and consisted of small agglomerates of copper grains) in the pulse electrodeposited porous structure. The longer deposition pulse cause solution become more saturated, and the larger number of hydrogen bubbles formation. On the other hand, the shorter deposition pulses, the small number of hydrogen bubbles is formed at the electrode surface as in the initial stage of electrodeposition process. The shape, size and number of holes strongly depended on the length of pulse on time. With high pulse on time, the structure consists of both coalescence and non-coalescence holes. With lower pulse on time, the structure tends to have only non-coalescence holes, dish-like holes, and constructing the honeycomb-like structure as shown in Figure 21.

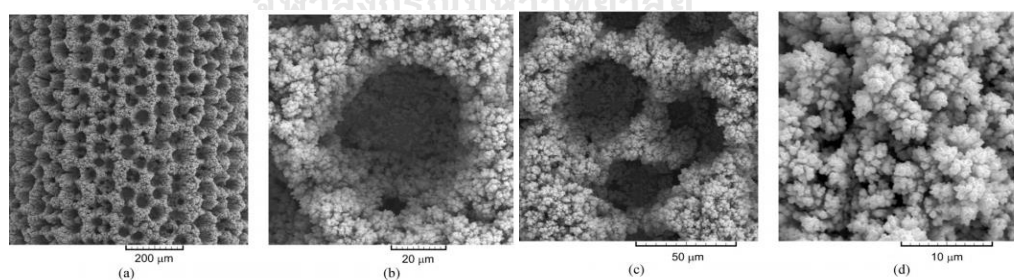


Figure 21 Structure of pulse electrodeposited porous copper: (a) Honeycomb-like structure, (b) Non coalescence hole, (c) Coalescence hole, and (d) Cauliflower-like agglomerates [87].

There are three main advantages of pulse electrodeposition compared to the direct current electrodeposition consisting of (1) reduction of porosity (reduction of surface roughness), (2) fine-grained deposits, and (3) low electrical resistance.



### 3. Scope of experiments

Copper was selected as a main metal-based catalyst in this work because copper has the intermediate binding energy between  $\ast\text{CO}$  intermediate and the surface. The  $\ast\text{CO}$  intermediate can be absorbed and further reduced to product which requiring more than 2 electron transfer for formation. Copper-based catalyst can provide higher product distribution than of other metals, but products are formed with low activity and faradaic efficiency. Therefore, it is an interesting challenge to develop it to get the better catalyst from copper metal. The goal of catalytic electrode fabrication in this work is to study the relationship between processing parameters in fabrication process for enhancing the catalytic property of copper-based catalytic electrode in order to maximize the yield of valuable chemicals by increasing selectivity and activity with minimal energy input. At the present, faradaic efficiency of CO and formate are as high as approximately 100% by using Au and Sn as catalytic electrode, respectively. On the other hand, copper is under investigated for valuable chemicals formation due to its moderate binding energy with CO intermediate. Moreover, among metal which are used as catalytic electrode in  $\text{CO}_2\text{RR}$ , copper is the only metal that can provide hydrocarbons but not for acceptable valuable chemicals yield. Copper oxide is an interesting candidate for valuable chemicals formation due to more performance of copper oxide surface. Moreover, Cu (I) tend to have more potential than Cu(II) and  $\text{Cu}^0$  as suggested by previous studies.

Challenges of this study are (1) how to stabilize  $\text{CO}^\ast$  intermediate during  $\text{CO}_2\text{RR}$  and (2) how to increase selectivity and activity of valuable chemicals formation. Since  $\text{CO}^\ast$  intermediate plays an important role affecting to product distribution. From these challenges, there are some possible solutions consisting of changing chemical composition or structure of copper catalytic electrode, selecting the suitable form of copper, and stabilizing it and developing the physical form of copper catalytic electrode by the proper preparation method.

The studies are divided into 3 Sections that focus on different electrodes' fabrication and surface modification processes, as follows:

#### 3.1) Sample fabrication

##### **Section1: Electrodeposited porous copper electrocatalysts**

Since, increase of catalytic electrode surface area may be the possible solutions. Previous studies tend to enhance the reaction rate by increasing surface area of catalyst. Moreover, electrolyte concentration can affect to the porous structure of catalytic electrode while applied current, deposition time, deposition method also affects to pore size and pore characteristic.

##### 1.1) Constant-current electrodeposition

Differentiation of copper metal deposition and porous copper fabrication is that higher concentration of  $\text{H}_2\text{SO}_4$  and higher current density was used to fabricate

porous copper. High amount of  $\text{H}_2\text{SO}_4$  enhance the hydrogen bubbles generation rate while high current density provides high energy for deposition.

This work focus on the effect of electrodeposition parameters consisting of deposition time, current density, and bath composition influencing on porous fabrication performance. The  $\text{CuSO}_4$  and  $\text{H}_2\text{SO}_4$  concentrations of bath composition, current density (2, 3, and  $3.5 \text{ A/cm}^2$ ) and deposition time (20, 40, and 60 s) were assorted to study the pore characteristics, morphology, and their electrocatalyst performance for  $\text{CO}_2\text{RR}$ . All constant-current porous coppers were fabricated at Metallurgy and Materials Science Research Institute (MMRI), Chulalongkorn University. The porous B-3-40 was fabricated for  $\text{CO}_2\text{RR}$  experiment at 2 laboratories: (1) Chemical Engineering, Chulalongkorn University and (2) Nanotec, NSTDA to compare the setup and the obtained result, moreover, to alternative study about the electrochemical property of the fabricated porous B-3-40. The surface area of copper foil substrate was different size because of the limitation of reactor type. The surface area of copper foil substrate which used as electrocatalyst in H-cell at Chemical Engineering, Chulalongkorn University was  $2.5 \times 2.5 \text{ cm}^2$  whereas the surface area of copper foil substrate which used as electrocatalyst in Flat-cell at Nanotec, NSTDA was  $4.2 \times 2.2 \text{ cm}^2$ .

### 1.2) Pulse electrodeposition

Pulse electrodeposition was performed at Fraunhofer Institute for Manufacturing Engineering and Automation (Fraunhofer-Institut für Produktionstechnik und Automatisierung: IPA), Stuttgart, Germany. For this work, the pulsed electrodeposited porous coppers were fabricated to compare their porous structure with constant current electrodeposition for being a guideline of next studies. The four groups of pulse electrodeposited porous copper (PX-10) namely P1-10, P4-10, P10-10 and P20-10 which fabricated by varying the pulse on time at 1, 4, 10, and 20 milliseconds, respectively. The pause off time, current density, and deposition time were fixed at 10 milliseconds,  $0.44 \text{ A/cm}^2$ , and 40 seconds, respectively.

## Section 2: Thermally-oxidized copper electrocatalysts

Based on previous studies [61], the fabrication of copper can produce valuable chemicals with higher selectivity than copper electrode. Copper oxide fabrication is an interesting way (i.e., thermal oxidation and electrochemical oxidation). It is a simple, cheap process that can provide copper oxide electrode. In this study, soaking temperature is the variables of focus. Four temperatures consisting of 300, 500, 800, and  $1000^\circ\text{C}$  were selected to represent the temperature range: low (less than  $400^\circ\text{C}$ ), moderate ( $400\text{--}700^\circ\text{C}$ ), and high (more than  $700^\circ\text{C}$ ), respectively with fixed oxidation time for 1 hour to study the effect of physical and chemical properties on catalytic activity of copper catalytic electrodes. Such designed heat treatment protocols were

applied onto high purity copper foil substrates. Oxidized copper electrodes namely A300, A500, A800, and A1000 were fabricated by thermal oxidation in the furnace at Metallurgy and Materials Science Research Institute (MMRI), Chulalongkorn University.

### **Section 3: Copper oxide electrocatalysts thermally-induced from electrodeposited porous copper**

The developed electrodes in this section were the combination of the representative conditions of surface development in section 1 (A-3-40, B-3-40, and C-3-40) and chemical development in section 2 (A300). This section focuses on studying the feasibility of the fabricated catalyst.

#### **3.2) Sample Characterization and Analysis**

The 2D-characteristics were demonstrated by 2D-morphology, apparent pore size, and percentage of apparent porosity whereas the 3D-characteristics were manifested by 3D-morphology, true surface area, pore distribution, and surface roughness. Moreover, their chemical composition, including bulk composition and surface composition were also analyzed. The 2D-surface morphology was observed by the optical microscope (OM). Image J software was used for analyzing the apparent pore size and apparent porosity. For in depth characteristics, the 3D-morphology was also utilized by the scanning electron microscope (SEM). Brunauer-Emmett-Teller (BET) and Barrett-Joyner-Halenda (BJH) were manipulated for acquiring the true surface area and pore distribution. Moreover, surface roughness was also measured by the 3D-profilier. In addition to the physical property, the bulk and the surface composition were detected by energy dispersive X-Ray (EDX) and X-ray photoelectron spectroscopy (XPS), respectively. All analysis method were tabulated in Table 11.

Surface morphology and chemical composition were needed for all samples. Copper and oxygen content affect the catalytic electrode property. The chemical composition change of bulk and surface could be confirmed. On the other hand, pore characteristic investigation was required for only porous copper (section 1) and the thermally-induced copper oxides from porous copper (section 3).

Table 11 Sample analysis

Sample analysis	Objective	Technique	Analysis	Consequence
Physical property	2D-surface morphology	Optical microscope (OM)	Image with 500X magnification	2D-Morphology
	2D-pore characteristics	Image J software	Pore diameter and percentage of porosity measurement	Apparent pore size and apparent porosity
	3D-surface morphology	Scanning Electron Microscope (SEM)	Image with 2000X, 5000X, 15,000X magnifications	3D-Morphology
	3D-pore characteristics	Brunauer-Emmett-Teller (BET)	Isotherm plot of adsorption and resorption, and BET surface area	True surface area
		Barrett-Joyner-Halenda (BJH)	The correlation between $dV/d\log(W)$ Pore Volume ( $\text{cm}^3/\text{g}$ ) and Pore Width (nm)	Pore distribution
		3D-profilier	Value of Ra, Rz	Surface roughness
Chemical property	Chemical composition	Energy dispersive X-Ray (EDX)	Atomic of %Cu, %O, and %C	Bulk composition
		X-ray photoelectron spectroscopy (XPS) with CASA software	Oxidation state of Cu ( $\text{Cu}^0$ , $\text{Cu}^+$ , and $\text{Cu}^{2+}$ ) with CASA software analysis	Surface composition

### 3.3) CO<sub>2</sub>RR Testing and Chemical Product Detection

After the sample fabrication, all samples were employed as the electrocatalyst in CO<sub>2</sub>RR process for investigating their performance. The CO<sub>2</sub>RR experiment is tested by two type of reactors (conventional H-cell and Flat cell). Sandwich (flat) cell is a type of H-cell with shorter distance between working electrode and counter electrode. Both type of reactors are composing of 3 electrodes: working electrode (WE), counter electrode (CE), and reference electrode (RE). The conventional H-cell

is made of glass but the flat cell is made of the teflon. The distance between WE and CE of H-cell is approximately 6 cm but for flat cell is approximately 2 cm.

The CO<sub>2</sub>RR was run in the H-cell electrolyzer with three electrodes: working electrode (WE), counter electrode (CE), and Ag/AgCl reference electrode (RE). Copper foil and the fabricated samples were used as a working electrode in catholytic part while platinum foil was used as a counter electrode in anolytic part. These two parts were separated by the proton-exchange membrane (PEM). Schematic of CO<sub>2</sub>RR experiment is shown in Figure 22.

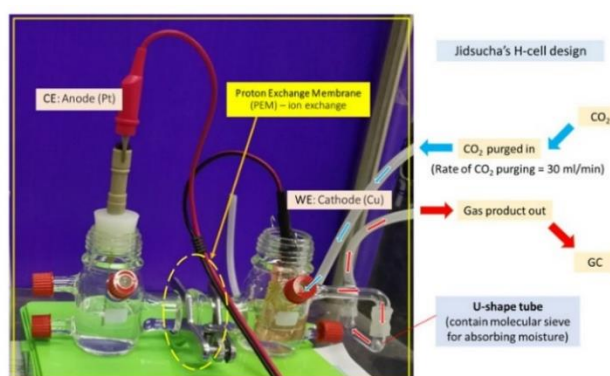


Figure 22 Schematic of CO<sub>2</sub>RR test.

The current density was acquired by the potentiostat. Subsequently, gas and aqueous products of CO<sub>2</sub>RR process were detected by gas chromatography (GC) and nuclear magnetic resonance (NMR), respectively. The schematics experiments, including the CO<sub>2</sub>RR and product detection were shown in Figure 23.

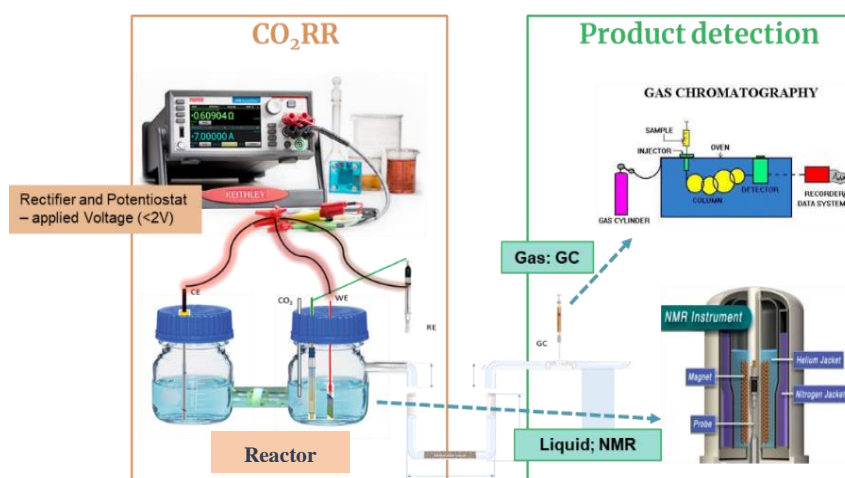


Figure 23 the overview of operation consisting of (a) CO<sub>2</sub>RR and (b) product detection.

## 4. Objectives

The Objective of this work are (1) for studying the relationship between processing parameters of copper-based catalytic electrode both porous fabrication and thermally oxidation processes and their performance for electrochemical conversion of carbon dioxide to valuable chemicals and (2) to study the directions to develop copper-based catalytic electrodes for electrochemical conversion of carbon dioxide to valuable chemicals by controlling structure and chemistry of the copper electrodes' surfaces.

## 5. Experimental

### 5.1) Sample Preparation procedure

#### Section 1: Electrodeposited porous copper electrocatalysts

##### 1.1) Constant-current electrodeposition

Copper foil was used as pure smooth copper sample in appendix 1 whereas nanostructured porous copper was represented copper catalytic electrode with developed surface by electrochemical method in section 1. Since, bath composition used in electrochemical process influence on the porous structure, the composition ratio of the electrolyte was optimized for acquiring the desirable porous structure. Electrodeposition of copper metal at cathode with higher concentration of  $\text{H}_2\text{SO}_4$  in  $\text{H}_2\text{SO}_4$  and  $\text{CuSO}_4$  electrolyte was generally used to fabricate porous copper by applying constant current for a time. Copper metal was deposited on copper foil substrate at cathode while hydrogen bubbles were also formed by reduction at the cathode as shown in Figure 24.

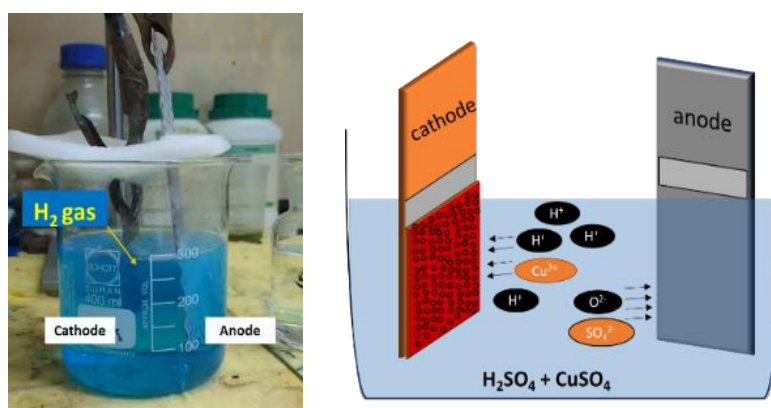


Figure 24 Constant-current electrodeposition.

This method called “Dynamic hydrogen bubble template (DHBT)”. Hydrogen formation create a model like a stack up of different size of hydrogen bubbles. More distance from substrate, small bubbles will coalesce and become larger as shown this schematic in Figure 25.

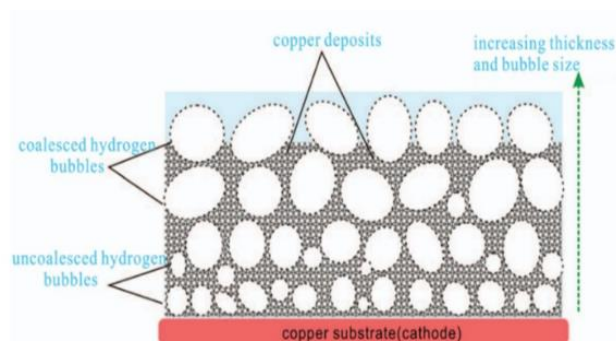


Figure 25 A stack up of different size of hydrogen bubbles which fabricated by Dynamic hydrogen bubble template (DHBT).

Porous copper was fabricated on the copper foil surface by varying composition ratio of  $\text{CuSO}_4$  and  $\text{H}_2\text{SO}_4$  with the controllable current density and deposition time. Three groups of porous copper samples, to be named porous A, B, and C, were fabricated by the process of copper electrodeposition on the high-purity copper foils (0.1 mm thick, 99.9999% purity, Alfa Aesar) with a dimension of 2.5 cm  $\times$  2.5 cm. The three groups differ from one another by the compositions of  $\text{H}_2\text{SO}_4$ ,  $\text{CuSO}_4$  and HCl in the plating solutions (300 ml). Concentration of  $\text{H}_2\text{SO}_4$  was fixed at 1.5M. The electrolyte B contains of twice as high  $\text{CuSO}_4$  concentration as electrolyte A whereas the HCl was added in electrolyte C in order to study effect of  $\text{CuSO}_4$  concentration and HCl addition, respectively. A standard setup of copper electrodeposition was employed at room temperature (28°C). Prior to electrodeposition, copper foil substrate was cleaned by propanol and acetone. Subsequently, the surface of copper foil was also prepared by immersing in the 5%  $\text{H}_2\text{SO}_4$  for 10 seconds. The porous fabrication is a two-electrode process: cathode and anode. Copper foil was used as cathode while the platinum mesh was used as anode. The current was applied to the two-electrode electrochemical cell by the rectifier. For each of the sample groups, the deposition was performed by varying applied current density (2, 3, and 3.5  $\text{A}/\text{cm}^2$ ), and deposition time (20, 40 and 60 s), resulting in 27 sub-sets of sample groups to consider the effect of current density and deposition time via their apparent pore size and percentage of apparent porosity. Moreover, for in depth study, this work focus on the representative of porous A, B, and C as A-3-40, B-3-40, and C-3-40. Electrolyte A (1.5M  $\text{H}_2\text{SO}_4$  and 0.2  $\text{CuSO}_4$ ), electrolyte B (1.5M  $\text{H}_2\text{SO}_4$  and 0.4  $\text{CuSO}_4$ ), and electrolyte C (1.5M  $\text{H}_2\text{SO}_4$  and 0.4  $\text{CuSO}_4$  + 0.05M HCl) composition and other parameters of constant-current porous copper fabrication is shown in Table 12. After deposition, samples were rinsed by DI water and dried.

Table 12 Parameters of constant-current porous copper fabrication.

Parameters	Details
Cathode	Copper foil (0.1 mm thick, 99.9999% purity, Alfa Aesar)
Anode	Platinum mesh
Sample area (cm <sup>2</sup> )	2.5 x 2.5 = 6.25 (Chemical Engineering, Chulalongkorn University)
	4.2 x 2.2 = 9.24 (Nanotec, NSTDA)
Current density (A/cm <sup>2</sup> )	3
Current (A)	6.25 x 3 = 18.75 (Chemical Engineering, Chulalongkorn University)
	9.24 x 3 = 27.72 (Nanotec, NSTDA)
Deposition time (s)	40
Temperature (°C)	Room temperature (28)
Electrolyte composition	(A) 1.5M H <sub>2</sub> SO <sub>4</sub> and 0.2M CuSO <sub>4</sub>
	(B) 1.5M H <sub>2</sub> SO <sub>4</sub> and 0.4M CuSO <sub>4</sub>
	(C) 1.5M H <sub>2</sub> SO <sub>4</sub> and 0.4M CuSO <sub>4</sub> + 0.05M HCl

### 1.2) Pulse Electrodeposition

This work focus on varying the pulse on time for pulse plating which can affect to the porous structure and deposition density compared to the constant current electroplating. Prior to deposit the pulsed electrodeposited samples, they were prepared by alkaline degreasing at 60°C. Subsequently, they were treated by 20% sulfuric acid and rinsed by DI water. Pulse electrodeposition was also a two-electrode process: cathode and anode. The high-purity copper foils (0.1 mm thick, 99.9999% purity, Alfa Aesar) was used as cathode with the same surface area as the constant-current porous copper fabrication while the platinum mesh was used as anode. The pulse electrodeposition set up was shown in Figure 26.



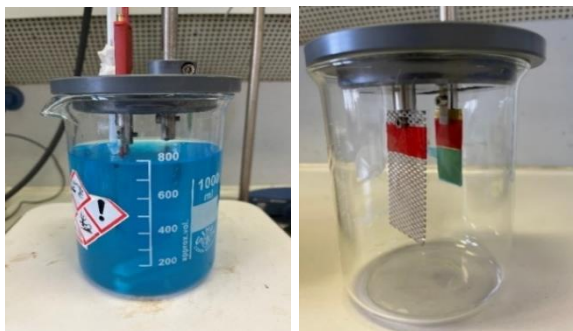


Figure 26 The pulse electrodeposition set up: (a) with electrolyte (b) copper foil cathode and platinum mesh anode.

The current was applied to the two-electrode electrochemical cell by the pulse rectifier. The 800 ml of bath composition composing of 0.5M  $\text{H}_2\text{SO}_4$  and 0.15M  $\text{CuSO}_4$  was used as electrolyte. The pulse electrodeposition was run at room temperature ( $20^\circ\text{C}$ ). Pulse off time was fixed at 10 milliseconds whereas pulse on time was varied as 1, 4, 10, and 20 milliseconds for P1-10, P4-10, P10-10, and P20-10, respectively. Applied current was also fixed at 2.75 A to consider the effect of pulse on time. Pulse electrodeposition parameters are shown in

Table 13 Parameters of pulse electrodeposited porous copper fabrication. After deposition, samples were also rinsed by DI water and dried.

Table 13 Parameters of pulse electrodeposited porous copper fabrication.

Parameters	Details
Cathode	Copper foil (0.1 mm thick, 99.9999% purity, Alfa Aesar)
Anode	Platinum mesh
Sample area ( $\text{cm}^2$ )	$2.5 \times 2.5 = 6.25$
Current density ( $\text{A}/\text{cm}^2$ )	0.44
Current (A)	2.75
Deposition time (s)	40
Temperature ( $^\circ\text{C}$ )	Room temperature (20)
Electrolyte composition	0.5M $\text{H}_2\text{SO}_4$ and 0.15M $\text{CuSO}_4$
Pause on time (ms)	1 for P1-10
	4 for P4-10
	10 for P10-10
	20 for P20-10

Pause off time (ms)	10
---------------------	----

### Section 2: Thermally-oxidized copper electrocatalysts

Smooth pure copper foil in appendix 1 was used as substrate for oxidized copper fabrication. The surface of copper foils was pre-treated with dilute HCl and consequently annealed in a furnace for 1 hour. The oxidizing temperatures of investigation are 300, 500, 800, and 1000°C. The thermal oxidation set up is shown in Figure 27 and the parameters of thermal oxidation are tabulated in the Table 14.



Figure 27 The thermal oxidation set up

Table 14 Parameters of thermally-induced copper oxides fabrication.

Parameters	Details
Sample area (cm <sup>2</sup> )	2.5 x 2.5 = 6.25
Oxidation time (h)	1
Oxidation temperature (°C)	300 for A300
	500 for A500
	800 for A800
	1000 for A1000

### Section 3: Copper oxide electrocatalysts thermally-induced from electrodeposited porous copper

Thermally-induced copper oxides from porous copper is an amalgamation of fabricated porous copper (A-3-40, B-3-40, and C-3-40) and oxidized copper (A300). The constant-current porous coppers were passing through the thermal oxidation at 300°C for 1 hour resulting of the thermally-induced copper oxides from porous copper as shown in the Figure 28.

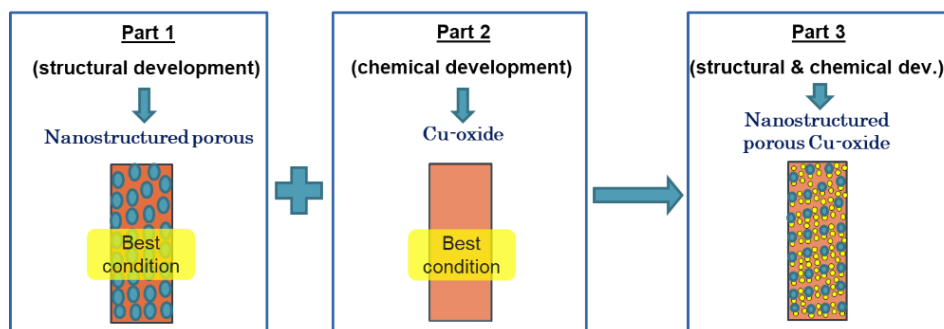


Figure 28 thermally-induced copper oxides from porous copper fabrication by combination of the best conditions of section 1 and section 2.

The thermally-induced copper oxides from porous copper set up is as of section 1 and section 2. The parameters of the thermally-induced copper oxides from porous copper are shown in the Table 15.

Table 15 Parameters of thermally-induced porous copper oxides fabrication.

Parameters	Details
Sample area (cm <sup>2</sup> )	2.5 x 2.5 = 6.25
Constant-current porous copper fabrication	
Cathode	Copper foil (0.1 mm thick, 99.9999% purity, Alfa Aesar)
Anode	Platinum mesh
Current density (A/cm <sup>2</sup> )	3
Current (A)	6.25 x 0.44 = 18.75
Deposition time (s)	40
Temperature (°C)	Room temperature (28)
Electrolyte composition	(A) 1.5M H <sub>2</sub> SO <sub>4</sub> and 0.2M CuSO <sub>4</sub>
	(B) 1.5M H <sub>2</sub> SO <sub>4</sub> and 0.4M CuSO <sub>4</sub>
	(C) 1.5M H <sub>2</sub> SO <sub>4</sub> and 0.4M CuSO <sub>4</sub> + 0.05M HCl
Thermally-induced copper oxides	
Oxidation time (h)	1
Oxidation temperature (°C)	300

## 5.2) CO<sub>2</sub> reduction reaction

After the sample fabrication, all samples were employed as the electrocatalyst in CO<sub>2</sub>RR process for investigating their performance. The CO<sub>2</sub>RR was run in the H-cell electrolyzer with three electrodes: working electrode (WE), counter electrode (CE), and Ag/AgCl reference electrode (RE). Copper foil and the fabricated samples

were used as a working electrode in catholytic part while platinum foil was used as a counter electrode in anolytic part. These two parts were separated by the proton-exchange membrane (PEM). CO<sub>2</sub>RR setup at Chemical Engineering, Chulalongkorn University and Nanotec, NSTDA are tabulated in Table 16 and Table 17, respectively. Schematic of H-cell setup at Chemical Engineering, Chulalongkorn University and flat-cell setup at Nanotec, NSTDA are shown in Figure 29 and Figure 30.

Table 16 CO<sub>2</sub>RR setup at Chemical Engineering, Chulalongkorn University.

Parameters	Details
Working electrode (WE)	Copper foil, fabricated electrocatalyst: Cu (EP)
	Constant-current porous copper (A-3-40, B-3-40, C-3-40)
	Thermally-induced copper oxides (A300)
	Thermally-induced copper oxides from porous copper (PAA300, PBA300, PCA300)
Counter electrode (CE)	Platinum foil
Reference electrode (RE)	Ag/AgCl
Type of reactor	H-cell electrolyzer
Proton-Exchange Membrane (PEM)	Nafion 117
Sample area (cm <sup>2</sup> )	2.5 x 2.5 = 6.25
Applied voltage (V vs. Ag/AgCl)	-1.3
Electrochemical method	Chronoamperometry (CA)
Deposition time (min)	70
Temperature (°C)	Room temperature (28)
Electrolyte composition	CO <sub>2</sub> saturated in 0.1M KCHO <sub>3</sub> (for section 1 and section 3)
	CO <sub>2</sub> saturated in 0.5M KCHO <sub>3</sub> (for section 2)
Rate of CO <sub>2</sub> purge (ml/min)	10
pH of electrolyte	6.8 ± 0.2



Figure 29 Schematic of CO<sub>2</sub>RR setup at Chemical Engineering, Chulalongkorn University.

Before CO<sub>2</sub>RR test, CO<sub>2</sub> gas was purged with 10 ml/min in to the 300 ml electrolyte of the catholytic part. The pH value of saturated CO<sub>2</sub>/KHCO<sub>3</sub> must be  $6.8 \pm 0.2$ . The 0.1 M KHCO<sub>3</sub> was used in experiment of constant-current porous copper and the thermally-induced copper oxides from porous copper whereas the 0.5 M KHCO<sub>3</sub> was used in experiment of oxidized copper. The electrical energy was applied with constant potential by Chronoamperometry (CA) method to generate CO<sub>2</sub>RR process for 70 minutes.

Table 17 CO<sub>2</sub>RR setup at Nanotec, NSTDA.

Parameters	Details
Working electrode (WE)	Copper foil and porous B-3-40
Counter electrode (CE)	Platinum foil
Reference electrode (RE)	Ag/AgCl
Type of reactor	Flat cell
proton-exchange membrane (PEM)	Selemion
Sample area (cm <sup>2</sup> )	4.2 x 2.2 = 9.24
Applied voltage (V vs. Ag/AgCl)	-1.3, -1.8, -2.3
Electrochemical method	Chronoamperometry (CA)
Deposition time (min)	70
Temperature (°C)	Room temperature (28)
Electrolyte composition	CO <sub>2</sub> saturated in 0.1M KCHO <sub>3</sub>
Rate of CO <sub>2</sub> purge (ml/min)	10
pH of electrolyte	$6.8 \pm 0.2$

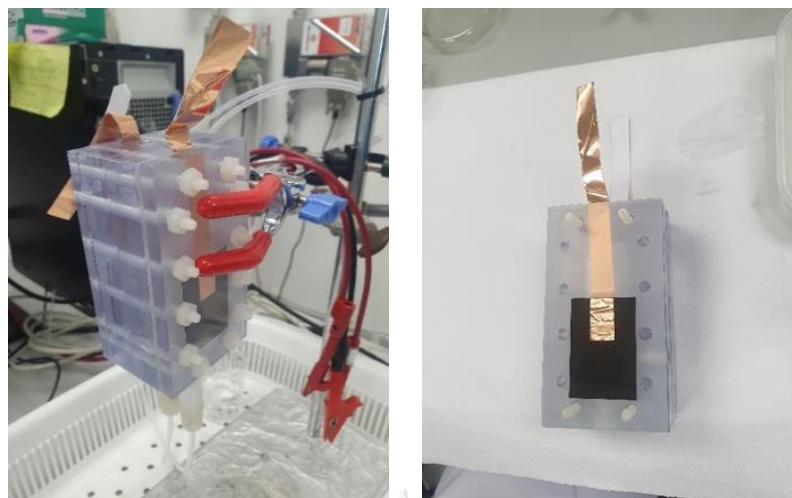


Figure 30 Schematic of CO<sub>2</sub>RR setup at Nanotec, NSTDA.

## 6. Result and discussion

### Section 1: Electrodeposited porous copper electrocatalysts

#### 1.1) Porous copper fabrication

A hierarchical copper structure composes of a lot of pores inside consisting of large and small micro pores overlap each other. In additions, there are plenty of more nano pores locating beside these pores. Therefore, the porous structure would have much higher of surface area providing high gas permeability and low density. The surface of porous copper which fabricated by pulse electrodeposited porous copper seems more uniform and denser than of the constant-current porous copper. The characteristics of them were described in the following topic.

##### 1.1.1) Constant-current electrodeposition

It was found that the fabricated porous A and porous B seems brown-black color surface, but porous C has a lighter color surface due to the HCl in the bath solution. After deposition, the layer of porous C appears thicker than of the other porous coppers. The small and large pores of the obtained porous structure were stacked up from the substrates. Although, these porous coppers could be swept out from their substrate, they have sufficient strength for being as catalytic electrode. The applied current was constant at 18.75 A for all 40 seconds. Three constant-current porous coppers after deposition are shown in Figure 31.



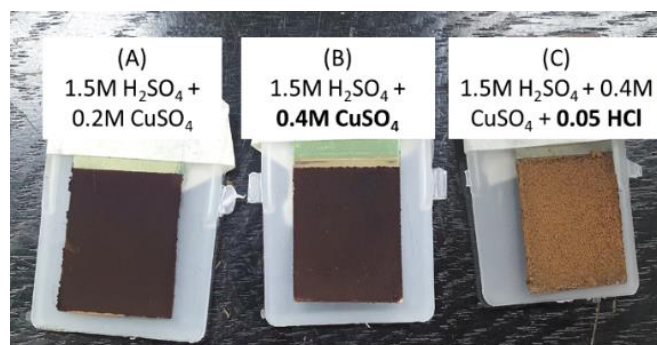


Figure 31 Surface appearance of the constant-current porous copper in groups (a) A, (b) B, and (c) C varying by bath solution composition.

### 1.1.2) Pulse Electrodeposition

Pulse electrodeposition consists of two main processes (pulse on time and pulse off time). During pulse on time, copper ion in the solution bath attracted to cathode and be reduced as copper metal deposited on the substrate similar to typical constant-current method. On the other hand, current become zero during pulse off time causing no copper deposition. Therefore, copper ion in solution bath has more time to replenish itself preparing to repeat the deposition in the range of pulse on time. These processes will occur alternately together until reaching the deposition time. The pulse electrodeposited porous coppers appearance and the square-waved relation of voltage (blue line), current (red line) and deposition time (s) of P1-10, P4-10, P10-10 and P20-10, respectively are shown in Figure 32. Each condition of pulse electrodeposited porous copper was fabricated for 40 seconds to compare the porous structure with the constant-current porous copper. Furthermore, they also were fabricated for 80 seconds to compared with pulse electrodeposited porous copper fabricated for 40 seconds. The pulse signal was selected as the square-waved pattern. The pulsed signal should be as a regular square-waved graph, but it has some gradient before reaching to the pulse on time and pulse off time due to the extremely short range of pulse on time and pulse off time. The peak of pulse current should reach at 2.75 A but it reached at 2.5 A. Moreover, the current from zero to 2.5 A still acted as the regular square-waved shape, excepting the current range from 2.5 A to 2.75 A and from 0.3 A to zero.

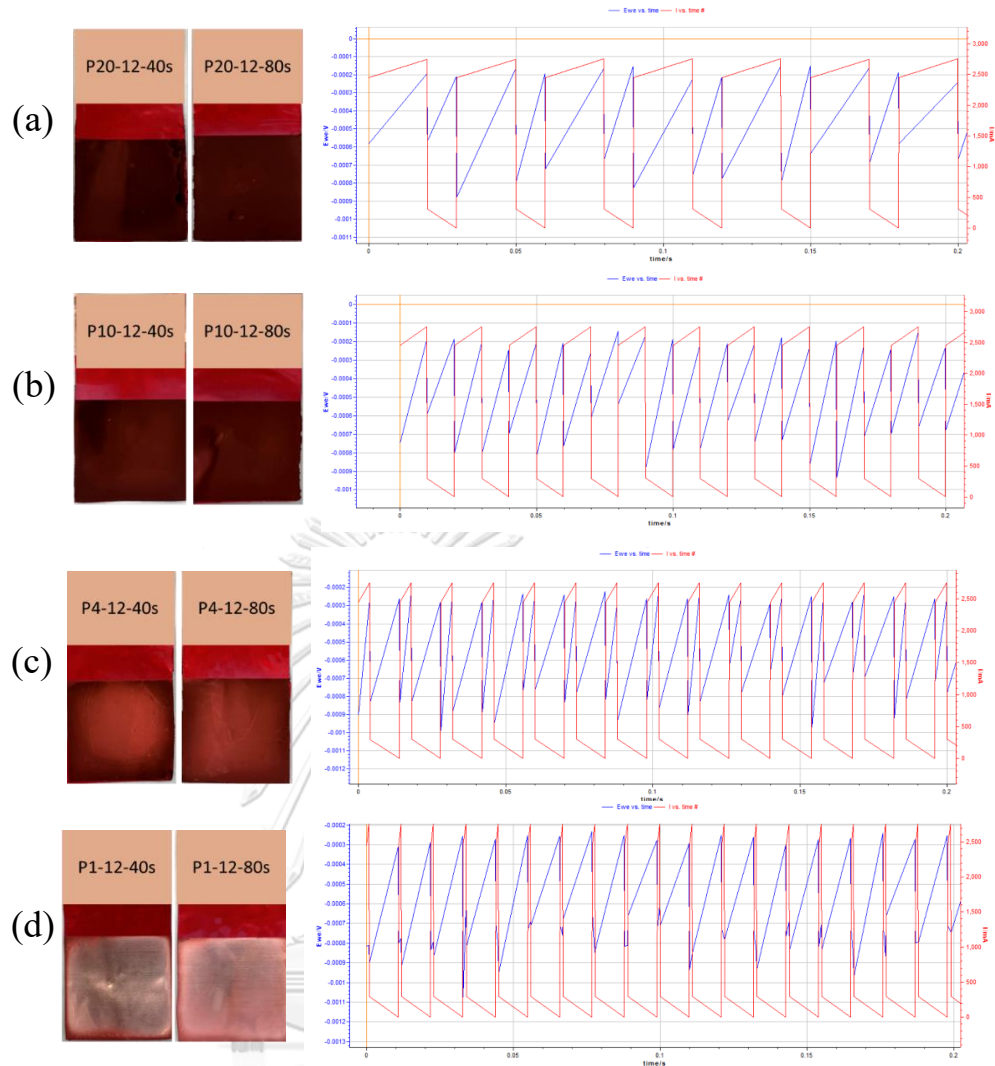


Figure 32 Surface appearance of the pulse electrodeposited porous copper P1-10, P4-10, P10-10 and P20-10, respectively which varying pulse on time: 1, 4, 10, and 20 ms, respectively with fixed pulse off time at 10 ms and current density  $0.44\text{A}/\text{cm}^2$ .

## 1.2 Sample characterization

### 1.2.1) Surface morphology and pore characteristics of constant-current porous copper

#### 1.2.1.1) Surface morphology and pore characteristics

Surface morphology and pore characteristics of all 27 sub-sets of constant-current porous coppers, which captured by OM and analyzed by Image J software. Figure 33a, Figure 33b, and Figure 33c show the morphology of the samples in group A, group B, and group C, respectively, prepared by varying applied current densities and deposition times. It is evidenced that the distribution of pore sizes of group A and group B as observed from the surface is rather more uniform than of group C, and that both two parameters significantly affect the apparent pore size and apparent porosity



observed at the surface. Both apparent pore size and apparent porosity of group C samples are larger than those of the other two groups. This is clearly owed to the effect of HCl addition in the plating bath that promotes hydrogen generation and bubble coalescence. HCl can reduce a branch size as presented in previous works. Therefore, its structure seems tearing from each other become a coral shape.

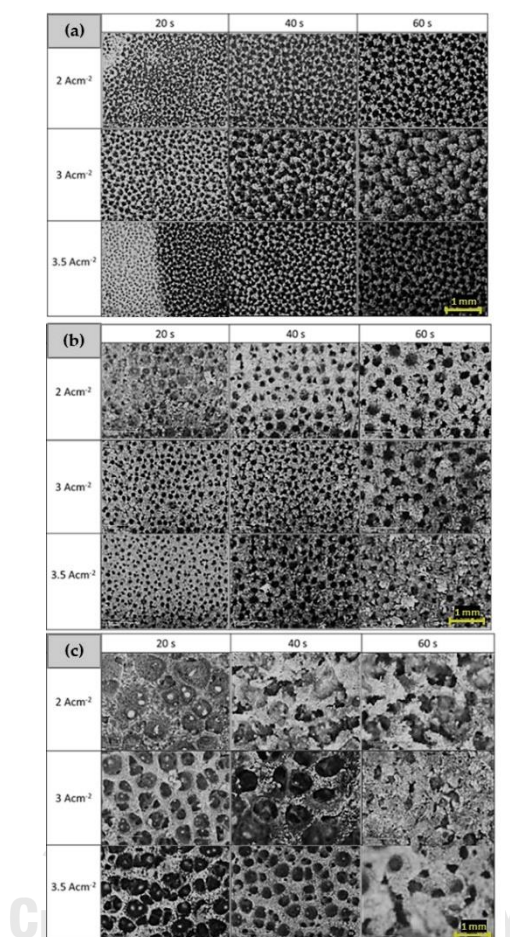


Figure 33 2D-Surface morphology of the constant-current porous copper in groups (a) A, (b) B, and (c) C varying by current density and deposition time.

Particularly, the decrease of applied current density and the increase in deposition time led to enlargement of apparent pore size. This may be attributed to slow rates of hydrogen evolution in conjunction with bubble coalescence in such conditions [81, 84, 88]. The effects of the two parameters on apparent porosity is however inconclusive, and the values of apparent porosity vary less significantly as compared to pore size.

The group B samples exhibit similar or higher apparent pore size and apparent porosity. Since the ratio of  $H^+/Cu^{2+}$  is lower for group B, this may imply

that the group B samples comprise of a lower number of smaller-sized pores, in a nano regime, which were not clearly captured by image J software. The group C has the highest apparent pore size and apparent porosity differentiate from other previous groups. Apparent pore size and apparent porosity of all 27 sub-sets of sample groups are plotted as shown in Figure 34. From their result, it has some observation that increase in applied current density provide smaller apparent pore size and lower percentage of apparent porosity but increase in deposition time provide larger pore size and higher percentage of apparent porosity although it may unclear totally. Even though, it may be used as a trend to study further.

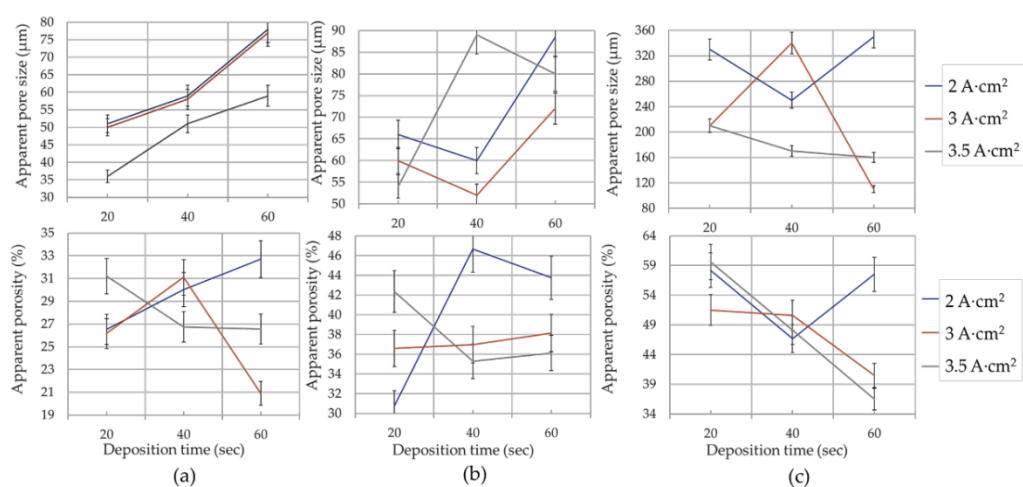


Figure 34 Apparent pore size and apparent porosity of the constant-current porous copper in groups (a) A, (b) B, and (c) C varying by current density and deposition time.

จุฬาลงกรณ์มหาวิทยาลัย

For in depth analysis, the representative samples of the three groups, namely A-3-40, B-3-40, and C-3-40, that were electrodeposited with 3 A/cm<sup>2</sup> for 40 seconds, were characterized in more details, and their respective characteristics and properties are summarized as following. The OM images and their analyzed result from Image J of the representatives are shown in Figure 35.

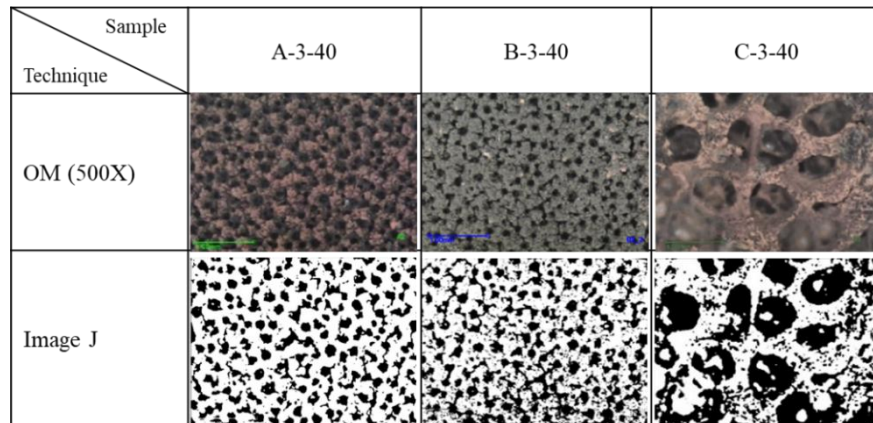


Figure 35 OM image and Image J analysis of A-3-40, B-3-40, and C-3-40.

Considering the analysis of 2D-pore characteristics, both apparent pore size and percentage of apparent porosity of A-3-40, B-3-40, and C-3-40 are plotted with current density at fixed deposition time (40 seconds) as presented in Figure 36. It suggests that C-3-40 provide the highest apparent pore size and percentage of apparent porosity while percentage of apparent porosity of B-3-40 is higher than of A-3-40 with identical pore size.

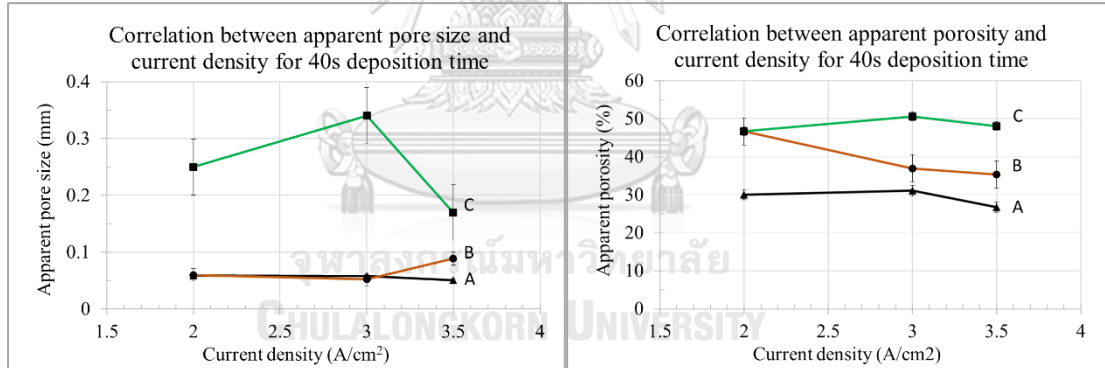


Figure 36 Apparent pore size and apparent porosity of A-3-40, B-3-40, and C-3-40 varying current density with deposition time 40 second.

Moreover, the cross-sectioned microstructure of porous coppers was also captured by SEM to investigate the correlation between pore distribution and copper deposition both inside the porous structure (PX) and at the interface (PX-IF). The cross-sectioned microstructure of A-3-40, B-3-40 and C-3-40 with magnification 1000X and 4000X are also shown in Figure 37 and Figure 38, respectively. It was found that there were small and large pores inserting between the copper deposits indicating that some pores were coalescent together inside the porous structure of A-3-40 and B-3-40. The deposited copper particle of A-3-40 appear to be finer than of B-3-40. Shape of some copper particles of B-3-40 seems like cube-shaped or polygonal-shaped which differentiate from of A-3-40. The cube-shaped with larger

particle size of copper deposit of C-3-40 were obviously. Moreover, there are some cracks at the interface between the porous structure and the substrate due to the metallurgical polishing; therefore, some copper particles flake off from the interface, especially C-3-40. However, this can indicate that the copper deposit of C-3-40 was obvious as the cube-shaped particle with larger size than of other two porous coppers.

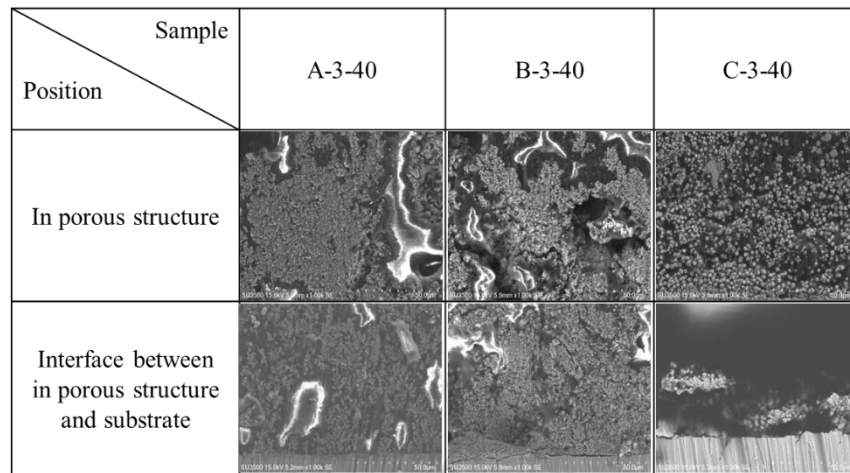


Figure 37 The cross-sectioned microstructure of A-3-40, B-3-40 and C-3-40 with magnification 1000X: PX (in porous structure) and PX-IF (interface between porous structure and substrate).

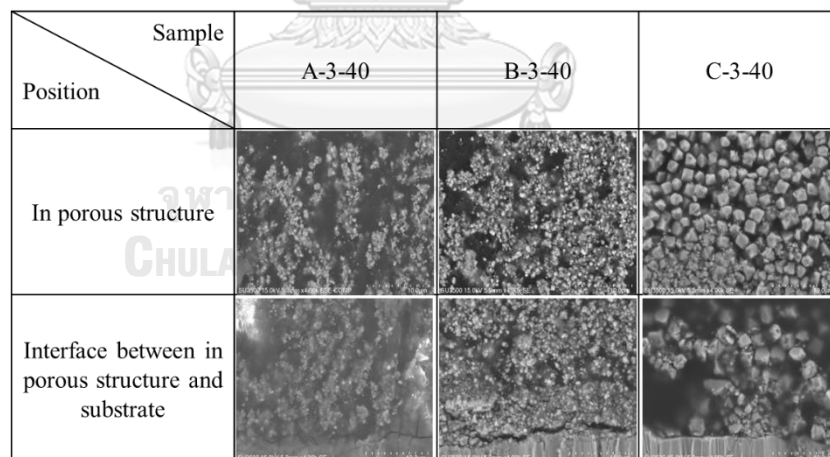


Figure 38 The cross-sectioned microstructure of A-3-40, B-3-40 and C-3-40 with magnification 4000X: PX (in porous structure) and PX-IF (interface between porous structure and substrate).

To investigate sample analysis deeper in details, 3D-characteristics is required. SEM images of smooth copper foil, and porous coppers were magnified from top to bottom (2000X, 5000X, and 15000X, respectively) as illustrated in Figure 39. Structure of copper foil obvious as a simple planar. The 3D image of A-3-40 appear

as many grape seeds locating on dendrite structures. B-3-40 structure seems like a flower-like dendrites. A lot of surface area of B-3-40 were overlap each other. C-3-40 structure seems something that was teared from each other as a coral-shape. The branch size of C-3-40 was reduced due to the effect of HCl addition whereas the huge pores was also formed due to the higher amount of hydrogen ion in the bath composition.

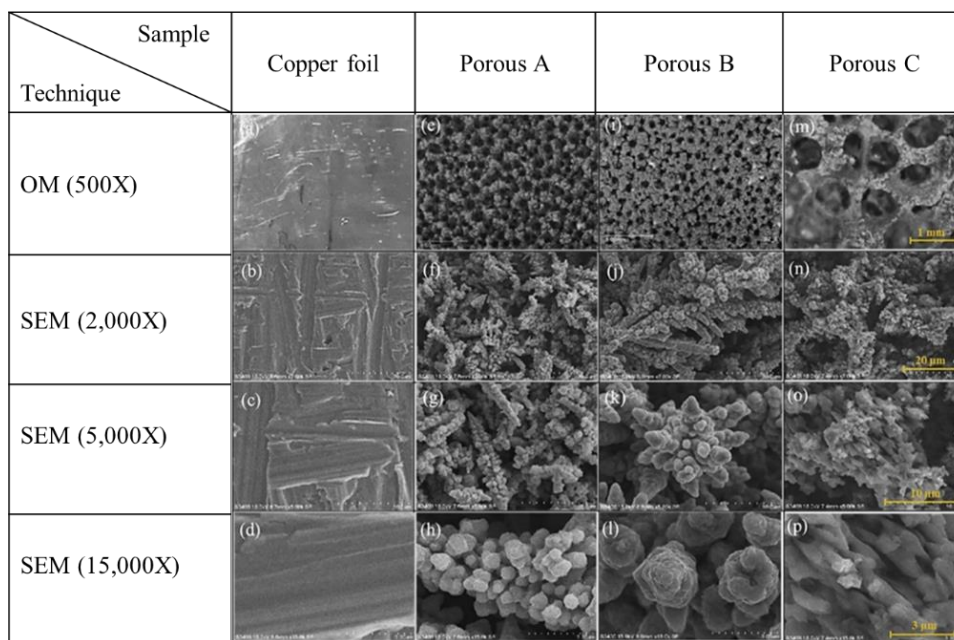


Figure 39 Microstructure of Cu foil (a–d), and porous Cu deposits from groups A (e–h), B (i–l), and C (m–p), electrodeposited with 3 A/cm<sup>2</sup> for 40 s, presented at different magnifications.

#### 1.2.1.2) 3D-Surface roughness

The 3D-morphology and surface roughness of constant-current porous coppers were also analyzed by 3D optical profiler as shown in Figure 40. All images were captured at 50X magnification. There are two values of surface roughness: arithmetic average roughness (Ra) and the average value of the absolute values of the heights of five highest-profile peaks and the depths of five deepest alleys within the evaluation length (Rz).



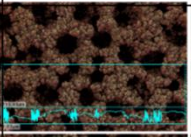
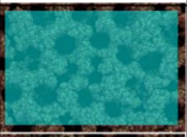
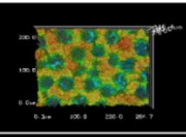
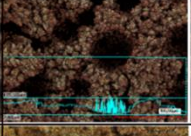

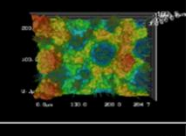


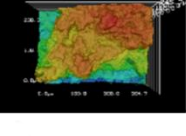
Sample \ Technique	Line scan	Area scan	3D- morphology	Roughness ( $\mu\text{m}$ )	
				Ra	Rz
A-3-40				25.03	162.58
B-3-40				41.43	222.81
C-3-40				49.35	179.61

Figure 40 The 3D-morphology captured by 3D optical profiler and surface roughness value of constant-current porous coppers.

Surface roughness of A-3-40 was less than of B-3-40, and C-3-40, respectively as shown in Figure 41, which has the same trend with the apparent porosity. The Ra value represent the average surface area whereas Rz can be used to differentiate the average of peak and the valley of each sample. Average surface roughness (Ra) of A-3-40, B-3-40, and C-3-40 were 25.03, 41.43, 49.35  $\mu\text{m}$ , respectively. Moreover, Rz value of A-3-40, B-3-40, and C-3-40 were 162.58, 222.81, 179.61  $\mu\text{m}$ , respectively, indicating that B-3-40 has the most height between the peak and the valley as correlate with the 3D structure captured by SEM. Many particles of deposited copper were overlap each other acquiring the high peak and low valley. Surface roughness of A-3-40 is low because its porous structure was order arrangement. Ra value of C-3-40 was high, but Rz value was less than of B-3-40. It could indicate that the shorter distance between the peak and the valley caused by the shorter branch of porous C.

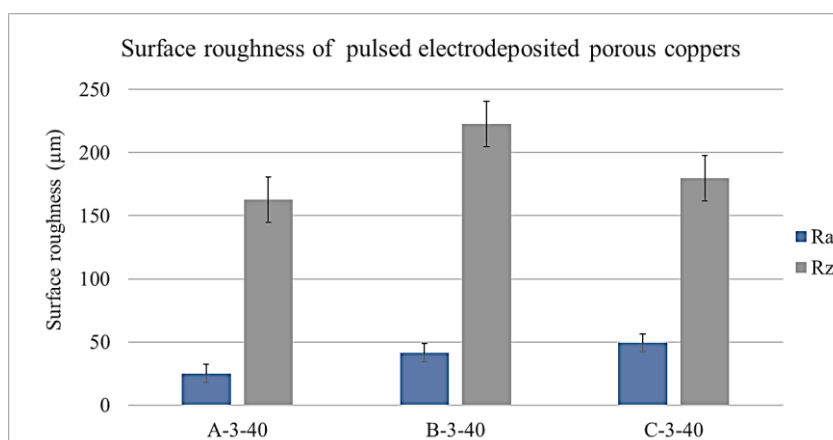


Figure 41 The correlation between surface roughness of the representative constant-current porous copper (A-3-40, B-3-40, and C-3-40).

### 1.2.1.3) True surface area and pore distribution

CO<sub>2</sub>RR occurs at the interphase between liquid phase (aqueous electrolyte) and solid phase (the surface of the catalyst) as heterogeneous reaction. Amount of active site at the surface is crucial factor to increase the performance of CO<sub>2</sub>RR. Therefore, surface area analysis is required. Indeed, upon a closer examination using Brunauer–Emmett–Teller (BET) by the physical adsorption, the buildup one monolayer of gas on the surface can be calculated to the surface area. It is found that the true surface area of A-3-40 was much higher than of porous B and porous C, respectively (Table 18) based on the surface area of each electrode, indicating the large number of nano-pores distributed along the struts of the porous copper structure.

The magnified microstructure of the A-3-40 sample (Figure 39), composing of clusters of sub-micron particulates and nano-pore in between each particulate, underlines this observation.

Table 18 Pore characteristics of Porous A-3-40, Porous B-3-40, and Porous C-3-40 copper.

Pore Characteristics	A-3-40	B-3-40	C-3-40
Apparent pore size	58	52	340
Apparent porosity	31.11	36.96	50.63
BET surface Area (m <sup>2</sup> /g)	19.56	4.00	3.75
Surface area (m <sup>2</sup> /electrode)	1.263	0.354	0.201
BJH pore distribution (nm)	2-16	2-16	2-16
Surface roughness (Ra)	25.03	41.43	49.35
Surface roughness (Rz)	162.58	222.81	179.61

Moreover, the Barrett-Joyner-Halenda (BJH) pore size & volume analysis was also used to explain the pore distribution. The BJH graph also confirms that C-3-40 has the largest pore size. Pore distribution of C-3-40 was mostly in the range of 13-14 nm with slightly 8-10 nm and 3-4 nm, respectively. On the other hand, most of pore size of A-3-40 and B-3-40 were in the range of 2-4 nm with some 12-14 nm, and 5-9 nm pores. Generally, nano means one part per billion or 10<sup>-9</sup> and micro means one part per million or 10<sup>-6</sup>. On the other hand, according to pore size of IUPAC classification system, there are three main types of pores: micropores (below 2 nm pore size), mesopores (between 2 and 50 nm pore size), and macropores (above 50 nm pore size) as illustrated in Figure 42. From this classification, all constant-current porous coppers are mesoporous materials because their pore size were in the range of 2 and 50 nm.

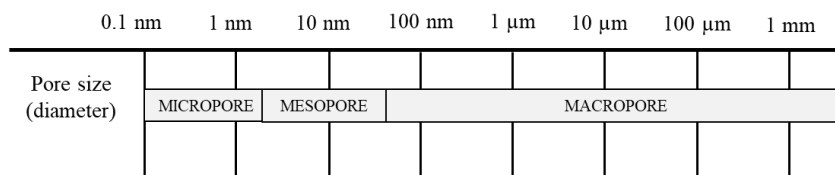


Figure 42 Pore size of IUPAC classification system.

Obviously, from the graph of A-3-40, it seems like A-3-40 has various range of pore size indicating that it has higher distribution of pore than of B-3-40. The BET isotherm graph and BJH pore distribution graph of porous coppers are shown in Figure 43. Therefore, that is a result that porous A has the highest surface area as seen by BET result. Moreover, the true surface area and the pore distribution also relate to the morphology.

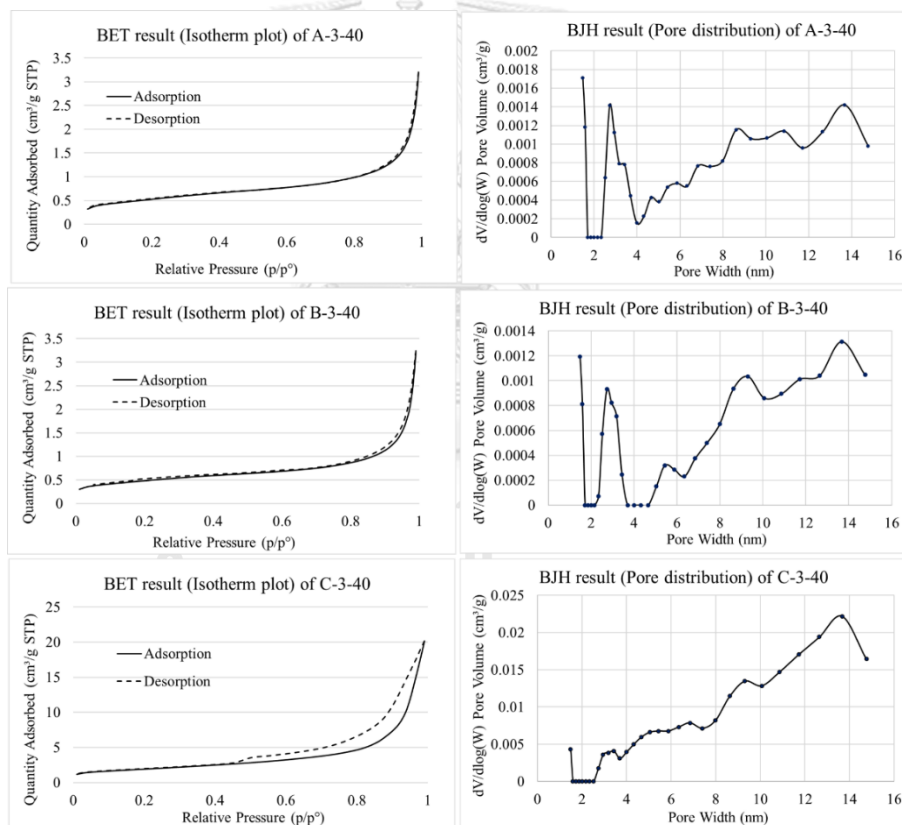


Figure 43 Isotherm plot of BET analysis and BJH pore distribution analysis results of A-3-40, B-3-40, and C-3-40.



#### 1.2.1.4) Apparent density, Electrodeposition efficiency, and True porosity calculation

Apparent density of porous coppers was calculated to compare their physical property. Mass of fabricated porous samples, area of the substrate, and thickness of the porous layer are required as shown in equation (3). To measure the thickness, each fabricated porous sample was cut from the edge into almost of the middle of sample. Subsequently, the cut sample was dipped into the liquid nitrogen to freeze the microstructure before separating into 2 pieces as shown in Fig. This process can deliver the cross-sectioned microstructure analysis of the porous coppers. Thickness of each porous copper was an average value which calculated from 10-time measurement from both SEM micrographs of 2 sides of sample.

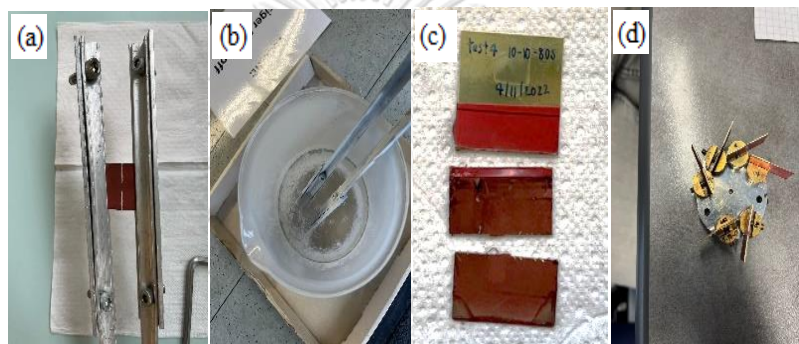


Figure 44 The process of cross-sectioned microstructure analysis of the porous coppers (a) the fabricated porous sample cut from the edge into almost of the middle of sample, (b) the cut sample dipped into the liquid nitrogen, (c) after separating the sample into 2 sides of sample, and (d) sample prepared to be analyzed by SEM

The result showed that B-3-40 has higher apparent density than of A-3-40, and C-3-40, respectively. In additions, the electrodeposition efficiency was also calculated to support the apparent density result. The electrodeposition efficiency calculation is presented in equation (4). It provides the same trend as the apparent density. The B-3-40 has higher electrodeposition efficiency than of A-3-40, and C-3-40, respectively. Moreover, the true porosity is the most important calculation for 3D-porous structure characterization. The true porosity calculation is presented in equation (5). The result show that B-3-40 has lower true porosity than of A-3-40, and C-3-40, respectively. For all calculations show that there were the same trend of porous structure calculation indicating that B-3-40 was the densest porous structure. This can imply that there was more concentration of copper ion in the bath solution B than of bath solution A. Moreover, compared to C-3-40, although there was the same concentration of copper ion in bath solution, HCl reduce the branch size of the porous

C structure. Therefore, apparent density of C-3-40 was less than of B-3-40. The calculation values are presented in Table 19.

$$\text{Apparent density (g/cm}^3\text{)} = \frac{\text{mass}}{\text{substrate area} \times \text{thickness}} \quad (3)$$

$$\text{Electrodeposition efficiency}(\varepsilon_f) = \frac{\text{weight} \times \text{interchanged electron} \times \text{Faradaic constant}}{\text{Current} \times \text{time} \times \text{Atomic weight}} \quad (4)$$

$$\text{True porosity} = \left(1 - \frac{\text{apparent density of sample}}{\text{density of matel}}\right) \times 100 \quad (5)$$

Table 19 Calculation for pore characteristics.

Characteristics for calculation	A-3-40	B-3-40	C-3-40
Mass of porous Cu (g)	0.065	0.088	0.054
Thickness of porous Cu (cm)	0.0141	0.0221	0.0222
Apparent density (g/cm <sup>3</sup> )	0.739	0.638	0.390
Electrodeposition efficiency (ε <sub>f</sub> )	2.584	3.498	2.146
True Porosity (%)	91.755	92.884	95.652

It is obvious that bath compositions (A, B, and C) largely influence the developed porous structure of the copper deposits. Not only their difference in terms of apparent pore size and apparent porosity, but their detailed features of deposit nodules along the struts of the porous structure also appear to vary largely. BET surface area, apparent pore size, apparent porosity, apparent density (determined from the coating mass and layer thickness), and true porosity. Overall, the true porosity obtained in this work falls in the range of the copper deposits' porosity obtained by the research of Shin et al. (93.30–97.77%).

#### 1.2.2) Surface morphology and pore characteristics of pulse electrodeposited porous copper

There are some correlations between the percentage of duty cycle, which is calculated by the equation (6), and the obvious porous copper morphology.

$$\% \text{ duty cycle} = \frac{\text{pulse on time}}{\text{pulse on time} + \text{pulse off time}} \times 100 \quad (6)$$

Percentage of duty cycle are 9.09, 28.57, 50.00, and 66.67 for P1-10, P4-10, P10-10 and P20-10, respectively. The morphology of sample which fabricated by less

pulse on time was obviously has a finer structure with smaller particles indicating that less duty cycle can deliver more homogeneous and finer porous structure as suggested by the previous studies. Moreover, increase in pulse on time supported the longer time for copper deposition causing the deposition is similar to the direct current deposition method. For 10 milliseconds pulsed off time, grain of deposited copper at the pulse on time will growth. Therefore, the longer pulse off time, the more grain growth causing the larger particles of copper and less homogeneous.

Surface roughness was observed by line scan to consider the peak and the valley performance and by area scan to get the value of surface roughness. Moreover, the 3D-surface roughness image was also captured. Surface roughness result of PX-10-40s samples were shown in Figure 45.

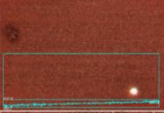

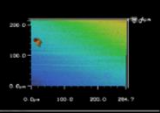
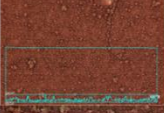

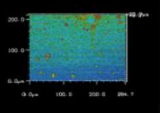
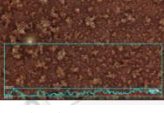

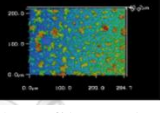
Sample \ Technique	Line scan	Area scan	3D- morphology	Roughness ( $\mu\text{m}$ )	
				Ra	Rz
P4-10-40s				1.89	36.32
P10-10-40s				1.76	22.96
P20-10-40s				4.42	39.48

Figure 45 The 3D-morphology captured by 3D optical profiler and surface roughness value of pulse electrodeposited porous coppers with 40 s deposition time.

Furthermore, Figure 46. shows the surface roughness of samples both fabricated for 40 seconds by the constant-current method (PX) and by pulsed electrodeposition (PX-10-40s). It was observed that the surface roughness of PX were much higher than of PX-10-40s suggesting that pulse electrodeposition contribute the denser porous structure and more uniform compared to the constant-current method. Moreover, there were a lot of difference between peak height and valley depth of the porous structure. Comparing in the pulse electrodeposited porous copper; P20-10-40s has the most trend similar as the constant-current due to higher pulse on time than P10-10-40s and P4-10-40s, respectively. Therefore, more pulse on time encouraging the increase of surface roughness. On the other hand, the P1-10-40s deposition was not uniform. It has some copper deposit at only the edge not covering all the copper foil substrate. Therefore, it was neglected to compare with other PX-10-40s because the surface roughness should be compared at the same place of the substrate.

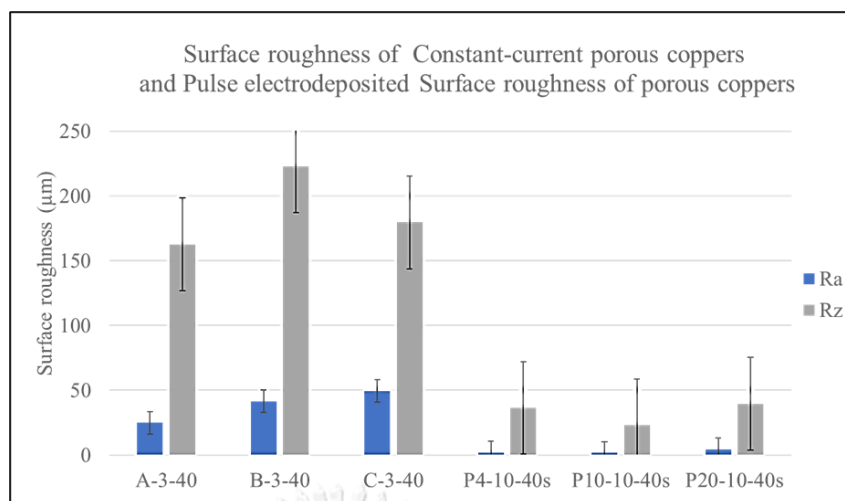


Figure 46 Surface roughness of constant-current porous coppers and pulse electrodeposition for 40 s deposition time.

The copper deposition will be probably better if providing more deposition time. The copper particles were larger for P4-10, P10-10, P20-10, respectively. For P20-10, some large chunks of copper particles were obvious. Therefore, it also correlates with the surface roughness result. Moreover, pulsed electrodeposition was also tested for 80 seconds (twice of 40 s) to study the effect of deposition time on the deposition efficiency to be a guideline for next works. There were some larger chunks of copper particle appearing on the surface, especially P20-10 for 80 seconds. The surface roughness of PX-10-40s and PX-10-80s are shown in Figure 47. The results of PX-10, which deposited for 80 seconds, contribute more surface roughness approximately two times of samples, which deposited for 40 seconds as shown in Figure 48.

Sample \ Technique	Line scan	Area scan	3D- morphology	Roughness (μm)	
				Ra	Rz
P4-10-80s				4.08	31.35
P10-10-80s				6.47	59.96
P20-10-80s				9.49	61.78

Figure 47 The 3D-morphology captured by 3D optical profiler and surface roughness value of pulse electrodeposited porous coppers with 80 s deposition time.

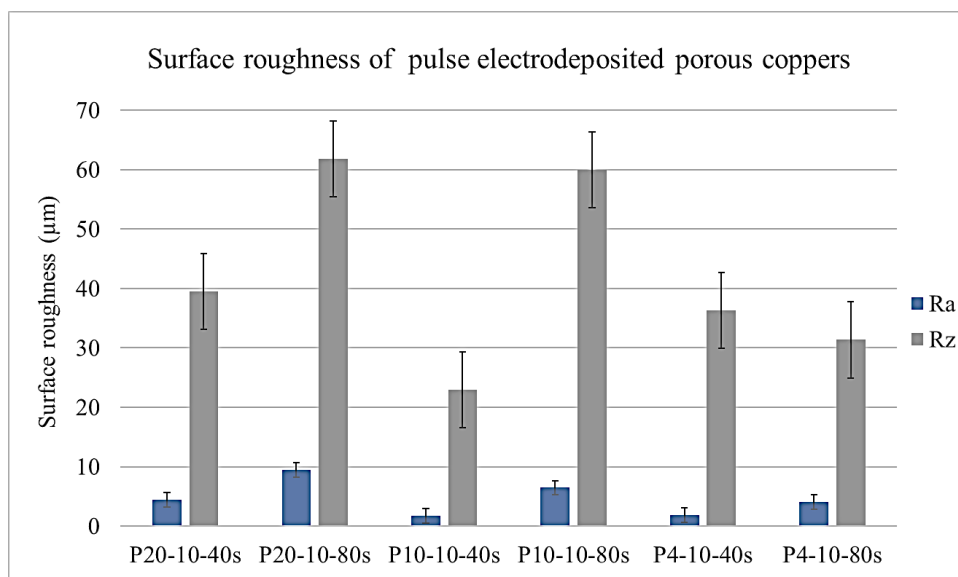


Figure 48 Surface roughness of pulse electrodeposited porous coppers.

The finer and more uniform porous structure of pulse electrodeposited porous copper which deposited for 40 and 80 seconds are shown in Figure 49. Porous copper which deposited for 80 seconds seems to have more copper particles deposition. Porous copper deposited with higher pulse on time tend to have more similar porous structure to the constant-current porous copper than of less pulse on time.

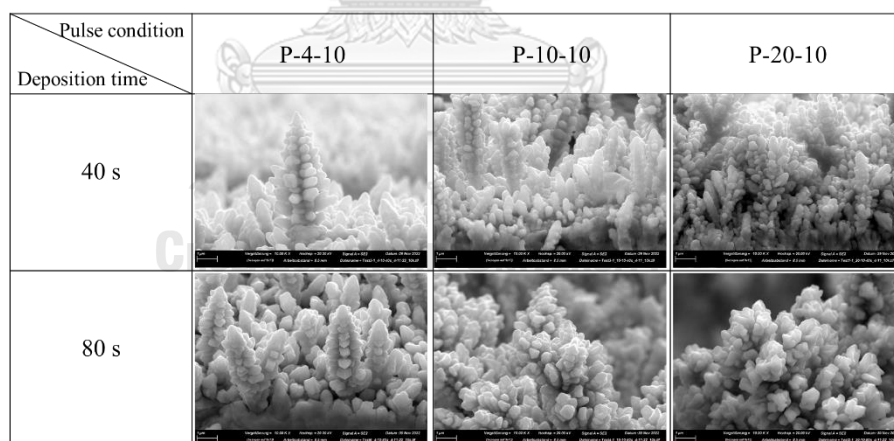


Figure 49 Microstructure of pulse electrodeposited porous copper which deposited for 40 and 80 seconds

Moreover, the pulse electrodeposited porous copper was also compared the surface roughness and 3D-profile with the constant-current porous copper by controlling the applied current density at  $0.44 \text{ A/cm}^2$  and deposition time for 40 seconds to analyze the effect of electrodeposition method. The result is presented in Figure 50.



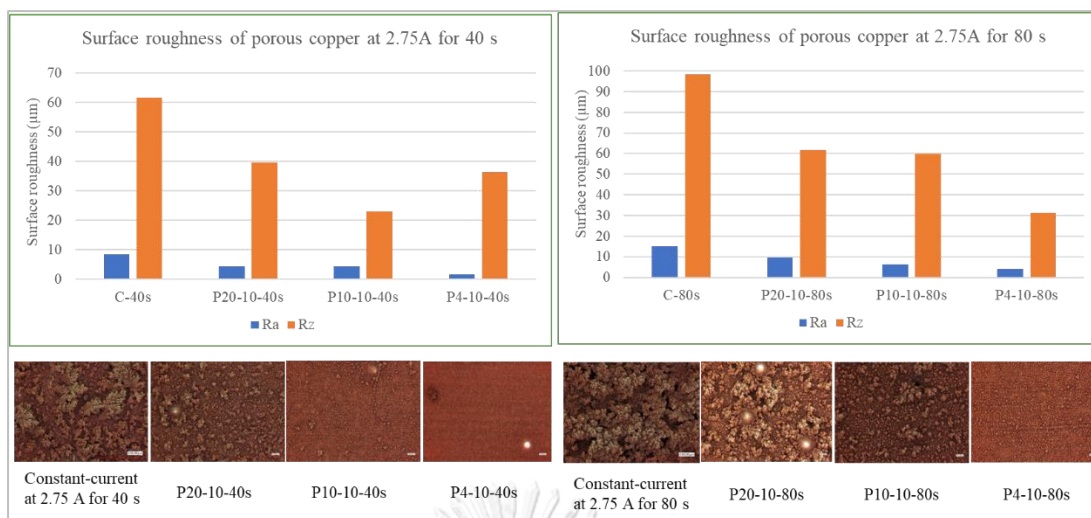


Figure 50 Comparison of surface roughness and microstructure of the constant-current and pulse electrodeposited porous copper by controlling the applied current density at  $0.44 \text{ A/cm}^2$  and deposition time for 40 seconds

The surface roughness has a similar trend to the morphology. Pulse electrodeposited porous copper with lower pulse on time provide finer and less surface roughness, the huge pore size also reduces. uniform size of pore may cause the higher selectivity of  $\text{CO}_2\text{RR}$  product. Therefore, the pulsed electrodeposition is a proposed candidate method to fabricate the porous copper catalyst.

### 1.2.3) Chemical composition

In addition to the physical property, the chemical composition of porous copper was also analyzed to compare with copper foil and relate to the  $\text{CO}_2$  reduction selectivity. The bulk composition was detected by EDX analysis as shown in Figure 51 presenting those porous coppers has higher percentage of oxygen than of copper foil. Moreover, it was found that the bulk composition of C-3-40 has higher percentage of oxygen than other two porous coppers. It can imply that surface area may correlate to chemical composition. However, while the presenting data of oxygen cannot be taken as absolute values, as oxygen is considered a light element for EDX analysis, and more advanced chemical analysis techniques would be required to determine the exact oxygen contents, it can be observed and qualitatively analyzed that the measured oxygen contents of the porous copper samples deviate (increase) rather significantly compared to the copper foil. This suggests the role of porosity in promoting the absorption of chemical species and transformation of surface chemistry of the copper deposits.

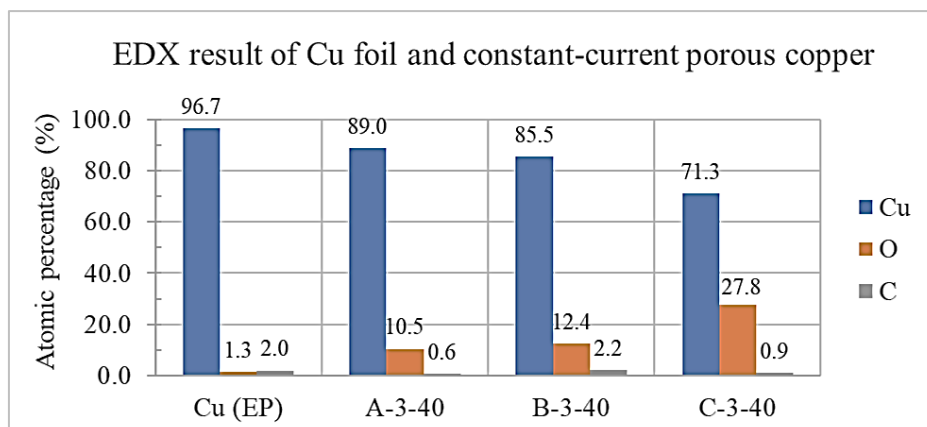


Figure 51 EDX result of Cu foil and constant-current porous copper.

Moreover, the surface composition, analyzed by XPS, of copper foil and porous coppers, it was found that the XPS profile of porous coppers were differentiate from copper foil. Porous copper surface has less percentage of carbon approximately 2-3 times, on the other hand, the percentage of copper and oxygen increase for porous copper compared to copper foil. Considering the oxidation state, only  $\text{Cu}^0$  and  $\text{Cu}^{2+}$  were detected on copper foil surface with the ratio 1:1 but the  $\text{Cu}^+$  was not detected on copper foil surface and on the surface of A-3-40 and B-3-40. Ratio of  $\text{Cu}^0/\text{Cu}^{2+}$  were approximately 2:1 and 2:3 for A-3-40 and B-3-40, respectively. For porous C-3-40, all state of copper ( $\text{Cu}^0$ ,  $\text{Cu}^+$ , and  $\text{Cu}^{2+}$ ) were detected on the surface with the ratio of approximately 1:1:6 for  $\text{Cu}^0$ ,  $\text{Cu}^+$ , and  $\text{Cu}^{2+}$ , respectively. The XPS spectra and ratio of oxidation state of copper foil (EP) and constant-current porous copper are illustrated in

Figure

52

and

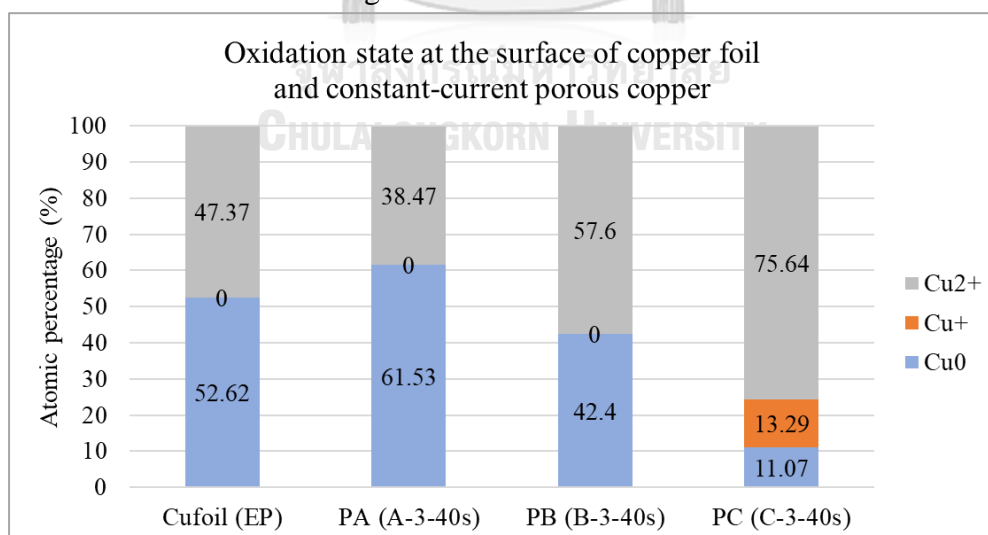


Figure 53, respectively. The oxidation state at the surface supported that composition bath of porous fabrication affect to the surface chemical composition of samples.

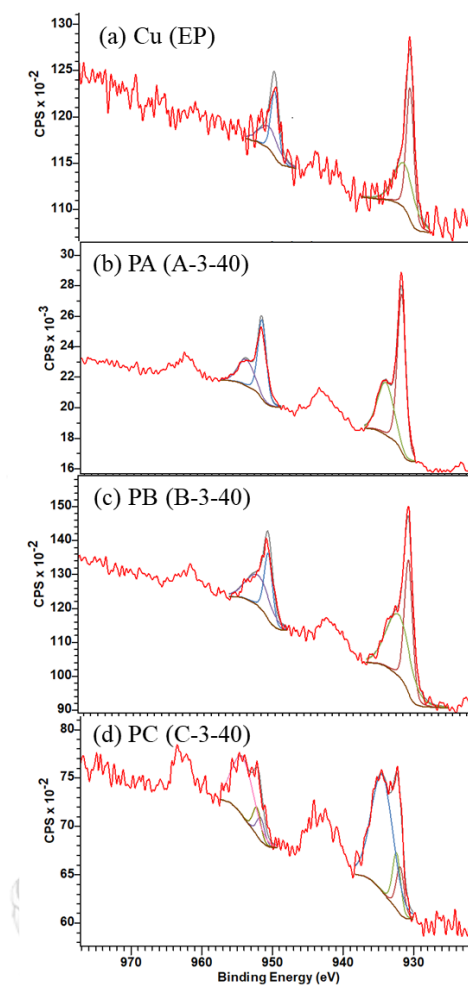


Figure 52 The XPS spectra of (a) copper foil (EP) and constant-current porous copper (b) PA (A-3-40), (c) PB (B-3-40), and (d) PC (C-3-40).

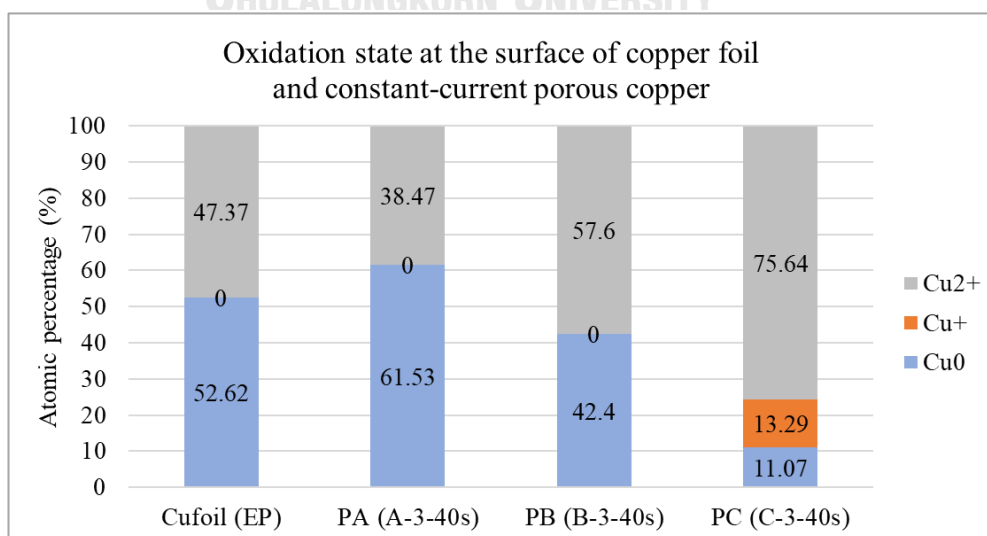


Figure 53 The ratio of oxidation state of copper foil (EP) and constant-current porous copper.



### 1.3 CO<sub>2</sub> electrochemical conversion tests (with Cu foil as baseline)

#### 1.3.1) CO<sub>2</sub>RR result of porous coppers compared with copper foil (tested at Chemical engineering, Chulalongkorn University)

Copper foil and porous coppers were passing through the CO<sub>2</sub>RR at -1.3V Ag/AgCl in 0.1 M KHCO<sub>3</sub> for 70 minutes. It can be observed that all porous coppers provided relatively high current density indicating that a faster rate of reduction reaction, as compared to the copper foil. The CO<sub>2</sub>RR products composed of those in gas and liquid forms for all porous copper electrodes under consideration. H<sub>2</sub> was the major gas product found in all testing groups, whereas CO was also detected only in the systems with porous copper electrodes. The C-3-40 electrode in particular provided relatively high amount of H<sub>2</sub> and CO, approximately 3-4 times higher than that of other porous copper groups. Moreover, whereas the copper foil electrode provided acetone, ethanol and formate, the use of electrocatalytic porous copper resulted in additional chemical products not found from the copper foil system, including acetaldehyde and acetate.

Current density of copper foil, porous A-3-40, B-3-40, and C-3-40 were -0.62, -4.11, -4.74, and -4.4 A/cm<sup>2</sup>. The constant-current porous coppers contributed approximately 7 times higher than of copper foil. The B-3-40 electrode, specifically, provided the highest reduction current density, and gave both acetaldehyde and acetate, and relatively high selectivity of ethanol compared to other porous copper electrodes. The A-3-40 electrode also yielded comparatively high selectivity of ethanol, but acetaldehyde was not detected from this system. The C-3-40 electrode, on the other hand, is unique in its relatively high production rate of formate, compared to the other sample groups. According to the mechanism pathway, H<sub>2</sub>, CO, acetaldehyde, acetate, acetone, ethanol, and formate formation require 2, 2, 10, 8, 16, 12, and 2 electron transfer, respectively. Generally, ethylene should be detected as product because it is formed by the same pathway with ethanol. CO should also be detected by copper foil because it is an elemental product requiring only 2 electron transfer. It is general product produced by copper foil. Moreover, H<sub>2</sub> and formate are also the main products produced by the copper-based electrode with 2 electron transfer requiring, therefore, they should be detected with the higher amount than the obtained result. There was also some error from the glue which used to cover getting the real active area of tested electrode, therefore, the CO<sub>2</sub>RR result show that acetone was also detected by copper foil and all kinds of porous copper. The NMR peak of the detected product and the CO<sub>2</sub>RR result of copper foil and porous coppers are shown in Figure 54, respectively.

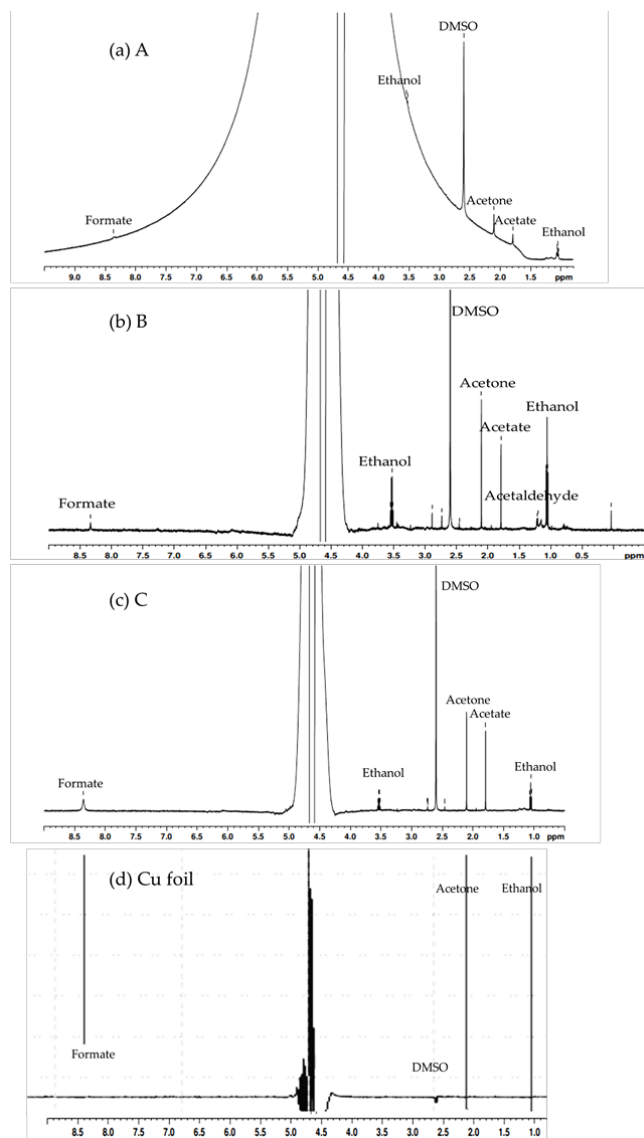


Figure 54 Representative NMR spectra obtained from the CO<sub>2</sub>RR experiments, using porous copper samples from groups (a) A, (b) B, and (c) C, electrodeposited with 3 A/cm<sup>2</sup> for 40 s, and (d) the copper foil as electrodes.

The rate of production of the chemical products of CO<sub>2</sub>RR, selectivity of the chemical products of CO<sub>2</sub>RR, and faradaic efficiency of the chemical products of CO<sub>2</sub>RR obtained from copper foil and porous A-3-40, B-3-40, and C-3-40, electrodeposited with 3 A/cm<sup>2</sup> for 40 seconds were presented in Figure 55, Figure 56, and Figure 57, respectively. The faradaic efficiency is a percentage of the ratio of output charge and input charge as calculated by the equation (7). The  $n$  is the number of mol of product,  $z$  is the number of electron transfer,  $F$  is the faradaic constant (96485 C/mol),  $I$  is input current (A), and  $t$  is the reaction time (s).

$$\% \text{ Faradaic efficiency} = \frac{nzF}{It} \quad (7)$$

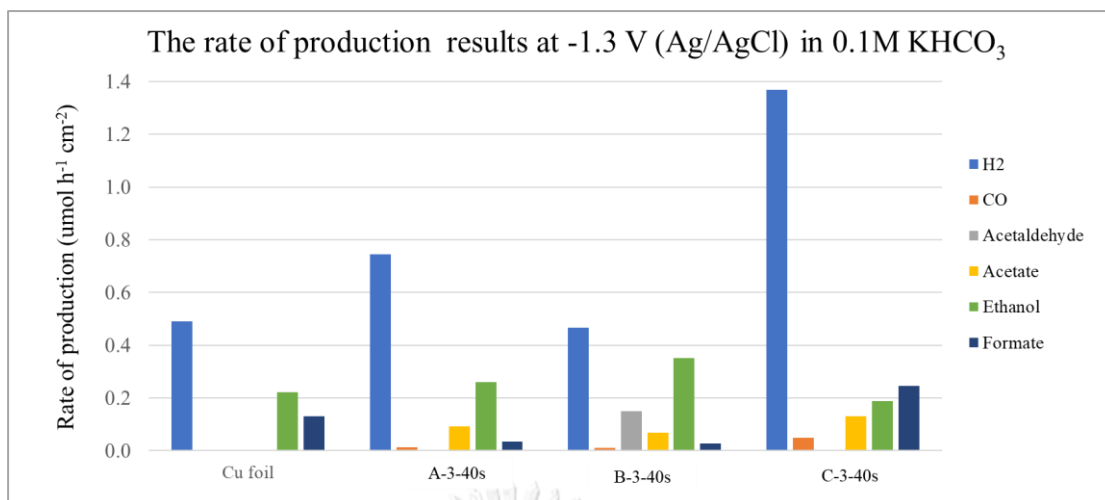


Figure 55 Rate of production of the chemical products of CO<sub>2</sub>RR obtained from Cu foil and porous A-3-40, B-3-40, and C-3-40, electrodeposited with 3 A/cm<sup>2</sup> for 40 seconds.

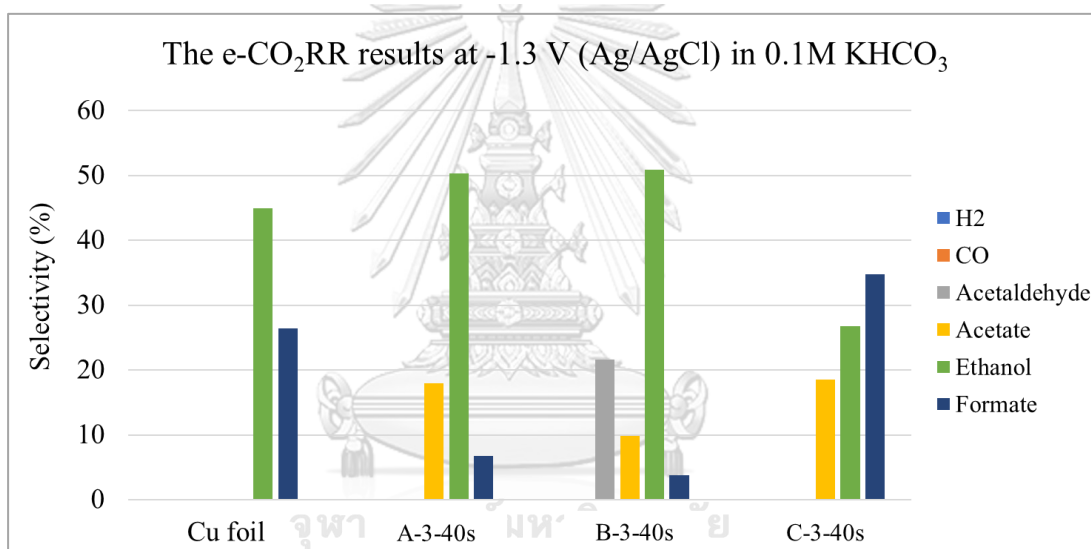


Figure 56 Selectivity of the chemical products of CO<sub>2</sub>RR obtained from Cu foil and porous A-3-40, B-3-40, and C-3-40, electrodeposited with 3 A/cm<sup>2</sup> for 40 seconds.

Microstructure of PX, PX1301, and PX1601 represents the porous coppers before passing through the CO<sub>2</sub>RR, after passing through the CO<sub>2</sub>RR at -1.3V (Ag/AgCl), and at -1.6V (Ag/AgCl), respectively, are shown in Figure 58. PX1601 was only captured for the structure comparison not for chemical composition analysis. It obvious that there is slight change in porous structure for A-3-40 and B-3-40. Their structure seems smoother than before passing through the CO<sub>2</sub>RR. Some copper particles agglomerate together into a larger particle. On the other hand, the structure of C-3-40 significantly changes from the coral-shaped into circular particles agglomeration of copper after passing through the CO<sub>2</sub>RR at -1.3 V (Ag/AgCl). Moreover, the cubic particles agglomeration of copper after passing through the CO<sub>2</sub>RR at -1.6 V (Ag/AgCl). It can indicate that the CO<sub>2</sub>RR affect to the surface structure of porous copper.

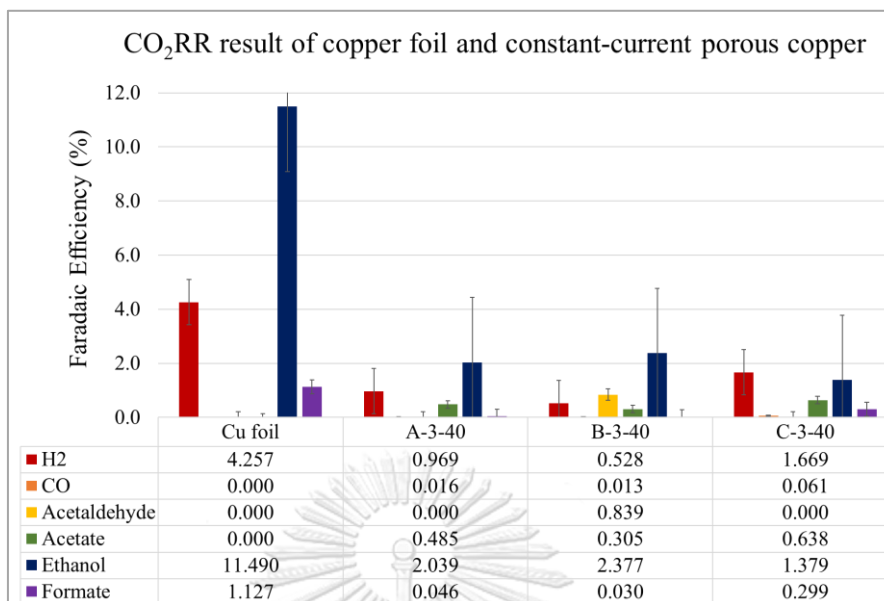


Figure 57 Faradaic efficiency of the chemical products of CO<sub>2</sub>RR obtained from Cu foil and porous A-3-40, B-3-40, and C-3-40, electrodeposited with 3 A/cm<sup>2</sup> for 40 seconds.

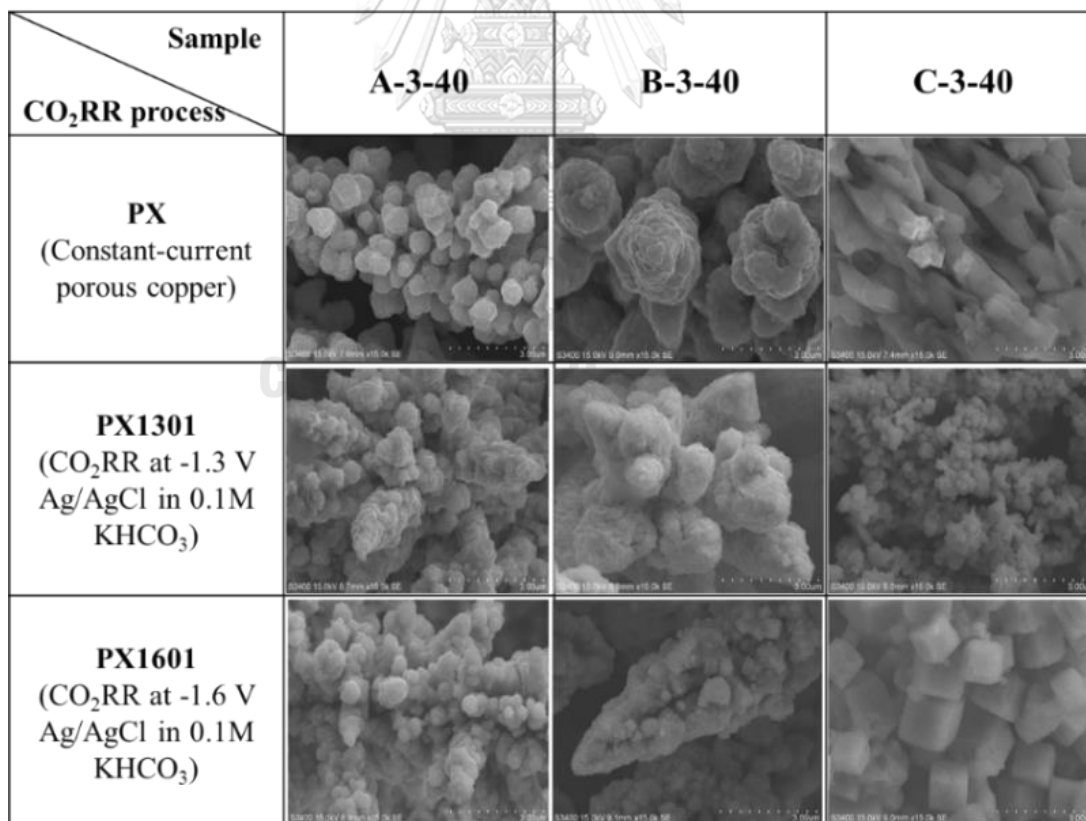


Figure 58 Microstructure of PX, PX1301, and PX1601 represents the porous coppers before passing through the CO<sub>2</sub>RR, after passing through the CO<sub>2</sub>RR at -1.3 V (Ag/AgCl), and at -1.6V (Ag/AgCl), respectively.

Apparent pore size and apparent porosity of A-3-40, B-3-40, and C-3-40 slightly increase after passing through the CO<sub>2</sub>RR as presented in Figure 59. Size in pore of C-3-40 was much higher increase than of the other porous coppers but change in porosity of C-3-40 was less than of the other porous coppers.

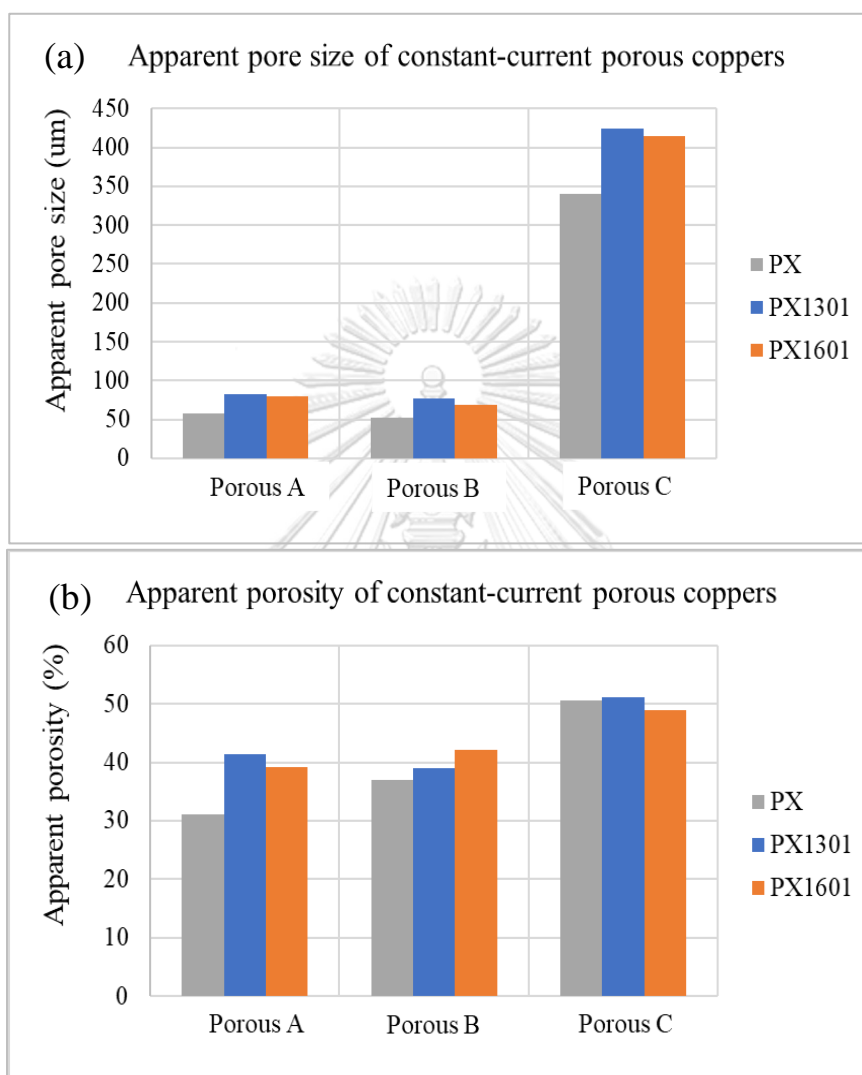


Figure 59 (a) Apparent pore size and (b) apparent porosity of constant-current porous coppers.

From EDX result as shown in Figure 60, considering chemical composition of copper foil and the constant-current porous coppers, percentage of copper content of porous copper was less than of all copper foil. Percentage of copper content of porous A, B and C (A-3-40, B-3-40, and C-3-40) are 89.49, 87.19, and 71.96, respectively. Pore size of C-3-40 was much larger than porous A and B that correspond to the lower percentage of copper content.

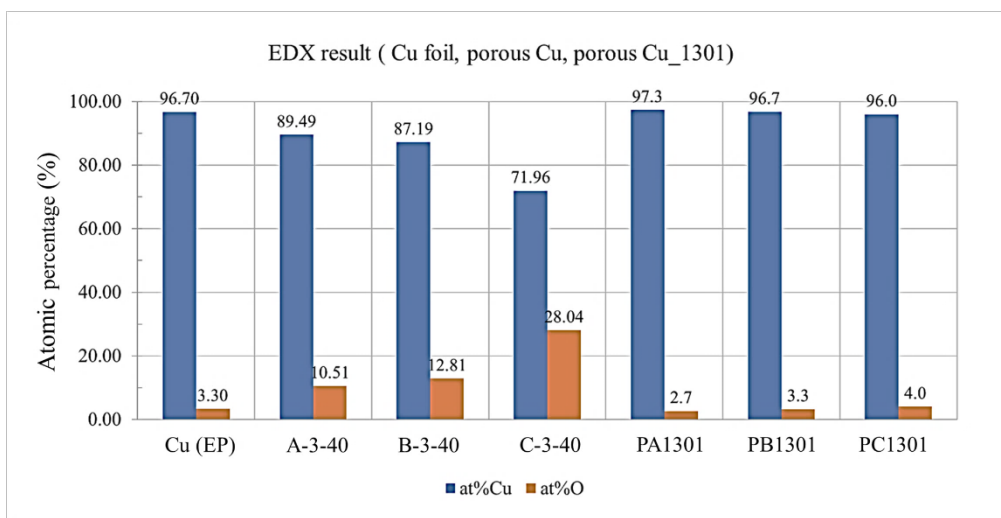


Figure 60 EDX result of copper foil and constant-current porous coppers before and after passing through CO<sub>2</sub>RR.

After passing through CO<sub>2</sub>RR, the percentage of oxygen of bulk composition of porous coppers decrease, especially C-3-40, due to reduction at working electrode. Figure 61 shows XPS profiles of the porous copper electrodes obtained after the CO<sub>2</sub>RR test sessions. The results indicate that the Cu<sup>+</sup> was detected on the surface of PA1301 and PB1301, but it was not detected on A-3-40 and B-3-40 (before passing through the CO<sub>2</sub>RR). The Cu<sup>0</sup> and Cu<sup>2+</sup> still also detected on their surface. Some copper ion was reduced at the cathode, therefore, Cu<sup>+</sup> appeared after passing through the CO<sub>2</sub>RR process. On the other hand, all of copper state (Cu<sup>0</sup>, Cu<sup>+</sup>, and Cu<sup>2+</sup>) were detected on the surface of PC1301 as similar to porous C-3-40 (Figure 62).

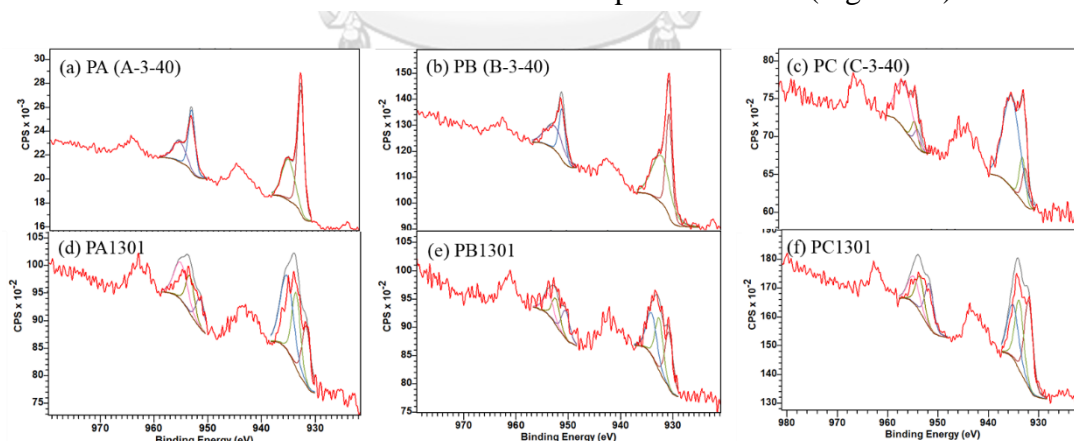


Figure 61 The XPS spectra of the constant-current porous copper before passing through CO<sub>2</sub>RR (a) PA (A-3-40), (b) PB (B-3-40), (c) PC (C-3-40), and after passing through CO<sub>2</sub>RR at -1.3 V (Ag/AgCl) in 0.1M KHCO<sub>3</sub> (d) PA1301, (e) PB1301, and (f) PC1301.

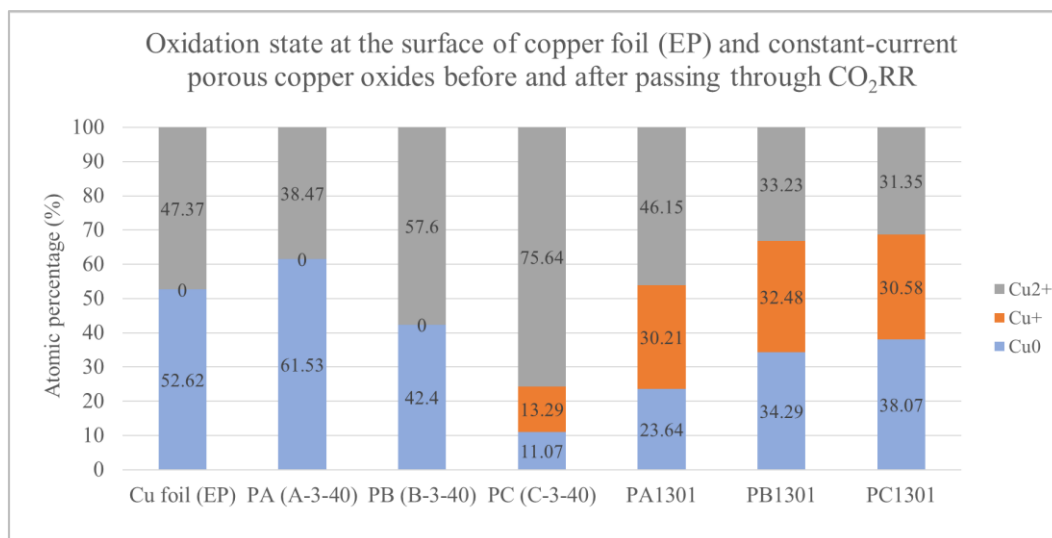


Figure 62 The ratio of oxidation state of copper foil (EP) and the constant-current porous copper before and after passing through at -1.3 V (Ag/AgCl) in 0.1M KHCO<sub>3</sub>.

1.3.2) CO<sub>2</sub>RR result of porous B-3-40 compared with copper foil (tested at National Nanotechnology Center (NANOTEC), NSTDA)

1.3.2.1) CO<sub>2</sub> electrochemical conversion result

Since, the B-3-40 provide the most product distribution compared to other two porous copper electrodes, therefore, B-3-40 was selected to study the effect of the applied voltage on the product distribution by varying the applied voltage at -1.3, 1.8, and 2.3 V Ag/AgCl in 0.1 M KHCO<sub>3</sub> for 70 minutes. PB1301, PB1801, and PB2301 were named herein to simplify the name of B-3-40 electrodes, which run at -1.3, -1.8, and -2.3 V Ag/AgCl. This experiment did at National Nanotechnology Center (NANOTEC), NSTDA. Some setup is not same as the laboratory at Chemical Engineer, Chulalongkorn University. There are some methods of sample preparation before testing CO<sub>2</sub>RR. For example, cyclic voltammetry in Ar and in CO<sub>2</sub> were required to examine the peak of CO<sub>2</sub> and acquire the proper voltage range for testing CO<sub>2</sub>RR. Chronoamperometry technique (CA), which run at constant applied voltage, was performed to test the CO<sub>2</sub>RR. The correlation between current (A) and time (s) of Cu1301, PB1301, PB1801, and PB2301 are plotted as illustrated in Figure 63. It was found that the current slightly decrease with the increasing reaction time, especially copper foil. Current of PB1301 seems more stable than of others. For PB1801, there are some errors due to leaking during CO<sub>2</sub>RR test, which can be noticed by its CA graph. Current density of copper foil, PB1301, PB1801, and PB2301 were -2.34, -5.07, -7.23, and -22.23 A/cm<sup>2</sup>, respectively. It could imply that current density increases as increase of applied voltage and physical property of electrocatalyst.

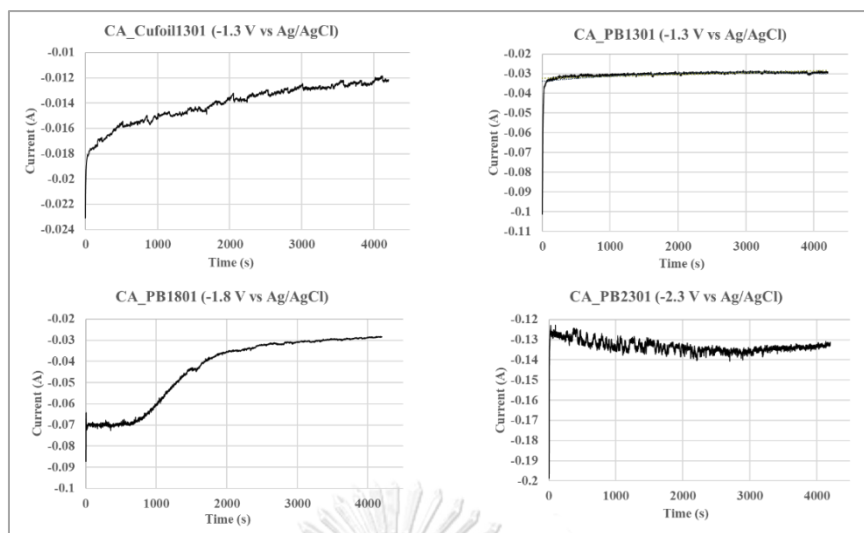


Figure 63 The correlation between current (A) and time (s) of Cu1301, PB1301, PB1801, and PB2301 during CO<sub>2</sub>RR.

Since, CO<sub>2</sub>RR products were generally produced at the cathode by reduction reaction, therefore, all liquid products should only be in the catholytic part. On the other hand, in anolytic part, oxygen gas was produced at the anode by oxidation reaction. However, due to the limitation of the Proton-exchange membrane (PEM), it was found that there were some products (i.e., formate and some alcohols) in the anolytic part. Therefore, NMR analysis were performed both catholytic and anolytic parts to collect all of products. The NMR peaks of copper foil and PB1301 are shown in Figure 64.



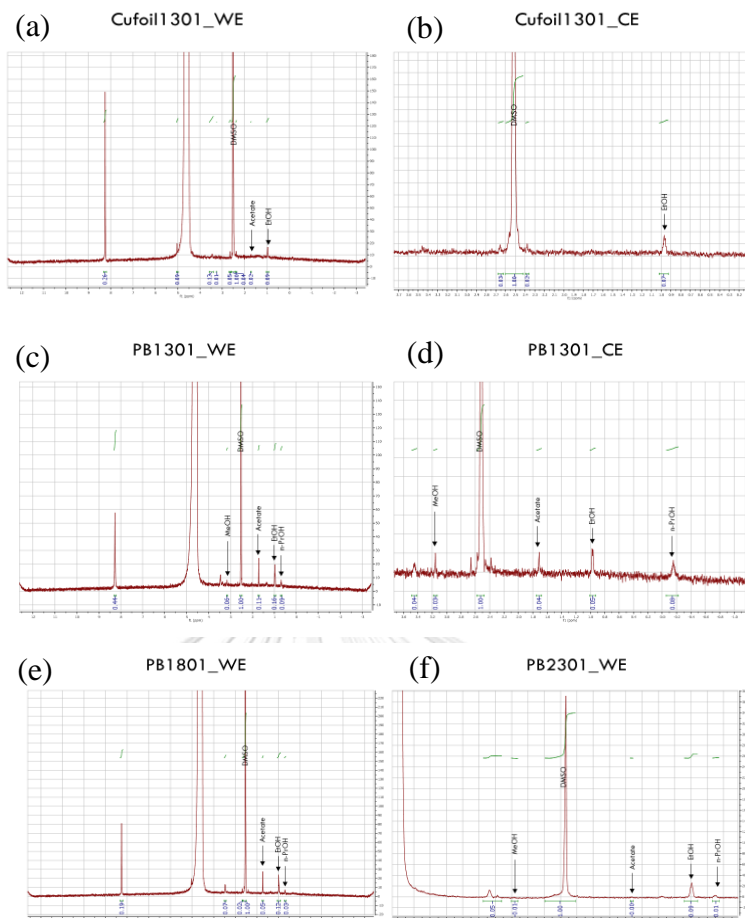


Figure 64 Representative NMR spectra obtained from the CO<sub>2</sub>RR experiments, using Cu foil in (a) catholytic and (b) anolytic parts, using B-3-40 running CO<sub>2</sub>RR at -1.3V (Ag/AgCl) in (c) catholytic and (d) anolytic parts, running CO<sub>2</sub>RR at -1.8V (Ag/AgCl) in (e) catholytic part, and running CO<sub>2</sub>RR at -2.3V (Ag/AgCl) in (f) catholytic part.

The product distribution of all electrodes herein is shown in Figure 65. It was found that current density of copper foil, PB1301, PB1801, and PB2301 were -2.34, -5.07, -7.23, and -22.23 A/cm<sup>2</sup>, respectively. The rate of reaction of porous B which run at any applied voltage was higher than of copper foil, especially for PB2301 indicating that current density increases with increase in applied voltage. In case of product distribution, H<sub>2</sub> is the major gas product for all electrodes, especially PB2301 (due to high-applied voltage). H<sub>2</sub> detected by PB1801 should be higher than of PB and PB1301 because of the higher applied voltage but the result show that less H<sub>2</sub> was detected by PB1801 due to the error during PB1801 experiment. CO was also detected as a gas product. Formate is the main liquid product for copper foil electrode whereas ethanol is the main liquid product for porous coppers. Excepting ethanol, propanol, formate, acetate, and methanol were also detected for porous coppers. Formate was detected by B-3-40 but it decreases with increasing applied voltage. Methanol was detected for only PB1301 and PB2301, but not for copper foil.

However, there probably have some errors for PB1801 because the flat cell was leak during CO<sub>2</sub>RR test as mentioned. Moreover, the faradaic efficiency summation of all products was not equal 100% designating that there probably has some products, which cannot be detected in this experiment (i.e., acetaldehyde and acetone). However, from the result, it can conclude that porous copper provides higher current density and more product distribution than of copper foil. Too high-applied voltage will cause a lot of hydrogen gas, which reduce the required CO<sub>2</sub> products.

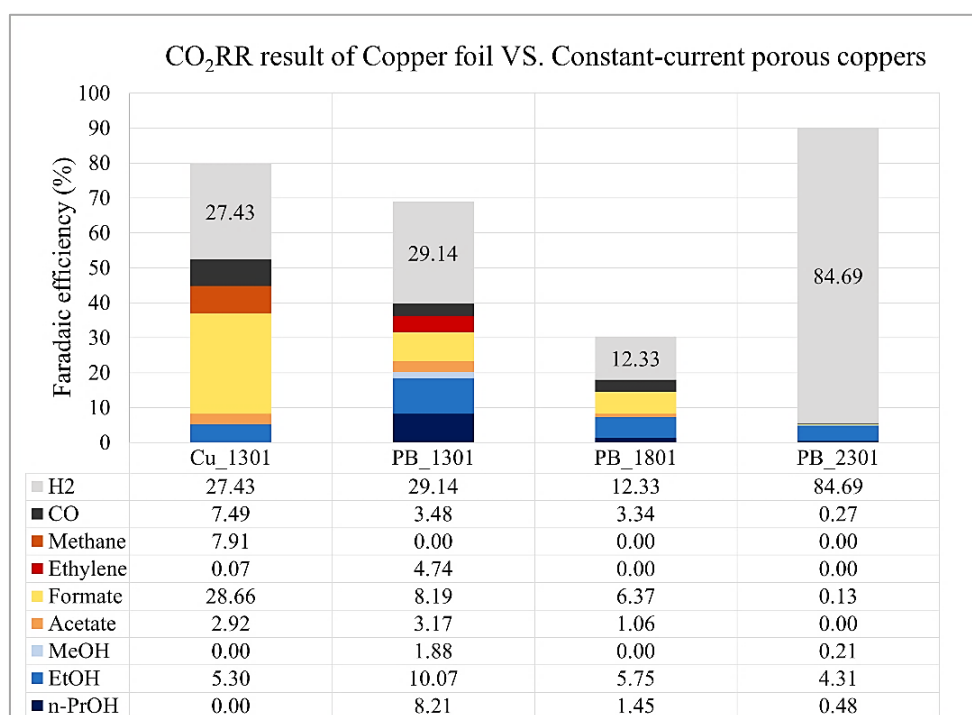


Figure 65 CO<sub>2</sub>RR result of copper foil and constant-current porous coppers.

According to the CO<sub>2</sub>RR result of Palmore's work as shown in Figure 66. His work focused on the porous coppers which deposited for 15 seconds at -1.1V (Ag/AgCl) because this is a condition which can provide the most product distribution. Formate, CO, and H<sub>2</sub> were detected as the major products whereas CH<sub>4</sub>, C<sub>2</sub>H<sub>4</sub>, C<sub>2</sub>H<sub>6</sub>, C<sub>3</sub>H<sub>6</sub> were the minor products (< 2%). Ethanol and methanol were very small products ( $\leq 1\%$ ). For C<sub>2</sub>H<sub>6</sub>, C<sub>3</sub>H<sub>6</sub>, they were detected by porous copper but not by the smooth copper. Faradaic efficiency percentage of formate of porous copper was more than of the smooth copper.

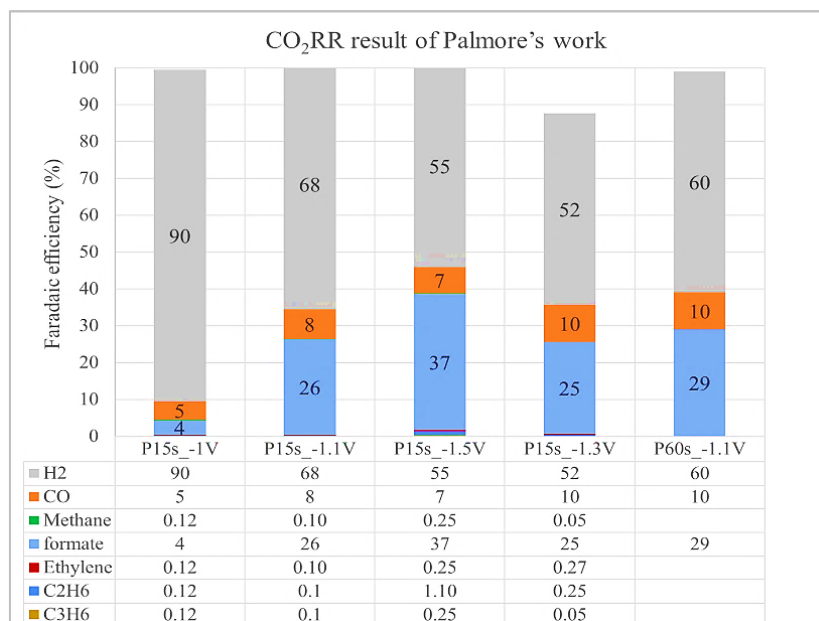


Figure 66 CO<sub>2</sub>RR result of Palmore's work.

Comparison of the CO<sub>2</sub>RR result between this work and the Palmore's work is tabulated in the Table 20. Ethanol was detected as a major product of the fabricated porous B but C<sub>2</sub>H<sub>6</sub> and C<sub>3</sub>H<sub>6</sub> were not detected by porous B due to no reference of them at Nanotec. However, this work fabricated the porous B for 40 seconds but only 15 seconds for Palmore's work. Moreover, porous B was tested in CO<sub>2</sub>RR process at -1.3V (Ag/AgCl) but Palmore's work focused on at -1.1V (Ag/AgCl).

Table 20 Comparison of the CO<sub>2</sub>RR result between this work and the Palmore's work.

Different Topic	Palmore's work	This work
Deposition time of porous fabrication	15 s	40 s
Deposition current density	> 0.5 A/cm <sup>2</sup>	3 A/cm <sup>2</sup>
Electrolyte concentration	Copper salt (contains CuSO <sub>4</sub> )	0.4M CuSO <sub>4</sub> + 1.5M H <sub>2</sub> SO <sub>4</sub>
Potential of CO <sub>2</sub> RR test	-1.1 V (Ag/AgCl)	-1.3 V (Ag/AgCl)
Major product	HCOOH CO H <sub>2</sub>	8.19% HCOOH 3.48% CO 29.14% H <sub>2</sub> 4.74% Ethylene (C <sub>2</sub> H <sub>4</sub> ) at -1.3V 10.07% EtOH at -1.3V 8.21% n-PrOH at -1.3V 3.17% Acetate at -1.3V
Minor product (< 2%)	Methane (CH <sub>4</sub> ) Ethylene (C <sub>2</sub> H <sub>4</sub> ) Ethane (C <sub>2</sub> H <sub>6</sub> ) Propylene (C <sub>3</sub> H <sub>6</sub> )	1.88% MeOH at -1.3V
Very small product (≤ 1%)	EtOH MeOH	-
Compared to smooth Cu foil	Ethane (C <sub>2</sub> H <sub>6</sub> ) and Propylene (C <sub>3</sub> H <sub>6</sub> ) were detected by porous Cu	- CO and HCOOH decrease - EtOH and Ethylene increase - MeOH and n-PrOH were detected by porous Cu - Methane was detected by Cu foil not by PB
Running CO <sub>2</sub> RR at higher potential	HCOOH increase	%FE of all products decrease when running at higher potential by PB (-1.8V, 2.3V)
Running CO <sub>2</sub> RR with 60s deposited porous Cu	HCOOH increase (Compared to 15s deposited porous Cu)	*MeOH, EtOH, n-PrOH, and Acetate were detected by PB * n-PrOH, and Acetate were not detected in Palmore's work

Furthermore, SEM images of porous B before and after passing through CO<sub>2</sub>RR are shown in Figure 67. It seems that porous B after passing the CO<sub>2</sub>RR become more cube-shaped copper particles. The copper particles split to the small groups.

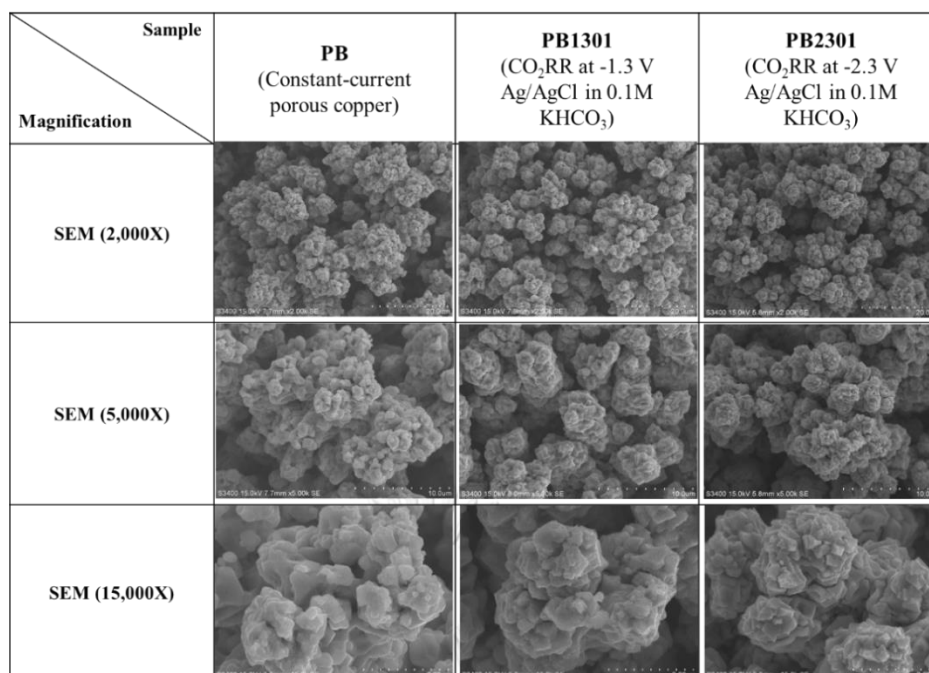


Figure 67 SEM images of porous B-3-40 before and after passing through CO<sub>2</sub>RR with magnification 2000X, 5000X, and 15,000X.

According to Figure 68, it was found that the bulk chemical composition of porous B after passing through the CO<sub>2</sub>RR was similar to the chemical composition of copper foil. More percentage of copper increase but percentage of oxygen decrease compared to PB due to the reduction reaction during CO<sub>2</sub>RR.

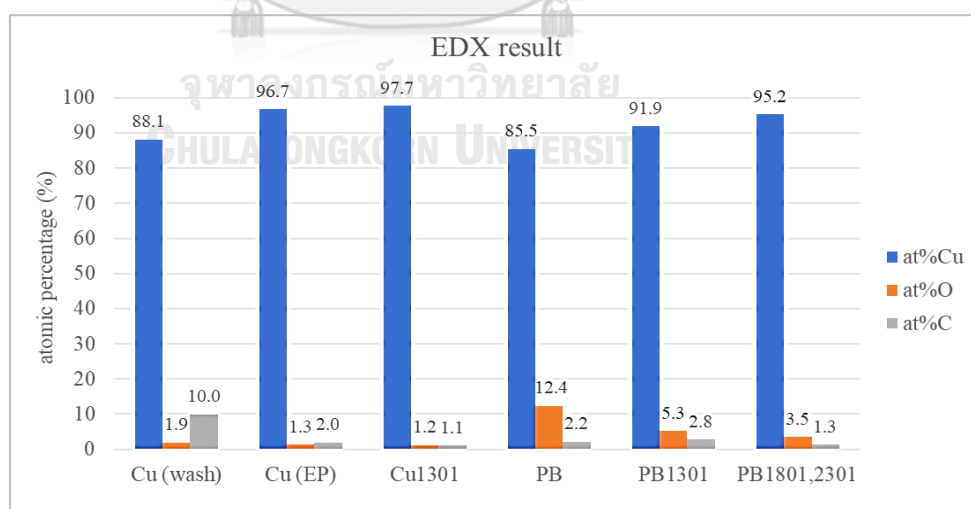


Figure 68 EDX result of Cu foil and porous B-3-40 before and after passing through at -1.3 V (Ag/AgCl) in 0.1M KHCO<sub>3</sub>. tested at Nanotec, NSTDA.

Oxidation state of porous B-3-40 was similar to copper foil both before and after passing through CO<sub>2</sub>RR. Only Cu<sup>0</sup>, and Cu<sup>2+</sup> were detected with identical ratio. Moreover, the surface chemical composition of porous B after passing through the CO<sub>2</sub>RR (Figure 69 and Figure 70) either at -1.3 V (Ag/AgCl) and -2.3 (Ag/AgCl) in 0.1 M KHCO<sub>3</sub> consisting of Cu<sup>0</sup>, Cu<sup>+</sup>, and Cu<sup>2+</sup>. It indicates that there is change in the oxidation state of copper ion at the surface due to the appearance of Cu<sup>+</sup>. Moreover, this result also correlates with the porous copper which tested at Chemical engineering, Chulalongkorn.

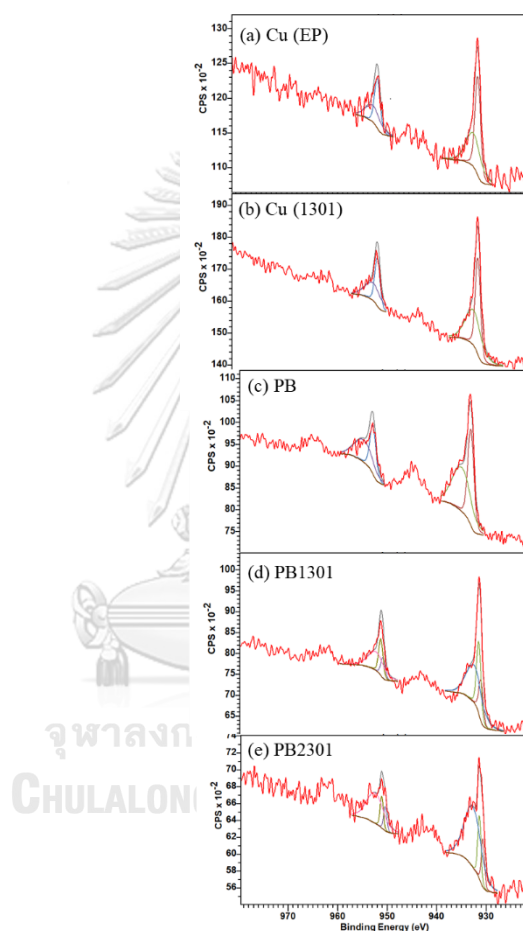


Figure 69 The XPS spectra of the copper foil and the constant-current porous copper before passing through CO<sub>2</sub>RR (a) Cu (EP), (c) PB (B-3-40) and after passing through CO<sub>2</sub>RR: (b) Cu (1301), (d) PB1301 at -1.3 V (Ag/AgCl) and (e) PB2301 at -2.3 (Ag/AgCl) in 0.1M KHCO<sub>3</sub>, respectively.

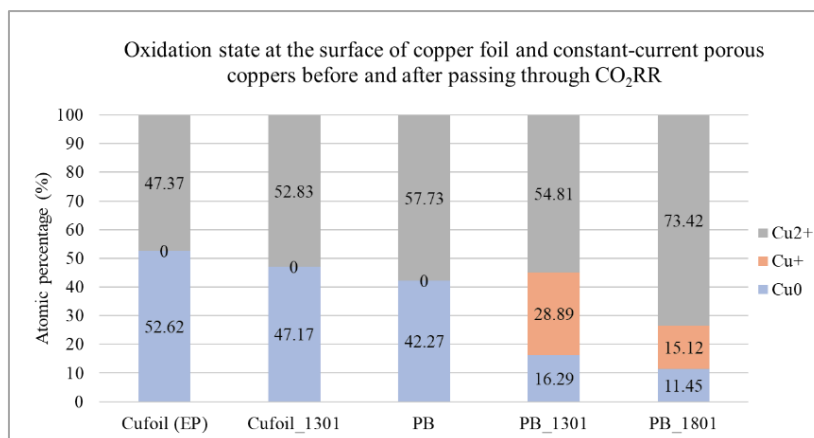


Figure 70 The ratio of the copper foil and the constant-current porous copper before passing through CO<sub>2</sub>RR (a) Cu (EP), (c) PB (B-3-40) and after passing through CO<sub>2</sub>RR: (b) Cu (1301), (d) PB1301 at -1.3 V (Ag/AgCl) and (e) PB2301 at -2.3 (Ag/AgCl) in 0.1M KHCO<sub>3</sub>, respectively.

### 1.3.2.2) Electrical test and capacitance of porous copper

Capacitance of electrode was also measured by the electrical mean. Capacitance is the capability of an electrode to store electric charge, which can be measured by change in charge in response to potential difference. This work measured the capacitance of electrodes by considering the relationship between current density (A/cm<sup>2</sup>) and scan rate (V/s). Therefore, the capacitance per area was obtained as presented in Figure 71. From the experiment, it was found that the capacitance of porous B was 20  $\mu\text{F}/\text{cm}^2$  which acquired from the gradient of the graph. The capacitance represents as the true electrical surface area of porous copper sample. Generally, capacitance of copper foil is in the range of 10-20  $\mu\text{F}/\text{cm}^2$ . Therefore, it indicates that porous B has approximately twice capacitance than of copper foil. While, both capacitance measurement and BET analysis can be used to measure the total surface area of the electrode, both techniques use different probing molecules. In capacitance measurement, ions are adsorbed on the surface in a similar conditions to the electrochemical measurement; on the other hand, in BET analysis, N<sub>2</sub> gas is employed to form a monolayer absorbed on the surface of sample, which could lead to surface area overestimation. Additionally, it is difficult to convert BET surface area to true surface area per geometrical surface area of a thin film electrode. Therefore, it is suggested that capacitance measurement should also be conducted in the future.



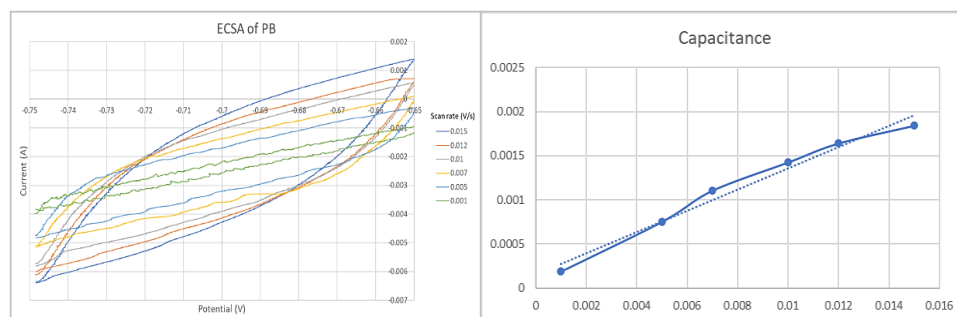


Figure 71 The capacitance of porous B-3-40.

#### 1.4 Analysis

From the results presented above, it is evidenced that the deposition of DHBT porous copper influences both the electrochemical reduction rate of  $\text{CO}_2$  and selectivity of species of chemical products developed from  $\text{CO}_2\text{RR}$  process. These improvements may stem from various factors related to the intricate structures of the porous copper electrodes, as follows: (i) porous structures appear to promote the absorption of chemical species, including oxygen as noted previously. As demonstrated by Dutta et al.[71], Lv et al.[89], and Nguyen-Phan et al.[90], surface copper oxide thus form can play a role in promoting the catalytic activity, owing to the development of a large number of active sites and roughening of the surface, following reduction of the oxide phase over the course of  $\text{CO}_2\text{RR}$ . Furthermore, the XPS analysis (Figure 52) signifies that porous copper electrodes of different morphologies exhibit a variation of oxidation states of copper on the surface (i.e.,  $\text{Cu}^0$ ,  $\text{Cu}^+$ , and  $\text{Cu}^{2+}$ ). The oxidation states of copper are known to influence preferential formations of intermediates and hence affect the  $\text{CO}_2$  reduction pathways and promote selectivity [91-93]; and (ii) the intricate structure of the porous copper electrodes may enhance dynamic diffusion of the dissolved gas to provide increasing  $\text{CO}_2$  concentration at the catalytic electrode-electrolyte interface [89]. Temporal trapping of gaseous intermediates, e.g., CO, could also be induced inside the pores [71]. Furthermore, the high porosity of the porous copper provides high surface areas and hence large active sites for the electrodes. Correspondingly, the retention time for  $\text{CO}_2\text{RR}$  could be effectively enlarged. Unlike  $\text{H}_2$ , CO and formate which require minimal amounts of electron transfers (1-2 electrons) to generate, larger hydrocarbon molecules such as acetate, acetaldehyde and ethanol requires many more electron transfers (8, 10, 12 electrons, respectively) making them challenging to produce from the  $\text{CO}_2\text{RR}$  process generally. Yet, these three chemical products were detected from the systems with the porous copper electrodes investigated herein with relatively high selectivity.

Examining more closely, porous B appears to exhibit the best performance in term of the reduction rate and a variety of the chemical products, albeit the true surface area of porous B is somewhat lower than that of porous A. This result thus

underlines that surface area is not the only primary factors underlining the good performance of the electrode, but rather other influences such as surface morphology (i.e., cluster of a berry like structure of porous A vs. flower like morphology of porous B) and surface chemistry (e.g., alternation of surface chemistry by adsorbed oxygen and oxidation states) also play important roles. Further examination and analysis will thus be required to gain insights on the contribution of important factors that lead to the enhancement of electrode performance observed herein, along with understanding of the suitable applied overpotentials and other control parameters to optimally induce CO<sub>2</sub>RR for respective porous copper electrodes.

## Section 2: Thermally-induced copper oxides and CO<sub>2</sub> conversion performance

### 2.1) Copper oxide fabrication

The oxidized copper electrodes namely A300, A500, A800, and A1000 fabricated by thermal oxidation in the furnace as shown Figure 72. It was found that the surface of A300 was darker due to the oxide layer on the copper foil substrate after passing through the oxidation process. The surface of A500 was not uniform. There are some copper oxide flakes peeling off from the surface. The oxide layer adhesion was not good, therefore, A500 cannot be used as electrocatalyst in CO<sub>2</sub>RR. Both A800 and A1000 were fully oxidized copper. Thicker layer of copper oxide covering on the substrate with high adhesion. Their surfaces seem shiny gray-black color. However, they were broken, therefore, they would also not run in CO<sub>2</sub>RR. It could summarize that all samples excepting A300 were broken due to the brittleness of copper oxide. Therefore, only A300 was run in CO<sub>2</sub>RR experiment.





Sample Characteristics	A300	A500	A800	A1000
Oxidation temperature (°C)	300	500	800	1000
Oxidation time (h)	1	1	1	1
Appearance after passing thermal oxidation				

Figure 72 Appearance and 3D-morphology of A300, A500, A800, and A1000 fabricated by thermal oxidation in the furnace.

### 2.2) Sample characterization

Morphology of oxidized coppers are shown in Figure 73. A300 seems smooth, but it consists of some chunks of copper oxide on the surface. The groups of particles as a flower-like particles were obvious on the surface of A500 and A800 whereas A1000 surface seems smooth with the strips separating into many groups.

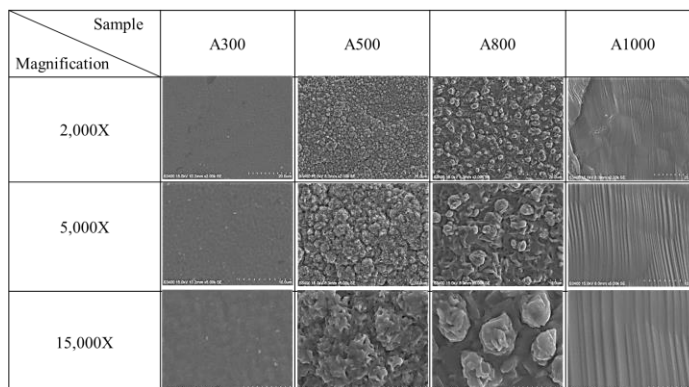


Figure 73 Morphology of oxidized coppers (A300, A500, A800, and A1000) captured at 2000X, 5000X, and 15000X.

Moreover, EDX result shows that percentage of oxygen of all oxidized copper is more than of copper foil manifestly. Especially A500, A800, and A1000, their percentage of oxygen in bulk is approximately twice as much as A300 as shown in Figure 74.

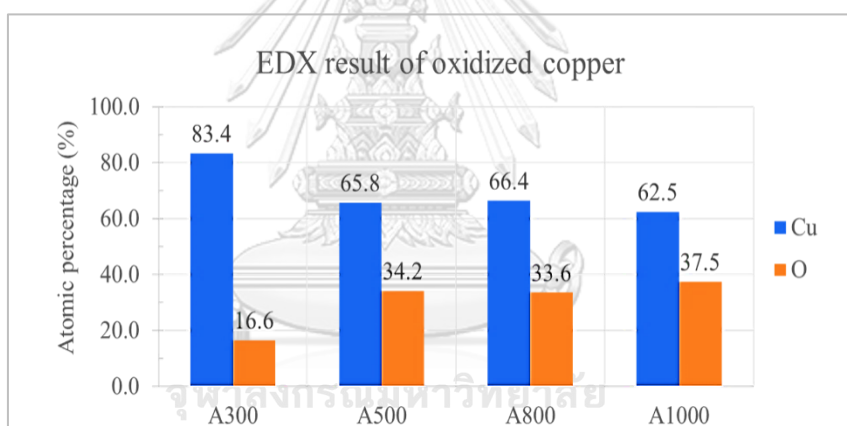


Figure 74 EDX result of oxidized copper.

According to the XRD result of Hugo's work as illustrated in Table 21, it supported that bulk composition of each fabricated oxidized copper were different.  $\text{Cu}^0$  and  $\text{Cu}^+$  were detected on A300 whereas  $\text{Cu}^+$  and  $\text{Cu}^{2+}$  were detected on A800. On the other hand, only  $\text{Cu}^{2+}$  was detected on A1000. Therefore, this work was inspired to fabricate the thermally oxidized copper for studying the relation between the surface composition and  $\text{CO}_2\text{RR}$  performance.

Table 21 the XRD result of Hugo's work.

Temperature range (°C)	Ambient	Temperature (°C)	Time (h)	Composition on Cu foil after heat treatment			Oxidation result
< 200	atm	100	1	Cu			Thin layer of Cu-oxide (main Cu <sub>2</sub> O) on Cu surface
	atm	150	1	Cu	Cu <sub>2</sub> O		
300	atm	300	1	Cu	Cu <sub>2</sub> O		Passivating oxide layer composed by CuO & Cu <sub>2</sub> O (24h)
	air flow	300	24	Cu	Cu <sub>2</sub> O	CuO	
400-700	-	-	-	-	-	-	Cu-oxide layer was fragile & poor adherence to the surface
800-900	air	800	1		Cu <sub>2</sub> O	CuO	Complete oxidation// the bulk composed by mixture of Cu <sub>2</sub> O and CuO
	air	900	1		Cu <sub>2</sub> O	CuO	
1000	air	1000	1		Cu <sub>2</sub> O	CuO	Pure and high crystal of CuO
	air	1000	3		Cu <sub>2</sub> O	CuO	
	air	1000	24			CuO	
	O <sub>2</sub>	1000	8			CuO	

The XPS spectra and the ratio of oxidation state are shown in Figure 75 and Figure 76. The percentage of carbon and oxygen of oxidized copper increase due to thermal oxidation. In case of the oxidation state, only Cu<sup>+</sup> and Cu<sup>2+</sup> were detected on the surface of A300 and A500 but all of oxidation states were detected on the surface of A800. The oxidation state of A1000 consisting of Cu<sup>0</sup> and Cu<sup>2+</sup> without Cu<sup>+</sup>. Their chemical composition of surface was different due to the effect of oxidation time.

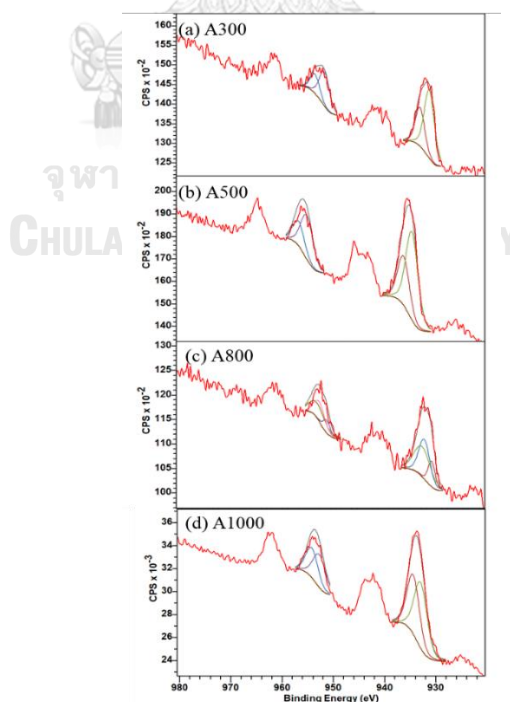


Figure 75 The XPS spectra of the thermally-induced copper oxides (a) A300, (b) A500, (c) A800, and (d) A1000.

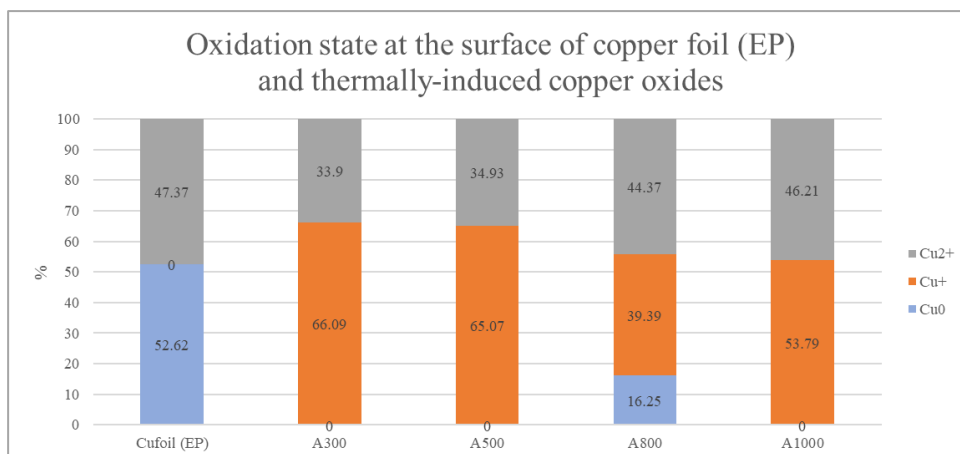


Figure 76 The oxidation state of copper foil and the thermally-induced copper oxides A300, A500, A800, and A1000.

### 2.3 CO<sub>2</sub> electrochemical conversion tests (with Cu foil as baseline)

The CO<sub>2</sub>RR result of A300 was compared with copper foil at -1.3 V (Ag/AgCl) in 0.5M KHCO<sub>3</sub> solution (

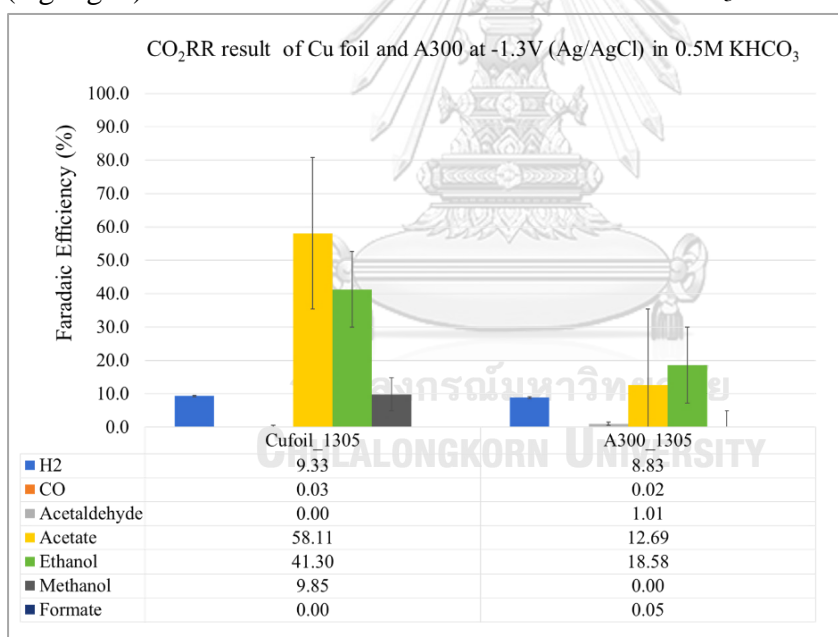


Figure 77). This experiment performed in different solution from porous coppers and oxidized porous coppers because the previous work suggested to run in 0.5M KHCO<sub>3</sub> solution. Since, this concentration is more suitable for reduction of CO<sub>2</sub> with A300. It was found that the current density of copper foil and A300 were -0.34 and -5.516 A/cm<sup>2</sup>, respectively. A300 contributed much higher rate of reaction than of copper foil approximately 16 times. For product distribution, H<sub>2</sub> and CO were detected as gas product for both copper foil and A300 but CO should be detected at higher %FE. Acetaldehyde and formate were detected only on A300 whereas methanol was detected only on copper foil. Although, the previous works suggested

that methanol has higher possibility to be detected in a copper oxide system. This suggest that there maybe errors during the gas detection process of CO<sub>2</sub>RR testing. Moreover, acetone was also detected with extremely high amount likely due to the contamination from glue or tape which was employed for sample masking. Therefore, summation of faradaic efficiency was higher than 100% which could not be possible for the percentage. As mentioned before, the setup of Chemical Engineering, Chulalongkorn University was different from Nanotec. Therefore, some results could not be reliable, but it can relate the result each other to get the trend of products. However, it could conclude that the fabricated copper oxide was not predominant for product distribution compared to copper foil, but it has high stability of the surface composition after passing through CO<sub>2</sub>RR.

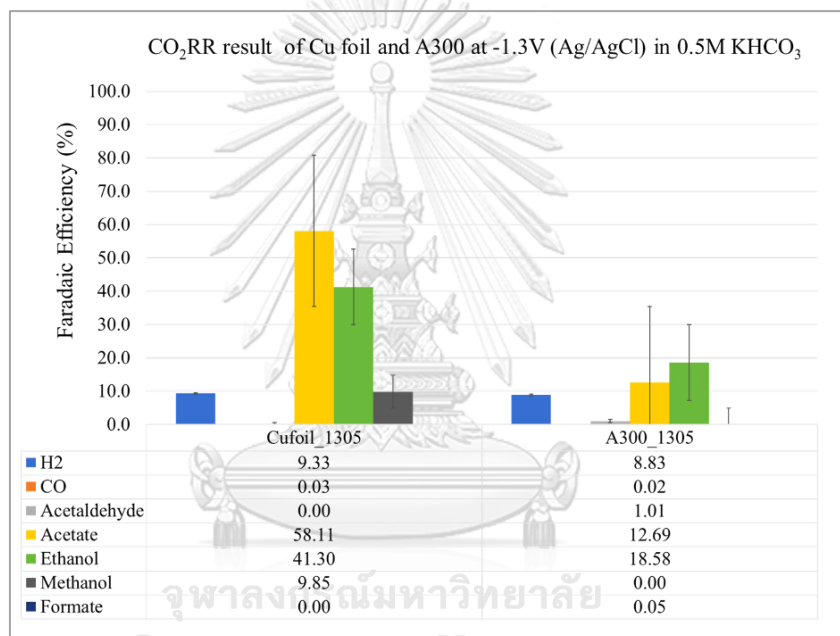


Figure 77 Faradaic efficiency of the chemical products of CO<sub>2</sub>RR obtained from Cu foil and the thermally-induced copper oxides (A300) at -1.3 V (Ag/AgCl) in 0.5 M KHCO<sub>3</sub>.

The oxidized copper was used to be a sample for studying the outcome of thermally oxidation. It was run at -1.3 V (Ag/AgCl) in 0.5 M KHCO<sub>3</sub> for 70 minutes as previous work recommendation, which different from the porous coppers and oxidized porous copper. Generally, higher concentration should promote higher rate of reaction due to higher molecule of solute in the solution. Therefore, 0.5M KHCO<sub>3</sub> electrolyte should enhance rate of reaction but the obtained current density of copper foil electrocatalyst was less than of running in 0.1 M KCHO<sub>3</sub>. It may conclude that higher concentration of this electrolyte can promote the A300 electrocatalyst performance more than of copper foil. Figure 78 illustrates the EDX result of copper foil and A300 before and after passing through CO<sub>2</sub>RR at -1.3 V (Ag/AgCl) in 0.5M KHCO<sub>3</sub>. Bulk composition after passing through the CO<sub>2</sub>RR of copper foil was



slightly changed whereas atomic percentage of oxygen of A300 was significantly reduced due to the reduction reaction at the working electrode.

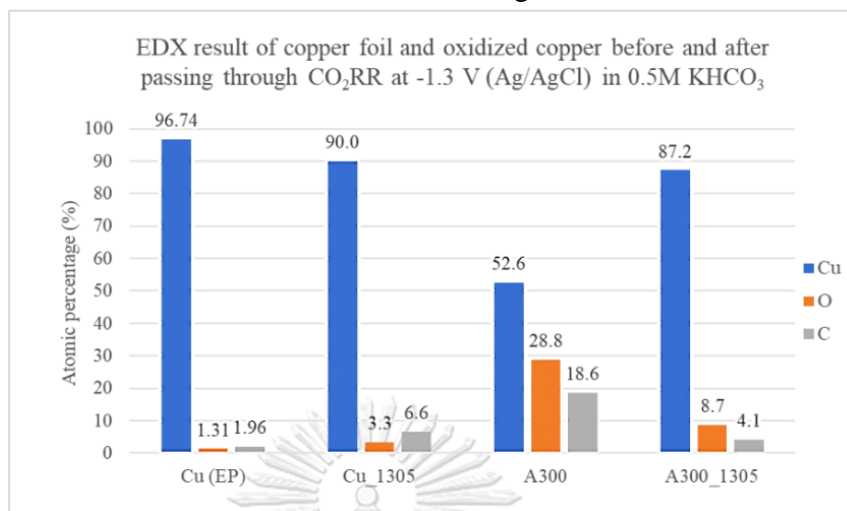


Figure 78 EDX result of copper foil and A300 before and after passing through CO<sub>2</sub>RR at -1.3 V (Ag/AgCl) in 0.5M KHCO<sub>3</sub>.

For surface chemical analysis (Figure 79. and Figure 80.), Cu<sup>0</sup> and Cu<sup>2+</sup> were detected on the surface of copper foil (EP). After CO<sub>2</sub>RR, Cu<sup>+</sup> and Cu<sup>2+</sup> were detected on the surface of copper foil. On the other hand, only Cu<sup>+</sup> and Cu<sup>2+</sup> were detected on the surface of A300, and A300\_1305. However, the ratio of Cu<sup>+</sup>/Cu<sup>2+</sup> slightly decrease after passing through the CO<sub>2</sub>RR. It implies that A300 have high surface stability compared to copper foil. For oxidized copper summation, A300 was fabricated to study in section 3 (oxidized porous copper). The other oxidized copper, A500, A800, and A1000, were much brittle to develop the electrodes. Therefore, A300 is the best condition for advancing the catalyst.

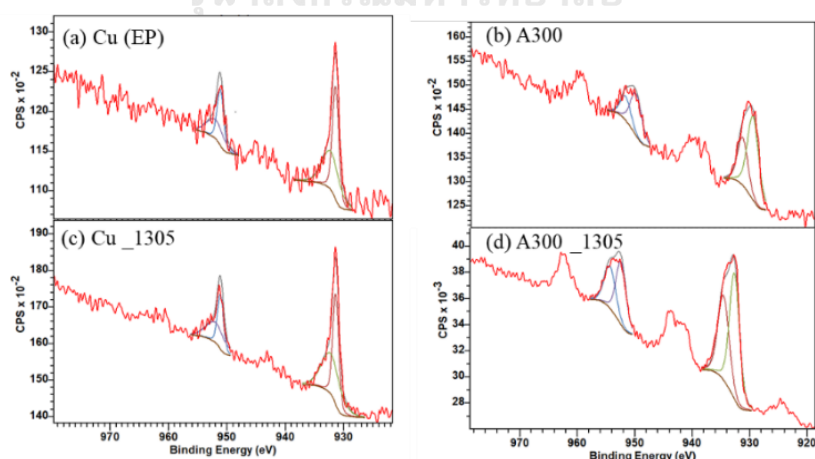


Figure 79 The XPS spectra of the copper foil and thermally-induced copper oxides before (a) Cu (EP), (b) A300 and after passing through CO<sub>2</sub>RR at -1.3 (Ag/AgCl) in 0.5M KHCO<sub>3</sub> (c) Cu\_1305, and (d) A300\_1305.



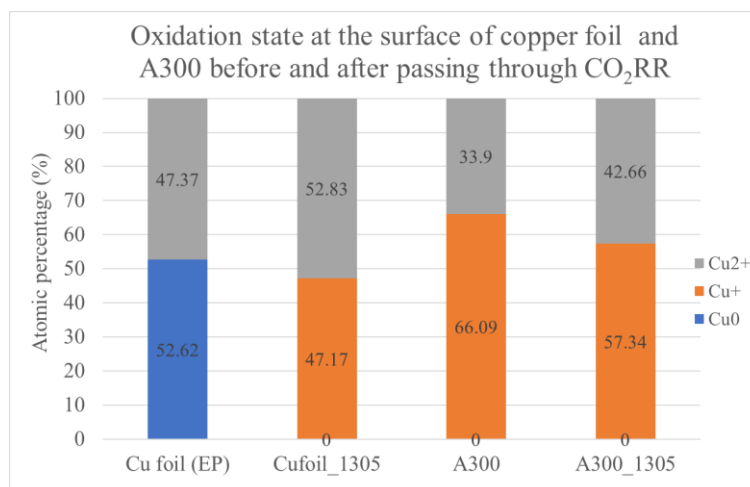


Figure 80 The ratio of oxidation state of the copper foil and thermally-induced copper oxides before (a) Cu (EP), (b) A300 and after passing through CO<sub>2</sub>RR at -1.3 (Ag/AgCl) in 0.5M KHCO<sub>3</sub> (c) Cu\_1305, and (d) A300\_1305.

## 2.4 Analysis

According to the result, copper oxide electrocatalyst could contribute different product distribution of CO<sub>2</sub>RR from copper foil (i.e., acetaldehyde and acetone) with much higher current density. Although, some errors affect the product distribution, it can indicate that copper oxide can enhance the rate of CO<sub>2</sub>RR and provide more product distribution.

## Section 3: Thermally-induced copper oxides from porous copper

### 3.1 Fabrication method

Thermally oxidized porous coppers is an amalgamation of fabricated porous copper (porous A, B, and C) and copper oxide (A300). Porous coppers were passing through the thermal oxidation at 300°C for 1 hour. Their morphology was visually similar to porous coppers, but the surface become darker than of porous coppers due to covering of oxide.

### 3.2 Sample characterization

Apparent pore size and percentage of apparent porosity of PX (Porous copper), PXA300 (pre-running CO<sub>2</sub>RR), and PXA300\_1301 (post-running CO<sub>2</sub>RR) are shown in Figure 81. The Image J result present that apparent pore size of thermally-induced porous copper oxides; PAA300 (60 μm) and PBA300 (58.9 μm) were slightly more than of porous coppers; PA (58 μm) and PB (52 μm). The apparent pore size of them is equally in the range of 50-60 μm with similar apparent percentage of porosity approximate as 30-40%.

After passing through the thermally-induced porous copper oxides in 0.1M KHCO<sub>3</sub> at -1.3 V (Ag/AgCl), diameter of pore slightly increases around 50%, in

additions, percentage of porosity also increase approximately 27.5% for PAA300 and 49.3% for PBA300. For PC, apparent pore size of PCA300 was larger than PC approximately 70%. It was found that a large cluster of particles of all thermally-induced porous copper oxides (PAA300, PBA300, and PCA300) seems to be separated from each other. Apparent pore size and apparent porosity would larger. However, OM and SEM image could illustrate the characteristic of 2D-morphology, Image J analysis result of porous C was not be clear. It might be due to the error when measuring because thermally-induced porous copper oxides of porous C (PCA300) was rather much weaker than PAA300 and PBA300.

Morphology characteristic of thermally-induced porous copper oxides and thermally-induced porous copper oxides after passing through CO<sub>2</sub>RR, were investigated by OM and SEM techniques. The result showed that particles on porous coppers agglomerated together to form a large cluster of these particles after passing through thermal oxidation as thermally-induced porous copper oxides. A lot of small particles of porous A were combine altogether, therefore, morphology change from small grains into a chunk of particles. Particles of porous B combine each other as a bunch of a lot of large polygon grains (compared to porous A). Particles of porous C seems connect between them. Copper particle of PAA300 seems as circular but copper particle of PBA300 and PCA300 appear to be cubic shaped as shown in Figure 82.

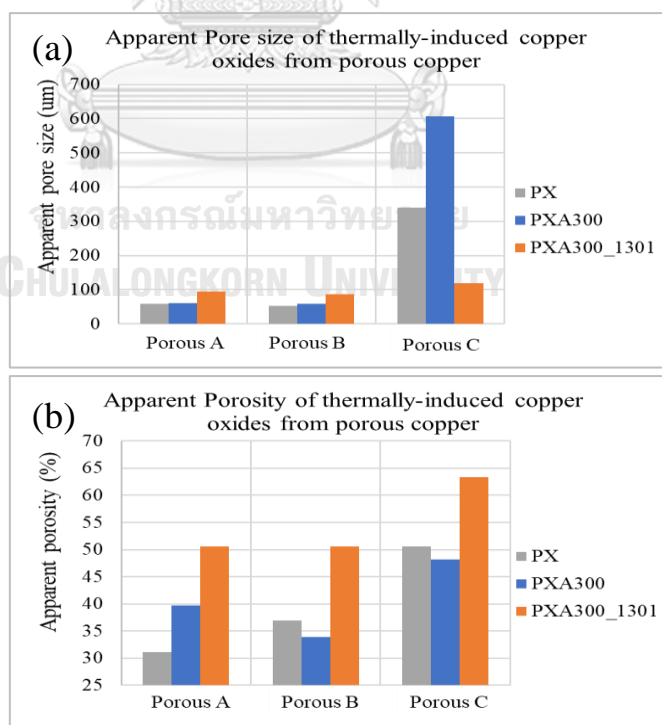


Figure 81 (a) Apparent pore size and (b) apparent porosity of constant-current porous coppers, thermally-induced porous copper oxides, and thermally-induced porous copper oxides after passing through CO<sub>2</sub>RR at -1.3V (Ag/AgCl) in 0.1M KHCO<sub>3</sub>.

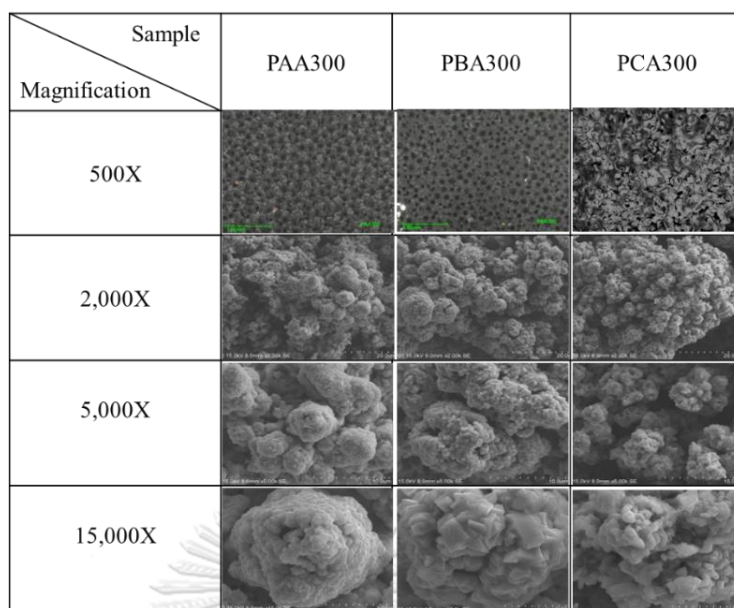


Figure 82 Morphology of thermally-induced porous copper oxides captured at 2000X, 5000X, and 15000X.

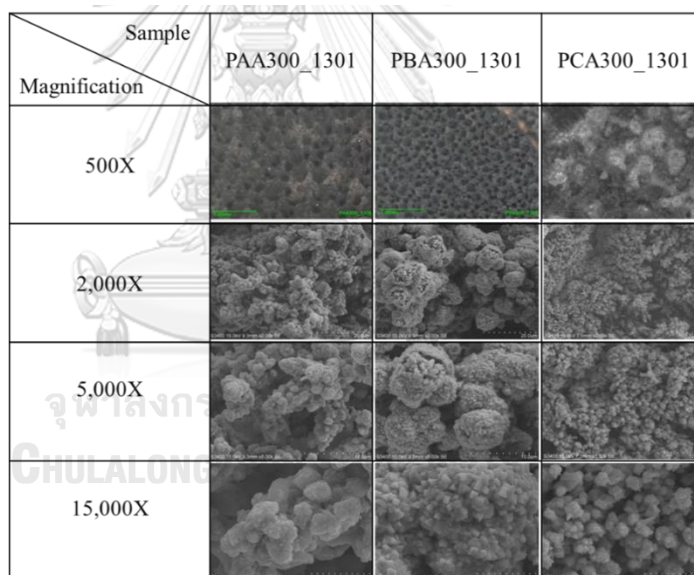


Figure 83 Morphology of thermally-induced porous copper oxides after passing through the CO<sub>2</sub>RR at -1.3 V (Ag/AgCl) in 0.1M KHCO<sub>3</sub> captured at 2000X, 5000X, and 15000X.

The surface composition of PXA300 after passing through CO<sub>2</sub>RR were not significantly change from before running as shown Figure 83. indicating that PXA300 surface is more stable than of PX. It was probably the oxide covering on the surface support to the stability. The bulk composition of PXA300, and PXA300\_1301 of PA, PB, and PC are shown in Figure 84. Oxygen percentage of PAA300 and PBA300 were higher than of PA and PB, respectively, due to thermal oxidation. Oxygen percentage of PCA300 is rather similar to PC indicating that the thermal oxidation is not significantly for oxygen content for PC. After CO<sub>2</sub>RR, oxygen percentage of PA decrease but oxygen percentage of PAA300 still equal to before CO<sub>2</sub>RR indicating

that PAA300 is more stable for being catalyst at -1.3V (Ag/AgCl) than of PA. Similarly, oxygen percentage of PB and PC decrease more than of PBA300 and PCA300, respectively, indicating that PBA300 and PCA300 were also more stable for being catalyst at -1.3V (Ag/AgCl) than of PB and PC, respectively.

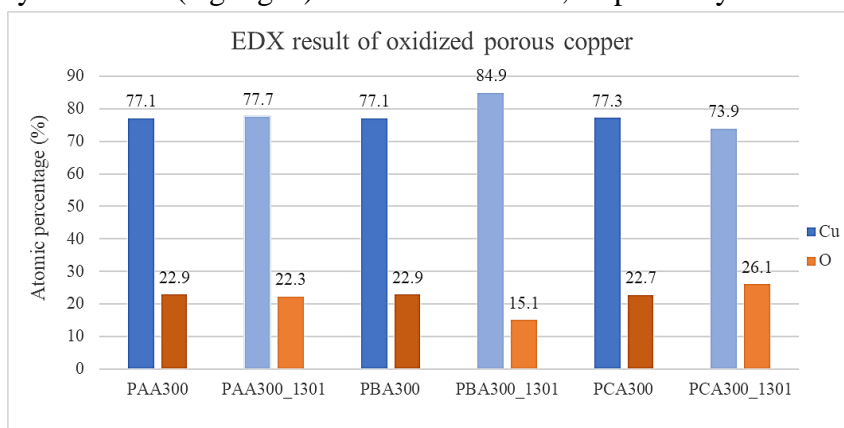


Figure 84 EDX result of thermally-induced porous copper oxides, and thermally-induced porous copper oxides after passing through CO<sub>2</sub>RR at -1.3V (Ag/AgCl) in 0.1M KHCO<sub>3</sub>.

Only Cu<sup>+</sup> and Cu<sup>2+</sup> were detected of all samples in this group both before and after passing through CO<sub>2</sub>RR as illustrated in Figure 85 and Figure 86. After running CO<sub>2</sub>RR, ratio of Cu<sup>+</sup>/Cu<sup>2+</sup> of all thermally-induced porous copper oxides increase indicating that Cu<sup>2+</sup> ion on surface of was reduced into Cu<sup>+</sup> ion during CO<sub>2</sub>RR. This ratio of PAA300, PBA300, and PCA300 increase approximately 1.75 times (from 1.15 to 2.01), times (from 0.83 to 2.8), 3.3 times (from 1.15 to 2.01), and 2.6 times (from 0.73 to 1.93), respectively. Therefore, CO<sub>2</sub>RR affect to oxidation state of Cu ion at the surface.

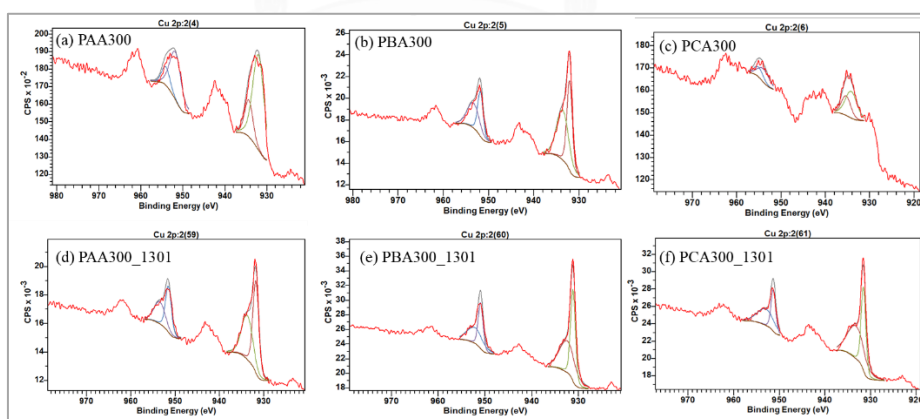


Figure 85 The XPS spectra of the constant-current porous copper before passing through CO<sub>2</sub>RR (a) PAA300, (b) PBA300, (c) PCA300 and after passing through CO<sub>2</sub>RR at -1.3 V (Ag/AgCl) in 0.1M KHCO<sub>3</sub> (d) PAA300\_1301, (e) PBA300\_1301, and (f) PCA300\_1301.

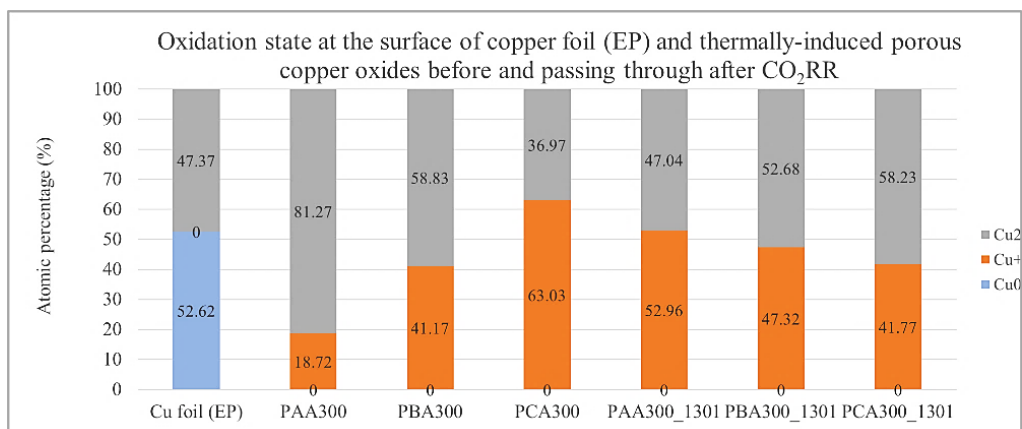


Figure 86 The ratio of the oxidation state of the constant-current porous copper before passing through CO<sub>2</sub>RR (a) PAA300, (b) PBA300, (c) PCA300 and after passing through CO<sub>2</sub>RR at -1.3 V (Ag/AgCl) in 0.1M KHCO<sub>3</sub> (d) PAA300\_1301, (e) PBA300\_1301, and (f) PCA300\_1301.

### 3.3 CO<sub>2</sub> electrochemical conversion tests

Gas products (H<sub>2</sub> and CO) were not detected on all PXA300 electrodes. The cause of CO absence may be due to the extremely high amount of input CO<sub>2</sub> reactant or/and set up of the CO<sub>2</sub>RR system. Although, the summation of faradaic efficiency of PXA300 were lower than 25% due to some errors or undetected products, it was found that PAA300 contribute the most products (i.e., acetaldehyde, acetate, ethanol, methanol, n-propanol, glycolaldehyde, and propionaldehyde). Acetaldehyde was detected only on PAA300 and PBA300 whereas methanol, n-propanol, glycolaldehyde, and propionaldehyde were detected only on PAA300. PCA300 deliver the least amount of product. Ethanol was the main product for all PXA300. Methanol can be detected on PAA300 but at a very low faradaic efficiency. These products require more than 2 electron transfer. Moreover, current density of PXA300 was approximately 8-9 mA/cm<sup>2</sup> which significantly increase compared to porous copper indicating that change in microstructure and chemical composition strongly enhance the CO<sub>2</sub>RR performance. CO<sub>2</sub>RR result of PXA300 are shown in Figure 87. Based on the CO<sub>2</sub> purging at 20 ml/min for 100 minutes (30 minutes before running CO<sub>2</sub>RR and 70 minutes during running CO<sub>2</sub>RR), total of input CO<sub>2</sub> is 3.954 grams. Total mass of all products which formed by PAA300, PBA300, and PCA300 are 0.001185, 0.000505, 0.000598 grams. Therefore, percentage of CO<sub>2</sub> conversion of PAA300, PBA300, and PCA300 are 0.0300%, 0.0128%, and 0.0151%, respectively. Moreover, the CO<sub>2</sub> solubility in the electrolyte is 35 mmol causing the total of saturated CO<sub>2</sub> in the experiment (20 ml electrolyte) is 700 μmol. Total mol of all products which formed by PAA300, PBA300, and PCA300 are 3.77, 5.02, 5.14 mol. Therefore, percentage of CO<sub>2</sub> conversion of PAA300, PBA300, and PCA300 are 0.5388%, 0.7168%, and 0.7340, respectively.



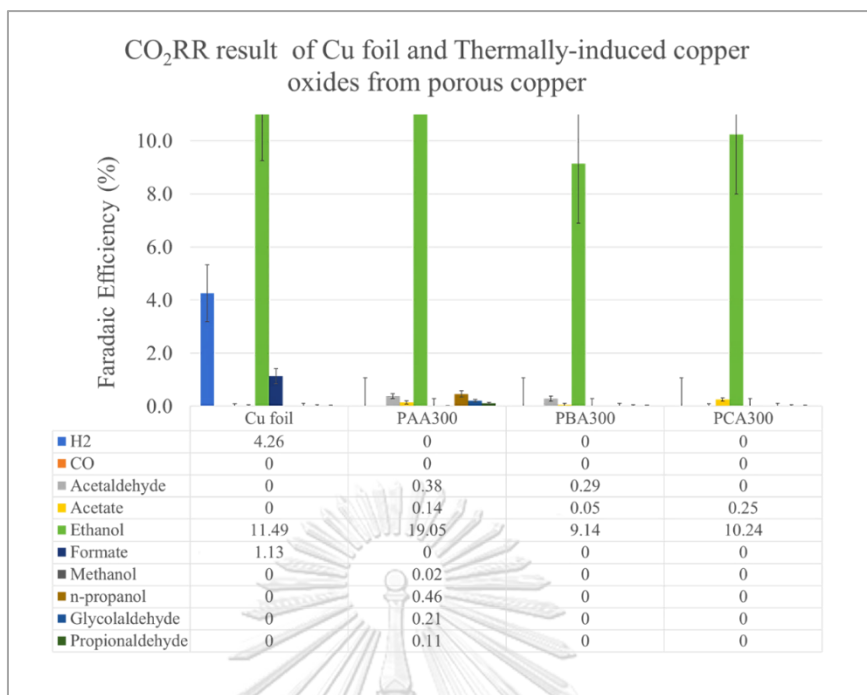


Figure 87 CO<sub>2</sub>RR result of copper foil and of thermally-induced porous copper oxides at -1.3V (Ag/AgCl) in 0.1M KHCO<sub>3</sub>.

### 3.4 Analysis

Thermally-induced porous copper oxides (PXA300) was fabricated to study the correlation between the physical and chemical properties and the CO<sub>2</sub>RR performance. The current density of CO<sub>2</sub>RR process of PXA300 was higher than of PX approximately 2 times. The product distribution of PXA300 were higher than of PX. Small amount of methanol was detected by PAA300, it was not detected by porous copper due to the synergistic between physical and chemical properties. Although, increase in surface area can enhance the active site causing increase in rate of reaction, it is not the only factor which affect to the CO<sub>2</sub>RR product distribution. Porosity and chemical composition also affect to the product distribution. The XPS analysis can be used to confirm the chemical composition for only 10 nm depth from the surface of catalyst. The oxidation state of copper detected by XPS is the hypothetical charge of an atom bonding to a different atom fully ionic. It represents the degree of oxidation or loss of electrons (Cu<sup>0</sup>, Cu<sup>+</sup>, and Cu<sup>2+</sup>) of an atom in a chemical compound. The most product distribution are detected by the porous copper A which passing through the oxidation process (PAA300). On the other hand, compared in porous copper, porous B provide the highest rate of reaction and product distribution. For the effect of particle shape and size, the result shows that the cubic particle and larger particle size provide lower product distribution than of the round particle and small particles, respectively. In case of the performance of electrode, it is generally considered from high selectivity of the desirable products or increase in rate of reaction. According to this work, the fabricated oxidized porous copper A

(PAA300) is the best candidate of all samples because it can enhance rate of reaction as high as 16 times and 7 times compared to copper foil, and porous copper, respectively. Moreover, it also provides the highest product distribution compared to other fabricated catalysts. Some detected products are formed by requiring much more electron transfer than of CO and formate.

The correlation of the pore characteristic and porous morphology can be summarized as following. Increase in concentration of  $\text{CuSO}_4$  in porous copper fabrication solution enlarge the thickness of porous copper measured from the substrate. Increase in porosity enhance the surface area causing increase in the active site on the catalyst surface. Particle shape and size also affect to the surface area. Dendritic-like structure with round-shaped copper particle provide higher surface area than of cubic-shaped copper particle. The surface roughness has the similar trend as the porosity. Porosity has more significantly effect to product distribution than of pore size. Moreover, pore distribution of pulse electrodeposited porous copper is more uniform than of constant current porous copper. The variety of pore size of constant current porous copper may the main cause to provide the diversified product distribution. Therefore, pulse electrodeposited porous copper probably provide the higher selectivity of the desirable product due to the uniform pore structure.

## 7. Conclusion

Since, the electrocatalyst is the important parts of  $\text{CO}_2\text{RR}$  to enhance the performance, acquiring the desirable product or improving the rate of reaction. This work manifests the insight correlation between parameter of sample fabrication and the  $\text{CO}_2\text{RR}$  performance. The characterization of physical and chemical property was used as a bridge to clarify them. Key of this study were summarized as follow.

- 1) Increasing deposition time and decreasing applied current density causing enlargement of apparent pore size due to slow rate of hydrogen evolution but the effects of deposition time and current density on apparent porosity is however inconclusive, and the values of apparent porosity vary less significantly as compared to pore size.
- 2) Bath solution strongly affect to the obtained porous structure. Higher concentration of  $\text{CuSO}_4$  enhance the copper deposit on the substrate due to higher copper ion in the bath solution. Porous copper with HCl in bath solution have the shorter branch of porous structure because the deposition reaction was accelerated by HCl.
- 3) The constant-current porous structure augments the true surface area as confirmed by BET as high as  $19.56 \text{ A/cm}^2$  and probably unique structure with  $58 \text{ }\mu\text{m}$  apparent pore size and 31.11% of apparent porosity. BJH result also confirm that all constant-current porous coppers were mesoporous with 2-50 nm pore diameter.



- 4) Ra value of constant-current porous coppers was in the range of 25-50  $\mu\text{m}$  whereas Ra value of pulse electrodeposited porous copper was in the range of 1.8-4.4  $\mu\text{m}$ . These values were different in one order of magnitude. Pulsed electrodeposition contributes more condensed porous copper with lower surface roughness because there was more time when pulse off time to replenish the copper ion. Pulse electrodeposition can be a promising catalyst to develop as CO<sub>2</sub>RR or other applications.
- 5) Porous copper enhances 4 times higher of rate of reaction with more variable valuable chemicals formation in CO<sub>2</sub>RR performance compared to copper foil due to the development of structure.
- 6) Excessive applied voltage causes redundant hydrogen formation and reducing in other valuable chemicals formation as confirmed by the result of CO<sub>2</sub>RR tested at Nanotec, NSTDA.
- 7) Only Cu<sup>+</sup> and Cu<sup>2+</sup> were detected on the surface of sample oxidized at 300°C and 500°C but all of oxidation states were detected on the surface of sample oxidized at 800°C. The oxidation state of sample oxidized at 1,000°C consisting of Cu<sup>0</sup> and Cu<sup>2+</sup> without Cu<sup>+</sup>. Oxidation temperature of thermally oxidized copper fabrication causing the different surface chemical composition and oxidation state compared to copper foil causing higher rate of reaction and more product distribution in CO<sub>2</sub>RR performance.
- 8) Change in microstructure and change in chemical composition of the thermally-induced porous copper oxides strongly enhance the CO<sub>2</sub>RR performance. This electrocatalyst provide 9 time and 4 times of rate of reaction compared to copper foil, and porous coppers, respectively as well as more product distribution. Some many electrons required products (i.e., glycolaldehyde and propionaldehyde) was also detected as product of this electrocatalyst.

All conclusions provide the direction of copper-based catalyst consisting of 3 main issues; (1) the higher apparent porosity tend to get higher product distribution (PB vs. PA), (2) Improvement of physical and chemical method deliver the better catalyst both in case of rate of reaction and product distribution (PAA300 which fabricated as oxidized porous A), and (3) the oxidation process increase the catalyst stability confirmed by the chemical composition on the surface after running CO<sub>2</sub>RR.

## 8. Reference

1. EPA, U. *CO<sub>2</sub> sources only zero carbon*. 2018; Available from: [http://www.onlyzerocarbon.org/sources\\_co2.html](http://www.onlyzerocarbon.org/sources_co2.html).
2. Quaschnig, V. *Development of Global Carbon Dioxide Emissions and Concentration in Atmosphere*. 2018 Available from: [https://www.volker-quaschnig.de/datserv/CO2/index\\_e.php](https://www.volker-quaschnig.de/datserv/CO2/index_e.php).
3. Prapunpoj, P.C.a.C., *Concentrations of Carbon Dioxide within Land Transportation System in Bangkok*. Thai Journal of Science and Technology, 2015. **23**(6): p. 898-913.
4. Arnette, A.N., *Renewable energy and carbon capture and sequestration for a reduced carbon energy plan: An optimization model*. Renewable and Sustainable Energy Reviews, 2017. **70**(Supplement C): p. 254-265.
5. Pérez-Fortes, M., et al., *Methanol synthesis using captured CO<sub>2</sub> as raw material: Techno-economic and environmental assessment*. Applied Energy, 2016. **161**(Supplement C): p. 718-732.
6. Graves, C., et al., *Sustainable hydrocarbon fuels by recycling CO<sub>2</sub> and H<sub>2</sub>O with renewable or nuclear energy*. Renewable and Sustainable Energy Reviews, 2011. **15**(1): p. 1-23.
7. Goeppert, A., et al., *Recycling of carbon dioxide to methanol and derived products - closing the loop*. Chemical Society Reviews, 2014. **43**(23): p. 7995-8048.
8. Jhong, H.-R.M., S. Ma, and P. Ja Kenis, *Electrochemical conversion of CO<sub>2</sub> to useful chemicals: Current status, remaining challenges, and future opportunities*. Vol. 2. 2013. 191-199.
9. Alper, E. and O. Yuksel Orhan, *CO<sub>2</sub> utilization: Developments in conversion processes*. Petroleum, 2017. **3**(1): p. 109-126.
10. Ola, O., M. Mercedes Maroto-Valer, and S. Mackintosh, *Turning CO<sub>2</sub> into Valuable Chemicals*. Energy Procedia, 2013. **37**(Supplement C): p. 6704-6709.
11. Gattrell, M., N. Gupta, and A. Co, *A review of the aqueous electrochemical reduction of CO<sub>2</sub> to hydrocarbons at copper*. Journal of Electroanalytical Chemistry, 2006. **594**(1): p. 1-19.
12. Hirunsit, P., W. Soodsawang, and J. Limtrakul, *CO<sub>2</sub> Electrochemical Reduction to Methane and Methanol on Copper-Based Alloys: Theoretical Insight*. The Journal of Physical Chemistry C, 2015. **119**(15): p. 8238-8249.
13. Arakawa, H., et al., *Catalysis Research of Relevance to Carbon Management: Progress, Challenges, and Opportunities*. Chemical Reviews, 2001. **101**(4): p. 953-996.
14. Kim, J., et al., *Methanol production from CO<sub>2</sub> using solar-thermal energy: process development and techno-economic analysis*. Energy & Environmental Science, 2011. **4**(9): p. 3122-3132.
15. Wang, Y., et al., *Tuning of CO<sub>2</sub> Reduction Selectivity on Metal Electrocatalysts*. Small, 2017. **13**(43): p. 1701809-n/a.
16. Kuhl, K.P., et al., *New insights into the electrochemical reduction of carbon dioxide on metallic copper surfaces*. Energy & Environmental Science, 2012. **5**(5): p. 7050-7059.

17. Xie, J.F., Y.X. Huang, and H.Q. Yu, *Tuning the catalytic selectivity in electrochemical CO<sub>2</sub> reduction on copper oxide-derived nanomaterials*. *Frontiers of Environmental Science & Engineering*, 2015. **9**(5): p. 861-866.
18. Chladek, P., et al., *Characterization of Copper Foam as Catalytic Material in Ethanol Dehydrogenation*. Vol. 85. 2008. 917.
19. Zhang, W., et al., *Progress and Perspective of Electrocatalytic CO<sub>2</sub> Reduction for Renewable Carbonaceous Fuels and Chemicals*. *Advanced Science*, 2018. **5**(1): p. 1700275.
20. Hori, Y., *Electrochemical CO<sub>2</sub> Reduction on Metal Electrodes*, in *Modern Aspects of Electrochemistry*, C.G. Vayenas, R.E. White, and M.E. Gamboa-Aldeco, Editors. 2008, Springer New York: New York, NY. p. 89-189.
21. Hatsukade, T., et al., *Insights into the electrocatalytic reduction of CO<sub>2</sub> on metallic silver surfaces*. *Physical Chemistry Chemical Physics*, 2014. **16**(27): p. 13814-13819.
22. Peterson, A.A., et al., *How copper catalyzes the electroreduction of carbon dioxide into hydrocarbon fuels*. *Energy & Environmental Science*, 2010. **3**(9): p. 1311-1315.
23. Wang, Y., C. Niu, and D. Wang, *Metallic Nanocatalysts for Electrochemical CO<sub>2</sub> Reduction in Aqueous Solutions*. Vol. 527. 2018.
24. Huang, Y., et al., *Electrochemical Reduction of CO<sub>2</sub> Using Copper Single-Crystal Surfaces: Effects of CO\* Coverage on the Selective Formation of Ethylene*. *ACS Catalysis*, 2017. **7**(3): p. 1749-1756.
25. Azuma, M., et al., *Electrochemical Reduction of Carbon Dioxide on Various Metal Electrodes in Low-Temperature Aqueous KHCO<sub>3</sub> Media*. *Journal of The Electrochemical Society*, 1990. **137**(6): p. 1772-1778.
26. Zhu, W., et al., *Active and Selective Conversion of CO<sub>2</sub> to CO on Ultrathin Au Nanowires*. *Journal of the American Chemical Society*, 2014. **136**(46): p. 16132-16135.
27. Chen, Y. and M.W. Kanan, *Tin Oxide Dependence of the CO<sub>2</sub> Reduction Efficiency on Tin Electrodes and Enhanced Activity for Tin/Tin Oxide Thin-Film Catalysts*. *Journal of the American Chemical Society*, 2012. **134**(4): p. 1986-1989.
28. Zhang, S., P. Kang, and T.J. Meyer, *Nanostructured Tin Catalysts for Selective Electrochemical Reduction of Carbon Dioxide to Formate*. *Journal of the American Chemical Society*, 2014. **136**(5): p. 1734-1737.
29. Bagger, A., et al., *Electrochemical CO<sub>2</sub> Reduction: A Classification Problem*. *ChemPhysChem*, 2017. **18**(22): p. 3266-3273.
30. Cave, E.R., et al., *Electrochemical CO<sub>2</sub> reduction on Au surfaces: mechanistic aspects regarding the formation of major and minor products*. *Physical Chemistry Chemical Physics*, 2017. **19**(24): p. 15856-15863.
31. Dong Yang, K., et al., *Morphology-Directed Selective Production of Ethylene or Ethane from CO<sub>2</sub> on a Cu Mesopore Electrode*. 2016.
32. Sen, S., D. Liu, and G.T.R. Palmore, *Electrochemical Reduction of CO<sub>2</sub> at Copper Nanofoams*. *ACS Catalysis*, 2014. **4**(9): p. 3091-3095.
33. Chen, Y., C.W. Li, and M.W. Kanan, *Aqueous CO<sub>2</sub> Reduction at Very Low Overpotential on Oxide-Derived Au Nanoparticles*. *Journal of the American Chemical Society*, 2012. **134**(49): p. 19969-19972.

34. Hori, Y., et al., *Electrochemical Reduction of CO at a Copper Electrode*. The Journal of Physical Chemistry B, 1997. **101**(36): p. 7075-7081.
35. Sarfraz, S., et al., *Cu–Sn Bimetallic Catalyst for Selective Aqueous Electroreduction of CO<sub>2</sub> to CO*. ACS Catalysis, 2016. **6**(5): p. 2842-2851.
36. Ma, S. and P. Ja Kenis, *Electrochemical conversion of CO<sub>2</sub> to useful chemicals: Current status, remaining challenges, and future opportunities*. Current Opinion in Chemical Engineering, 2013. **2**: p. 191–199.
37. Goeppert, A., et al., *Recycling of carbon dioxide to methanol and derived products – closing the loop*. Chemical Society Reviews, 2014. **43**(23): p. 7995-8048.
38. Frese, K.W., *ELECTROCHEMICAL REDUCTION OF CO<sub>2</sub> AT INTENTIONALLY OXIDIZED COPPER ELECTRODES*. 1991. **138**(11): p. 3338-3344.
39. Alinajafi, H.A., A.A. Ensafi, and B. Rezaei, *Reduction of carbon dioxide to methanol on the surface of adenine functionalized reduced graphene oxide at a low potential*. International Journal of Hydrogen Energy, 2018. **43**(52): p. 23262-23274.
40. Hang Low, Q., et al., *Enhanced Electroreduction of Carbon Dioxide to Methanol Using Zinc Dendrites Pulse-Deposited on Silver Foam*. Angewandte Chemie, 2018. **131**.
41. Safdar Hossain, S., S. Ur Rahman, and S. Ahmed, *Electrochemical Reduction of Carbon Dioxide over CNT-Supported Nanoscale Copper Electrocatalysts*. Journal of Nanomaterials, 2014. **2014**.
42. Zhang, W., et al., *Electrochemical Reduction of Carbon Dioxide to Methanol on Hierarchical Pd/SnO<sub>2</sub> Nanosheets with Abundant Pd–O–Sn Interfaces*. Angewandte Chemie International Edition, 2018. **57**(30): p. 9475-9479.
43. Jiwanti, P.K., et al., *Selective production of methanol by the electrochemical reduction of CO<sub>2</sub> on boron-doped diamond electrodes in aqueous ammonia solution*. RSC Advances, 2016. **6**(104): p. 102214-102217.
44. Le, M., et al., *Electrochemical Reduction of CO<sub>2</sub> to CH<sub>3</sub>OH at Copper Oxide Surfaces*. Journal of the Electrochemical Society, 2011. **158**.
45. Li, P., et al., *New insights into the photo-enhanced electrocatalytic reduction of carbon dioxide on MoS<sub>2</sub>-rods/TiO<sub>2</sub> NTs with unmatched energy band*. Applied Catalysis B: Environmental, 2014. **147**: p. 912-919.
46. Shironita, S., et al., *Methanol generation by CO<sub>2</sub> reduction at a Pt–Ru/C electrocatalyst using a membrane electrode assembly*. Journal of Power Sources, 2013. **240**: p. 404–410.
47. Yang, D., et al., *Selective electroreduction of carbon dioxide to methanol on copper selenide nanocatalysts*. Nature Communications, 2019. **10**(1): p. 677.
48. Albo, J., et al., *Production of methanol from CO<sub>2</sub> electroreduction at Cu<sub>2</sub>O and Cu<sub>2</sub>O/ZnO-based electrodes in aqueous solution*. Applied Catalysis B Environmental, 2015. **176-177**: p. 709-717.
49. Albo, J. and A. Irabien, *Cu<sub>2</sub>O-loaded gas diffusion electrodes for the continuous electrochemical reduction of CO<sub>2</sub> to methanol*. Journal of Catalysis, 2016.

50. Li, C.W. and M.W. Kanan, *CO<sub>2</sub> Reduction at Low Overpotential on Cu Electrodes Resulting from the Reduction of Thick Cu<sub>2</sub>O Films*. Journal of the American Chemical Society, 2012. **134**(17): p. 7231-7234.
51. Bandi, A., *Electrochemical Reduction of Carbon Dioxide on Conductive Metallic Oxides*. J. Electrochem. Soc., 1990. **137**(7): p. 2157-2160.
52. Summers, D.P., S. Leach, and K.W. Frese, *The electrochemical reduction of aqueous carbon dioxide to methanol at molybdenum electrodes with low overpotentials*. Journal of Electroanalytical Chemistry and Interfacial Electrochemistry, 1986. **205**(1): p. 219-232.
53. Hirunsit, P., *Electroreduction of Carbon Dioxide to Methane on Copper, Copper–Silver, and Copper–Gold Catalysts: A DFT Study*. The Journal of Physical Chemistry C, 2013. **117**(16): p. 8262-8268.
54. Jedidi, A., et al., *Generation of Cu–In alloy surfaces from CuInO<sub>2</sub> as selective catalytic sites for CO<sub>2</sub> electroreduction* N3 - 10.1039/C5TA05669A. 2015.
55. Rasul, S., et al., *A Highly Selective Copper–Indium Bimetallic Electrocatalyst for the Electrochemical Reduction of Aqueous CO<sub>2</sub> to CO*. Angewandte Chemie International Edition, 2015. **54**(7): p. 2146-2150.
56. Li, M., et al., *Mesoporous palladium–copper bimetallic electrodes for selective electrocatalytic reduction of aqueous CO<sub>2</sub> to CO*. Journal of Materials Chemistry A, 2016. **4**(13): p. 4776-4782.
57. Kortlever, R., et al., *Electrochemical CO<sub>2</sub> Reduction to Formic Acid at Low Overpotential and with High Faradaic Efficiency on Carbon-Supported Bimetallic Pd–Pt Nanoparticles*. ACS Catalysis, 2015. **5**: p. 3916-3923.
58. Le, M.T.H., *Electrochemical reduction of CO<sub>2</sub> to methanol*, in *LSU Master's Teses*. 2011, Louisiana State University.
59. M, M., *Study the Influence of the Anodizing Process Parameters on the anodized copper hardness*. 2017.
60. Stepniowski, W.J. and W.Z. Misiolek, *Review of Fabrication Methods, Physical Properties, and Applications of Nanostructured Copper Oxides Formed via Electrochemical Oxidation*. Nanomaterials (Basel, Switzerland), 2018. **8**(6): p. 379.
61. Castrejón-Sánchez, V.-H., et al., *Thermal oxidation of copper over a broad temperature range: towards the formation of cupric oxide (CuO)*. Materials Research Express, 2019. **6**(7): p. 075909.
62. Cocke, D.L., et al., *The low-temperature thermal oxidation of copper, Cu<sub>3</sub>O<sub>2</sub>, and its influence on past and future studies*. Vacuum, 2005. **79**(1): p. 71-83.
63. Jiang, X., T. Herricks, and Y. Xia, *CuO Nanowires Can Be Synthesized by Heating Copper Substrates in Air*. Nano Letters, 2002. **2**(12): p. 1333-1338.
64. Lee, S.-K., H.-C. Hsu, and W.-H. Tuan, *Oxidation Behavior of Copper at a Temperature below 300 °C and the Methodology for Passivation*. Materials Research, 2016. **19**.
65. Liu, S., et al., *Ultrathin 5-fold twinned sub-25nm silver nanowires enable highly selective electroreduction of CO<sub>2</sub> to CO*. Nano Energy, 2018. **45**: p. 456-462.
66. Reske, R., et al., *Particle Size Effects in the Catalytic Electroreduction of CO<sub>2</sub> on Cu Nanoparticles*. Journal of the American Chemical Society, 2014. **136**(19): p. 6978-6986.

67. Rosen, J., et al., *Mechanistic Insights into the Electrochemical Reduction of CO<sub>2</sub> to CO on Nanostructured Ag Surfaces*. ACS Catalysis, 2015. **5**(7): p. 4293-4299.
68. Hahn, C., et al., *Engineering Cu surfaces for the electrocatalytic conversion of CO<sub>2</sub>: Controlling selectivity toward oxygenates and hydrocarbons*. Proceedings of the National Academy of Sciences, 2017. **114**(23): p. 5918.
69. Hori, Y., et al., *Adsorption of CO accompanied with simultaneous charge transfer on copper single crystal electrodes related with electrochemical reduction of CO<sub>2</sub> to hydrocarbons*. Surface Science, 1995. **335**: p. 258-263.
70. Takahashi, I., et al., *Electrochemical reduction of CO<sub>2</sub> at copper single crystal Cu(S)-[n(111)×(111)] and Cu(S)-[n(110)×(100)] electrodes*. Journal of Electroanalytical Chemistry, 2002. **533**(1): p. 135-143.
71. Dutta, A., et al., *Morphology Matters: Tuning the Product Distribution of CO<sub>2</sub> Electroreduction on Oxide-Derived Cu Foam Catalysts*. ACS Catalysis, 2016. **6**(6): p. 3804-3814.
72. Min, S., et al., *Low overpotential and high current CO<sub>2</sub> reduction with surface reconstructed Cu foam electrodes*. Nano Energy, 2016. **27**(Supplement C): p. 121-129.
73. Mariano, R.G., et al., *Selective increase in CO<sub>2</sub> electroreduction activity at grain-boundary surface terminations*. Science, 2017. **358**(6367): p. 1187.
74. Tang, W., et al., *The importance of surface morphology in controlling the selectivity of polycrystalline copper for CO<sub>2</sub> electroreduction*. Physical Chemistry Chemical Physics, 2012. **14**(1): p. 76-81.
75. Lu, Q., et al., *A selective and efficient electrocatalyst for carbon dioxide reduction*. Nature Communications, 2014. **5**(1): p. 3242.
76. Ma, M., K. Djanashvili, and W.A. Smith, *Controllable Hydrocarbon Formation from the Electrochemical Reduction of CO<sub>2</sub> over Cu Nanowire Arrays*. Angewandte Chemie International Edition, 2016. **55**(23): p. 6680-6684.
77. Salehi-Khojin, A., et al., *Nanoparticle Silver Catalysts That Show Enhanced Activity for Carbon Dioxide Electrolysis*. The Journal of Physical Chemistry C, 2013. **117**(4): p. 1627-1632.
78. Steven Michael Brown , Y.W.H., Chaerin Kim and Fikile R. Brushet. *Bimetallic Gold-Copper Nanotube Catalyst for Cost Efficient and Selective Electrochemical Reduction of Carbon Dioxide to Carbon Monoxide*. in ECS - The Electrochemical Society. 2016.
79. Kim, D., et al., *Electrochemical Activation of CO<sub>2</sub> through Atomic Ordering Transformations of AuCu Nanoparticles*. Journal of the American Chemical Society, 2017. **139**(24): p. 8329-8336.
80. Brown, S., et al., *Impact of Catalyst Support on Activity and Selectivity of Gold Nanoparticles for the Carbon Dioxide Reduction Reaction*. 2016.
81. Niu, J., et al., *Effect of electrodeposition parameters on the morphology of three-dimensional porous copper foams*. 2015. **10**: p. 7331-7340.
82. Pestryakov, A.N., et al., *Supported foam-copper catalysts for methanol selective oxidation*. Catalysis Communications, 2004. **5**(12): p. 777-781.

83. Shin, H.-C. and M. Liu, *Copper Foam Structures with Highly Porous Nanostructured Walls*. Chemistry of Materials, 2004. **16**(25): p. 5460-5464.
84. Daiyan, R., et al., *Highly Selective Conversion of CO<sub>2</sub> to CO Achieved by a Three-Dimensional Porous Silver Electrocatalyst*. Chemistryselect, 2017. **2**(3): p. 879-884.
85. Zhu, P., Z. Wu, and Y. Zhao, *Hierarchical porous Cu with high surface area and fluid permeability*. Scripta Materialia, 2019. **172**: p. 119-124.
86. Luo, B., *3D Porous Copper Films with Large Specific Surface Prepared by Hydrogen Bubble Template*. Asian Journal of Chemistry, 2013. **25**: p. 9927-9930.
87. Nikolić, N.D., G. Branković, and K.I. Popov, *Optimization of electrolytic process of formation of open and porous copper electrodes by the pulsating current (PC) regime*. Materials Chemistry and Physics, 2011. **125**(3): p. 587-594.
88. Najdovski, I., *The electrochemical fabrication of porous bimetallic structures and their applications in catalysis and sensing*. 2013.
89. Lv, J.-J., et al., *A Highly Porous Copper Electrocatalyst for Carbon Dioxide Reduction*. Advanced Materials, 2018. **30**(49): p. 1803111.
90. Nguyen, T., et al., *Hydrogen bubbling-induced micro/nano porous MnO<sub>2</sub> films prepared by electrodeposition for pseudocapacitor electrodes*. Electrochimica Acta, 2016. **202**: p. 166-174.
91. Lee, S.Y., et al., *Mixed Copper States in Anodized Cu Electrocatalyst for Stable and Selective Ethylene Production from CO<sub>2</sub> Reduction*. Journal of the American Chemical Society, 2018. **140**(28): p. 8681-8689.
92. Xiao, H., et al., *Cu metal embedded in oxidized matrix catalyst to promote CO<sub>2</sub> activation and CO dimerization for electrochemical reduction of CO<sub>2</sub>*. Proceedings of the National Academy of Sciences, 2017. **114**(26): p. 6685-6688.
93. Chou, T.C., et al., *Controlling the Oxidation State of the Cu Electrode and Reaction Intermediates for Electrochemical CO(2) Reduction to Ethylene*. J Am Chem Soc, 2020. **142**(6): p. 2857-2867.



## Appendix: Copper foil

Copper foil was used for being as a reference to compare the physical (structure) and chemical properties with other fabricated electrode (porous copper, thermally oxidized copper, and thermally oxidized porous copper). As-received copper foil has high purity as 99.99997% with 0.1 mm thick. SEM image and the detailed chemical composition of copper foil was shown in Figure . Its bulk composition analyzed by EDX consisting of 87.06%Cu, 2.4%O, and 10.54%C. Preparation of copper foil surface or cleaning process was required because there is high amount of carbon on the copper foil surface where is the place for reacting the CO<sub>2</sub> reduction. It probably causes the block of electron transfer on the catalytic surface.

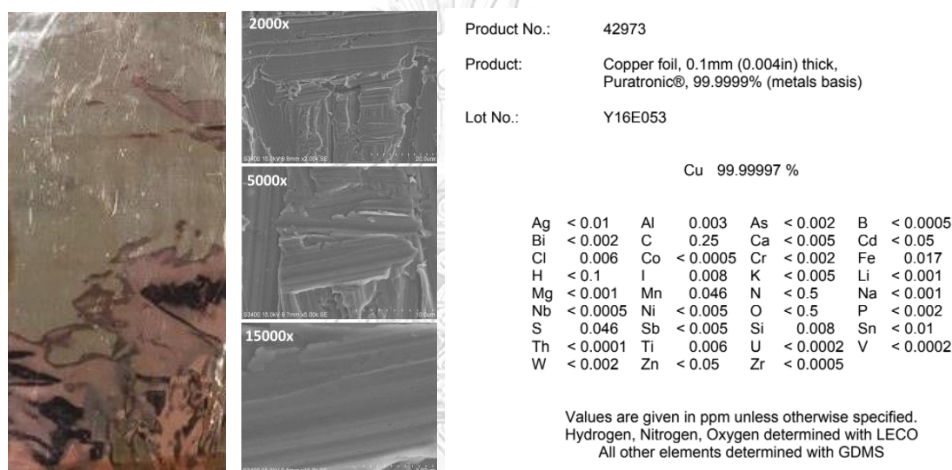


Figure A1 the detailed chemical composition of copper foil.

There are two surface preparation processes, washing and electropolishing (EP), were used to reduce the carbon content of the copper foil surface. For washing method, the copper foil was sonicated in ethanol, isopropanol, and deionized water (DI water), respectively by ultrasonic sonicating for 30 minutes each. The composition of washed copper foil is also similar to the as-received copper foil. After performing EP by applied +1.5V (Ag/AgCl) for 2 minutes in 85% phosphoric acid and rinsed in DI water, the treated surface look shiny because of less amount of carbon proved by EDX results. There is 96.7% Cu, 1.3%O, and 2%C in the bulk. After passing through the CO<sub>2</sub>RR process at -1.3V (Ag/AgCl) in 0.1M KHCO<sub>3</sub>, the composition do not significantly change indicating that copper foil still acts good stability (for 1 test of the reaction) as shown in Figure .

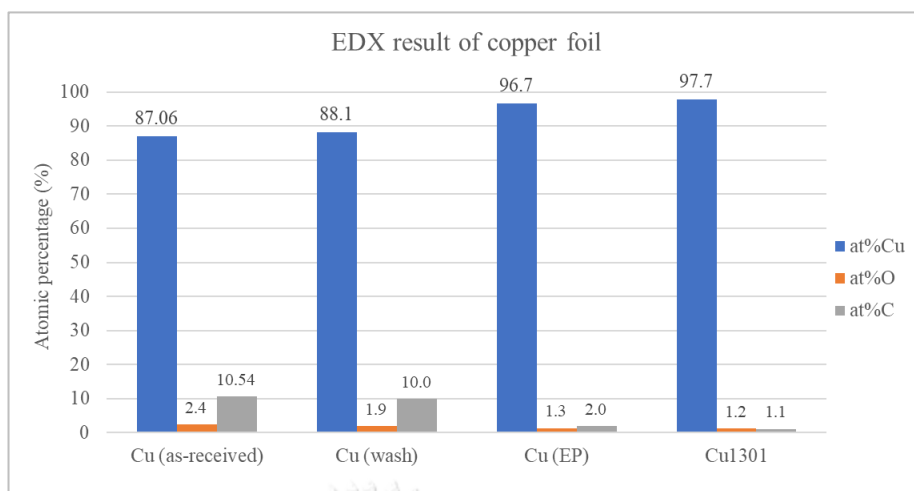


Figure A2 EDX result of copper foil.

Moreover, considering to oxidation state of copper foil, as received and washed copper foil surface consist of all copper ion species ( $\text{Cu}^0$ ,  $\text{Cu}^+$ , and  $\text{Cu}^{2+}$ ) with similar amount with the ratio of approximate 44:44:12. On the other hand, only  $\text{Cu}^0$ , and  $\text{Cu}^{2+}$  with the ratio 1:1 for electropolished copper foil and only  $\text{Cu}^+$ , and  $\text{Cu}^{2+}$  with the ratio 1:1 for copper foil after passing through  $\text{CO}_2\text{RR}$  at  $-1.3\text{V}$  ( $\text{Ag}/\text{AgCl}$ ). The XPS profile of all copper foil samples are shown in Figure .

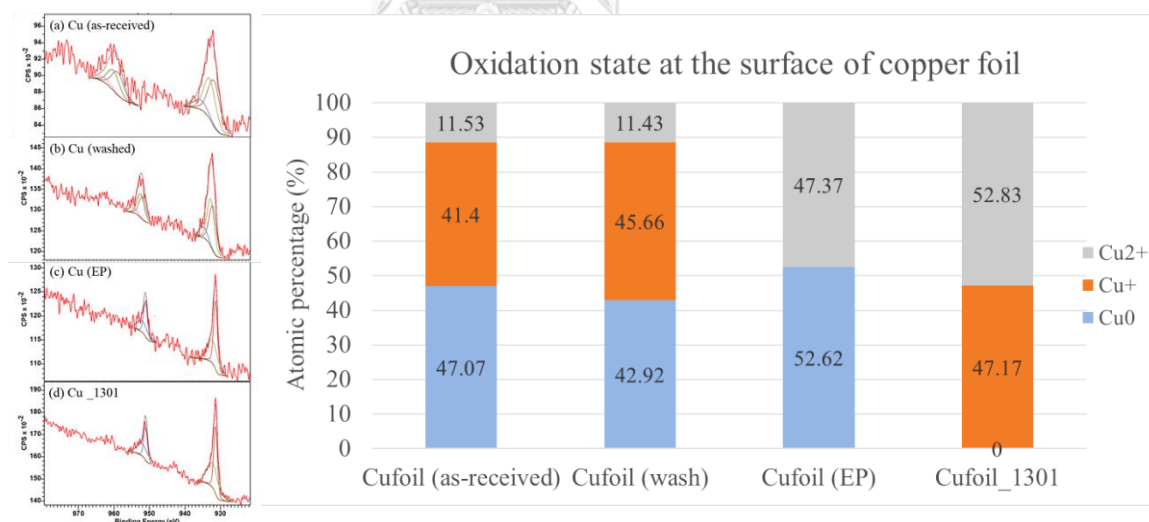


Figure A3 XPS profile and oxidation state of copper foil.

Capacitance of the double electrical layer (DEL) of copper foil usually in the range of  $10\text{--}20\text{ uF}/\text{cm}^2$ . This value was referred from the previous work [1] due to some errors of the experiment of this work. Although, the graph of this experiment was shown in Figure A4 Capacitance experiment of copper foil.

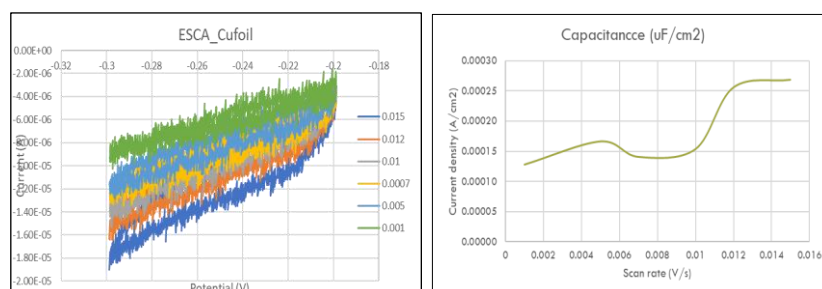


Figure A4 Capacitance experiment of copper foil.

### Comparison of conventional H-Cell and Sandwich (flat) Cell

According to the CO<sub>2</sub>RR experiment, copper foil was tested by two type of reactors (conventional H-cell and Flat cell). Both of reactors were shown in Figure 88 CO<sub>2</sub>RR electrolyzer (1) the conventional H-cell and (b) the flat cell.

. Sandwich (flat) cell is a type of H-cell with shorter distance between working electrode and counter electrode. Both type of reactors are composing of 3 electrodes: working electrode (WE), counter electrode (CE), and reference electrode (RE). The conventional H-cell is made of glass but the flat cell is made of the teflon. The distance between WE and CE of H-cell is approximately 6 cm but for flat cell is approximately 2 cm. For the conventional H-cell, the 6.25 cm<sup>2</sup> (2.5 cm x 2.5 cm) copper foil was used as WE whereas platinum foil was used as CE. Ag/AgCl was used as RE. The nafion 117 membrane was used as anion exchange membrane positioned in the middle of the cell between catholytic and anolytic parts. 0.1M KHCO<sub>3</sub> was used as electrolyte. For flat cell, the 9.24 cm<sup>2</sup> (4.2 cm x 2.2 cm) copper foil was used as WE for the flat cell but the platinum rod was used as CE. Ag/AgCl and nafion 117 membrane were also used as RE and anion exchange membrane, respectively. Injection of CO<sub>2</sub> gas of both system were similar. CO<sub>2</sub> was injected into the solution system by the tube with 30 ml/min rate of purging for 1 hour before testing. CO<sub>2</sub> gas was also injected all time of an experiment with the same rate. Gas products were detected by Gaschromatography (GC) which directly connected with the reactor. Aqueous products were detected by Nuclear magnetic resonance (NMR) technique. Copper foil was tested in both cell at -1.2 V (Ag/AgCl) to compare the CO<sub>2</sub>RR performance.

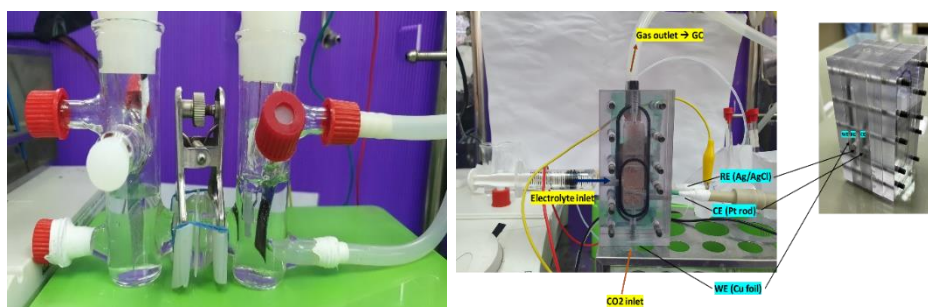


Figure 88 CO<sub>2</sub>RR electrolyzer (1) the conventional H-cell and (b) the flat cell.

For product distribution, after running for 30 minutes, H<sub>2</sub> detected by flat cell was higher than of the conventional H-cell approximately 15 times with a small amount of CO whereas no detection of CO in the conventional H-cell. After running for 70 minutes, it was found that less amount of H<sub>2</sub> was detected by flat cell. However, H<sub>2</sub> detected by flat cell was higher than detected by the conventional H-cell approximately 5 times. Moreover, less amount of CO was also detected. Therefore, the result manifest that flat cell has more efficiency to increase the rate of reaction or rate of product formation than of the conventional H-cell. The detected products from the conventional H-cell, and flat cell were summarized as 78.78% and 30.60%, respectively as shown in . It indicate that many other products were not detected by flat cell as high as 70% because probably no reference list of product (i.e., ethylene and acetaldehyde) as shown in Figure A6.

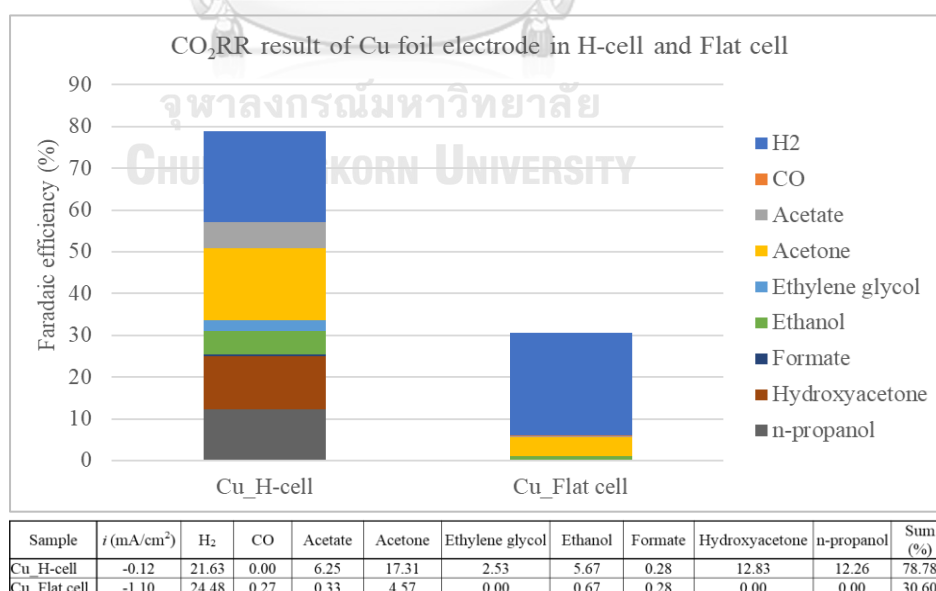


Figure 89 CO<sub>2</sub>RR result of copper foil which tested by H-cell and flat cell electrolyzer.

## REFERENCES



จุฬาลงกรณ์มหาวิทยาลัย  
**CHULALONGKORN UNIVERSITY**



จุฬาลงกรณ์มหาวิทยาลัย  
**CHULALONGKORN UNIVERSITY**

## VITA

<b>NAME</b>	Jidsucha Darayen
<b>DATE OF BIRTH</b>	8 May 1992
<b>PLACE OF BIRTH</b>	Bangkok
<b>INSTITUTIONS ATTENDED</b>	- Metallurgical and chemical engineering - Metal-based catalytic electrodes for carbon dioxide conversion. - Waste recycling and green ecosystem
<b>HOME ADDRESS</b>	84 Baankaewvilla Village, Soi Petchkasem 48 Lane 16, Petchkasem Rd., Bangduan, Pasicharoen, BKK 10160
<b>PUBLICATION</b>	1) Microstructural and Diffusion Analysis of Au-Sn Diffusion Couple Layer Undergoing Heat Treatment at Near Eutectic Temperatures 2) The Thermal-Aging Effect on the Microstructure Evolution and Shear Strength of the Sn-Rich Au-Sn Soldering between Al <sub>2</sub> O <sub>3</sub> and Si Substrate in Microelectronics 3) Porous Electrodeposited Cu as a Potential Electrode for Electrochemical Reduction Reactions of CO <sub>2</sub> 4) Advances in the Key Metal-Based Catalysts for Efficient Electrochemical Conversion of CO <sub>2</sub>